

Millimeter-wave MIMO radars for radio-frequency imaging systems

Citation for published version (APA):

Syeda, R. Z. (2021). *Millimeter-wave MIMO radars for radio-frequency imaging systems: A sparse array topology approach*. [Phd Thesis 1 (Research TU/e / Graduation TU/e), Electrical Engineering]. Eindhoven University of Technology.

Document status and date:

Published: 03/11/2021

Document Version:

Publisher's PDF, also known as Version of Record (includes final page, issue and volume numbers)

Please check the document version of this publication:

- A submitted manuscript is the version of the article upon submission and before peer-review. There can be important differences between the submitted version and the official published version of record. People interested in the research are advised to contact the author for the final version of the publication, or visit the DOI to the publisher's website.
- The final author version and the galley proof are versions of the publication after peer review.
- The final published version features the final layout of the paper including the volume, issue and page numbers.

[Link to publication](#)

General rights

Copyright and moral rights for the publications made accessible in the public portal are retained by the authors and/or other copyright owners and it is a condition of accessing publications that users recognise and abide by the legal requirements associated with these rights.

- Users may download and print one copy of any publication from the public portal for the purpose of private study or research.
- You may not further distribute the material or use it for any profit-making activity or commercial gain
- You may freely distribute the URL identifying the publication in the public portal.

If the publication is distributed under the terms of Article 25fa of the Dutch Copyright Act, indicated by the "Taverne" license above, please follow below link for the End User Agreement:

www.tue.nl/taverne

Take down policy

If you believe that this document breaches copyright please contact us at:

openaccess@tue.nl

providing details and we will investigate your claim.

Millimeter-wave MIMO radars for radio-frequency imaging systems

A sparse array topology approach

This research was financially supported by NWO-TTW through the HTSM research program with project number 13922.



Millimeter-wave MIMO radars for radio-frequency imaging systems: A sparse
array topology approach / by

R. Z. Syeda – Eindhoven : Technische Universiteit Eindhoven, 2021 – Proefschrift

A catalogue record is available from the Eindhoven University of Technology
Library

ISBN: 978-90-386-5391-4

This thesis was prepared with the L^AT_EX 2_ε documentation system

Reproduction: Ipskamp printing, Enschede, The Netherlands

Cover design credits: Syed Ali Abbas Zaidi

Copyright ©2021 by R. Z. Syeda. All rights reserved.

Millimeter-wave MIMO radars for radio-frequency imaging systems

A sparse array topology approach

PROEFSCHRIFT

ter verkrijging van de graad van doctor aan de
Technische Universiteit Eindhoven, op gezag van de
rector magnificus, prof.dr.ir. F.P.T. Baaijens, voor een
commissie aangewezen door het College voor
Promoties in het openbaar te verdedigen
op woensdag 3 november 2021 om 16.00 uur

door

Rabia Zainab Syeda

geboren te Rawalpindi, Pakistan

Dit proefschrift is goedgekeurd door de promotoren en de samenstelling van de promotiecommissie is als volgt:

voorzitter:	prof.dr.ir. M.J. Bentum
1 ^e promotor:	prof.dr.ir. A.B. Smolders
2 ^e promotor:	prof.dr.ir. M.C. van Beurden
leden:	prof.dr.ir. C. Craeye (Université catholique de Louvain)
	prof.dr.ir. P.G.M. Baltus
	prof.dr.ir. M. Mischi
adviseurs:	dr.ir. P.T.M. van Zeijl (Zelectronix B.V.)
	dr.ir. J.G. Bij de Vaate (SRON)

Het Onderzoek of ontwerp dat in dit proefschrift wordt beschreven is uitgevoerd in overeenstemming met de TU/e Gedragscodex Wetenschapsbeoefening.

”Every search begins with beginner’s luck. And every search ends with victor’s being severely tested.”

- *Paulo Coelho*, The Alchemist

Contents

Summary	xiii
List of Abbreviations and Symbols	xv
1 Introduction	1
1.1 Societal relevance of radar imaging systems	1
1.2 mm-Wave radar imaging systems for the automotive industry	3
1.3 Research objectives	5
1.4 Research Activities	6
1.5 Thesis outline	7
1.5.1 Suggested method of reading	7
1.6 Original contributions of this thesis	8
2 En route to MIMO radar	9
2.1 Introduction	9

2.2	Phased-array vs MIMO radar	11
2.2.1	Phased-array radars	11
2.2.2	Limitation of the phased-array	13
2.2.3	MIMO radar	14
2.3	Technical background on MIMO radar	16
2.3.1	Mathematical formulation of MIMO radars	17
2.3.2	Modes of operations for MIMO radars	18
2.3.3	Target detection in MIMO radars	19
2.3.4	Resolution of a radar imaging system	21
2.4	Technical background on antenna array sparsity	22
2.4.1	Antenna array sparsity	23
2.5	State-of-the-art on MIMO radar in radar imaging applications	25
3	A mm-wave MIMO radar demonstrator	29
3.1	Introduction	30
3.2	TDM-MIMO FMCW radar	31
3.3	60-GHz MIMO radar prototype design	31
3.3.1	System architecture functionality	31
3.3.2	Chirp generation section	32
3.3.3	60 GHz RF radar-chip section	33
3.3.4	Data acquisition section	34
3.3.5	MIMO array of radar chips	35
3.4	Comparison of SIMO and MIMO direction of arrival	37
3.5	Performance and evaluation of the prototype	38

3.5.1	Range measurements	38
3.5.2	SNR and target phase error	40
3.5.3	Transmit phase synchronization analysis	41
3.6	Phase-error tolerances for MIMO virtual arrays	42
3.6.1	Transmit, receive and virtual array with errors	43
3.6.2	Uniform and non-uniform array configurations	43
3.6.3	Resulting effects of phase errors	44
3.7	Conclusion	47
4	Regular and irregular sparse array analysis for connected arrays	49
4.1	Introduction	50
4.2	Sparse Configurations	50
4.2.1	Radiation pattern and grating lobes	52
4.2.2	Total effective area	52
4.3	Element terminations for regular-on-grid sparse array	55
4.3.1	Active reflection coefficient	55
4.3.2	Antenna array noise temperature	56
4.4	Conclusion	59
5	Sparse Virtual Array Synthesis for MIMO Radar Imaging Systems	61
5.1	Introduction	62
5.2	Conventional MIMO virtual array concept and its limitations	64
5.2.1	CASE I: Dense virtual array	66
5.2.2	CASE II: Conventional virtual array	66
5.2.3	Comparison between CASE I and CASE II	66

5.3	Optimization techniques for virtual array synthesis	69
5.3.1	Two-step Synthesis Procedure (TSP) formulation	70
5.3.2	Method I: TSP with maximum scanning	71
5.3.3	Method II: Virtual array synthesis using the methods of least squares	72
5.4	Numerical examples	75
5.4.1	Method I: TSP with maximum scanning	76
5.4.2	Method II: Virtual array synthesis using the method of least squares	81
5.5	Validation using full-wave solver	84
5.5.1	Mutual coupling inclusion in optimization	89
5.6	Discussion on strengths and limitations	89
5.7	Conclusion and future work	91
6	Virtual array pattern measurements using a VNA	93
6.1	Introduction	94
6.2	Measurement strategy	95
6.2.1	Emulating TDM MIMO mode using a two-port VNA	95
6.2.2	Measurement and calibration challenges	99
6.3	Design of a test case with 3 transmit and 4 receive physical element arrays	103
6.4	Manufacturing and measurement set-up	106
6.5	Measurement results	110
6.5.1	Scanning	112
6.6	Conclusion	115
7	Improved 3D imaging MIMO radar	117

7.1	Introduction	118
7.2	Planar virtual array configurations for MIMO radars	118
7.2.1	Linear transmit and receive array with orthogonal axis	119
7.2.2	Planar transmit and receive array	119
7.3	Discussion on the pros and cons	123
7.4	Conclusion	124
8	Conclusion and recommendations	125
8.1	Conclusions	125
8.2	Recommendations	127
A	Transmit phase synchronization analysis	129
	Bibliography	146
	List of publications	147
	Acknowledgements	148
	Curriculum Vitae	150

Summary

Millimeter-wave MIMO radars for Radar Imaging systems

A sparse antenna array topology

Radar imaging systems have become increasingly popular to capture a camera-like image. Especially at millimeter-wave frequencies it can be used for a wide range of commercial applications, such as security, health monitoring, and autonomous driving. Radar systems offer the ability to have a better performance under various weather conditions as compared to their alternatives, such as laser and optical systems. In order to replace or complement a camera-based system in these applications, the radar imaging systems have to meet stringent requirements such as a large bandwidth to realize a high range resolution, and a large electrical aperture to obtain a high angular resolution while keeping the size and cost to a minimum. Primarily these radar systems employ phased-array radar technology which results in large, complex, and expensive systems. Recently, the concept of Multiple-Input-Multiple-Output (MIMO) radar technology is being used as an extension of conventional phased array radars. MIMO radar offers several advantages including an increased angular resolution and reduced cost and energy consumption. In this work, the challenges of designing and evaluating MIMO radars for millimeter-wave imaging radar systems are investigated and analyzed.

A high integration level of single-chip radars with on-chip antennas instigate the idea of using an array of these chips to realize a MIMO radar system, each with its own radar front end and on-chip antennas. The design of such a demonstrator presents a set of challenges, such as the optimal configuration of the array and the synchronization between the chips, which should result in the realization of a low-cost and low-

power MIMO radar. The design of a MIMO array of single-chip Frequency-Modulated-Continuous-Wave (FMCW) radars operating in the 57-63 GHz band is presented and the experimental verification of the realized prototype is discussed in detail.

The MIMO radar has an inherent advantage of a higher angular resolution as compared to phased array radars. However, the dependence of the MIMO virtual array on the topology of the applied transmit and receive arrays allows to further increase the angular resolution by using a sparse array topology for both transmit and receive arrays. For this purpose, two methods using convex optimization are proposed for the synthesis of sparse virtual MIMO-radar arrays with a high performance in terms of narrow beamwidth and low side lobe levels, even while scanning. It is shown that the achieved performance in terms of narrow beamwidth and low side lobe levels is better as compared to conventional dense virtual arrays.

Finally, the challenge of measuring and characterizing virtual arrays in MIMO radars is addressed in this work. Although the characterization of virtual arrays is commonly done with a complete radar-system setup, an alternative approach using a two-port Vector Network Analyzer (VNA) is presented. The measurement strategy for such a characterization of MIMO virtual arrays is presented, evaluated, and verified experimentally.

List of Abbreviations and Symbols

Abbreviations and acronyms

ADC	analog to digital converter
AESA	active electronically steered array
AF	array factor
AoC	antenna-on-chip
ARC	active reflection coefficient
DDS	direct digital synthesizer
DOA	direction-of-arrival
EEP	embedded element pattern
FDM	frequency division multiplexing
FFT	fast Fourier transform
FMCW	frequency modulated continuous wave
FOV	field of view
FPGA	field programmable gate array
IC	integrated circuit
IF	intermediate frequency
LIDAR	light detection and ranging
LNA	low noise amplifier
LO	local oscillator
LNA	low noise amplifier
LRR	long-range radar

MIMO	multiple input multiple output
mm-wave	millimeter-wave
MRR	medium-range radar
OWA	open-ended waveguide antennas
PA	power amplifier
PCB	printed circuit board
PDM	phase division multiplexing
PESA	passive electronically steered array
PLL	phased-locked loop
PMCW	phase modulated continuous wave
RCS	radar cross section
RF	radio frequency
RX	receiver
SIMO	single input multiple output
SLL	side lobe level
SNR	signal-to-noise ratio
SRR	short-range radar
TDM	time division multiplexing
TX	transmitter
UWB	ultra wide band
VCO	voltage controlled oscillator
VNA	vector network analyzer

List of symbols

Symbol	Description
λ_0	free-space wavelength of center frequency
f_0	center frequency
P_t	transmit power
G_t	gain of transmit antenna
G_r	gain of receive antenna
σ_{tgt}	RCS of the target
k	Boltzmann constant
T_0	system temperature
B	bandwidth
S/N	signal to noise ratio
F	noise figure
k_0	free-space wave number
a_n	amplitude of the n -th element transmit signal
Φ_n	phase weight of the n -th element transmit signal
k_0	free-space wave number
θ_0	steering angle
D	maximum diameter of the aperture of the array
$x_m[n]$	discrete-time base-band signal of the m -th transmitter
$s[n]$	discrete-time base-band transmit signal
τ_{mt}	time-delay from the m -th transmitter to the target
τ_{mr}	time-delay from the target to the m -th receiver
\mathbf{a}_t	transmit array steering vector
\mathbf{a}_r	receive array steering vector
\mathbf{a}_v	virtual array steering vector
\mathbf{d}_t	inter-element distance vector of the transmit array
\mathbf{d}_r	inter-element distance vector of the receive array
\mathbf{d}_v	inter-element distance vector of the virtual array
N_t	number of transmit array elements

N_r	number of receive array elements
N_v	number of virtual array elements
$y[n]$	discrete-time base-band receive signal
K	number of targets
θ_k	angle of the k -th target
w_n	complex-valued weight coefficient of the n -th antenna element
δ_{at}	amplitude errors of the transmit array element
δ_{ar}	amplitude errors of the receive array element
ϕ_{pt}	phase errors of the transmit array element
ϕ_{pr}	phase errors of the receive array element
A_{eff}	total effective area
T_{sky}	sky noise temperature
L_t	length of transmit array elements
L_r	length of receive array elements
L_v	length of virtual array elements
\mathbf{S}_{total}	total S-parameter matrix
\mathbf{S}_A	S-parameter matrix A
\mathbf{S}_B	S-parameter matrix B
B_n	amplitude of the noise component
ω_n	frequency of the noise components
ϕ_n	phase of the noise component

CHAPTER ONE

Introduction

1.1 Societal relevance of radar imaging systems

In today's demand-driven era, technology primarily thrives based on the desires and requirements of consumers and so is the case with the automotive industry. The demand for safety, comfort and sustainability is rapidly growing for the car industry and hence the need for autonomous driving is thriving. Although in the past year, the corona pandemic has stalled the driver-less cars vision [1], but as the world is now slowly coming out of the corona pandemic and society goes back to the 'so-called' normal, the travel and commute to-and-from work will also resume en masse [2]. Moreover, the demand for autonomous delivery vans and taxi robots has also been made obvious and essential during stay-at-home times [3]. Therefore, the demand for automobiles that go beyond their current potential, provide a mobile living space while commuting to-and-from work or travel to-and-from a holiday destination and become more safe is going to sky rocket in the near future. Also, traffic density reduction and efficient fuel consumption are among the challenges of today's ever-growing mobile world. Autonomous driving has a potential to contribute to resolving these challenges [4].

The idea of a car that drives itself was instituted as early as the 1950s, but at that time its realization felt far-fetched [5]. However, with the rapid breakthroughs in technology and fast urbanization of mega cities, the vision of autonomous driving has come a long way. Over the past two decades, the road towards self-driving cars has evolved significantly and the path has been segregated into five levels of automation, as shown in Fig. 1.1. In the early 2000s, the adaptation of safety features in high-end

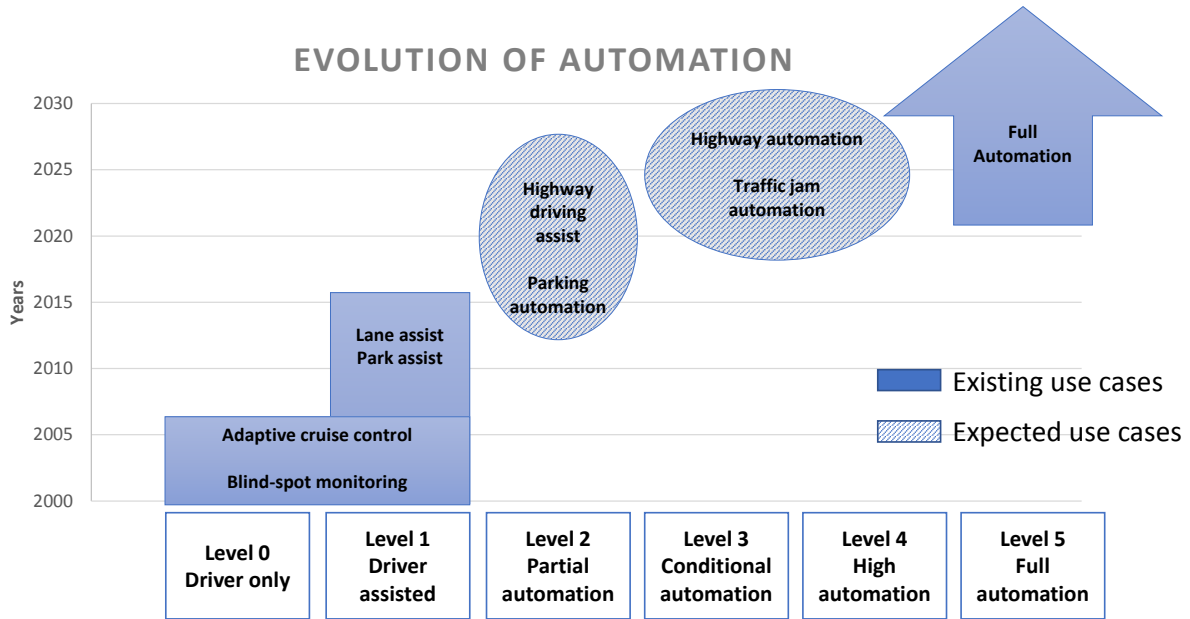


Figure 1.1: The evolution of five levels of automation versus the years with the use cases that already exist in the market (blue shade) and use cases that are expected (pattern shade) [5].

cars became mainstream with the introduction of adaptive cruise control and blind-spot detection where the driver is mainly in control of the vehicle (level 0 and 1). Only recently, car manufacturers, like Audi and BMW [6], have been offering a partial automation (level 2) that mainly involves remote parking and highway auto pilot mode. However, these use cases are still not very mature and mainstream. The automotive industry is now in the process of promising the availability of full highway automation and automation during traffic-jams (level 3 and 4), while some manufacturers, like Tesla, have announced to offer a fully autonomous vehicle (level 5) by the end of the year 2021 [6]. However, whether the engineering capabilities and legal framework will allow this is still questionable. Needless to say is that our future nevertheless holds self-driving cars that will make commuting safe, comfortable and sustainable.

In order for a vehicle to be fully automated, it needs to monitor its surrounding, for which there are a number of sensors placed in the cocoon of the car. The traditional sensors include LIDAR, stereo cameras, infrared cameras, ultrasound sensors and radar sensors. All these sensors have particular capabilities and functions that allow 360° coverage around the car [7]. These sensors are technologically advanced but radar in particular has been gaining a lot of attention by car manufacturers, ever since the technological breakthroughs in semiconductor (silicon-based) Radio Frequency (RF) circuits in the mm-wave frequency band are providing low-cost, low-power, and small-size solutions. Some functionalities of radar are unique to it and give it precedence

over other sensors, such as its ability to create a complete 4D image (range, azimuth, elevation and velocity) and its operation under all weather conditions [8]. Thus, the next step in automotive sensing is a radar imaging system in the mm-wave range.

1.2 mm-Wave radar imaging systems for the automotive industry

Radar imaging systems are a strong candidate when it comes to many 3D environment scanning applications, such as automotive, security and medicine. In the automotive industry, they are used in short-range radar (SRR), medium-range radar (MRR) and long-range radar (LRR). The two categories of radar imaging systems are: microwave imaging and mm-wave imaging. Microwave radar imaging systems operate in the range from 300 MHz to 30 GHz (1 meter to 1 centimeter wavelength) e.g. ultra-wide band (UWB) near-field imaging radars [9] and 24 GHz radars [10]. On the other hand, mm-wave imaging systems operate in the frequency range from 30 GHz to 300 GHz (10 millimeter to 1 millimeter wavelength). The most popular among these systems are the 60 GHz and 77 GHz radar systems [11, 12].

For SRR and MRR, the 24 GHz radar had been used predominantly but due to the introduction of this band in 5G-NR [13], this frequency is expected to become obsolete for automotive applications. The 60 GHz and 77 GHz bands are therefore becoming more suitable for SRR and MRR, in addition to LRR. The mm-wave range is most suitable for radar imaging applications because of its potential for high resolution, which is desirable for target recognition and separation. Therefore, a great deal of focus in the radar community is being put forward to address the challenges that arise when improving the resolution of an imaging system. Radar modules are aimed to have an improved performance through a large bandwidth in order to provide a high range and velocity resolution. The relation of the range and velocity resolution between the microwave and mm-wave frequency ranges is shown in Fig. 1.2. The mm-wave band has a great potential to have higher range and velocity resolution as compared to the microwave band. Next, radar modules are largely employing the concepts of phased-arrays and Multiple-Input Multiple-Output (MIMO) radars to improve the angular resolution, which also depends on the frequency as shown in Fig. 1.3.

From Fig. 1.2 and Fig. 1.3, it is clear that the mm-wave band is the best choice for a high-resolution radar system. However, the mm-wave frequencies bring in challenges and obstacles that need great attention while realizing a radar imaging system at these frequencies. For higher angular resolution a large aperture is required but at mm-wave frequencies, as the wavelength is small, the dense configuration of a typical phased-array

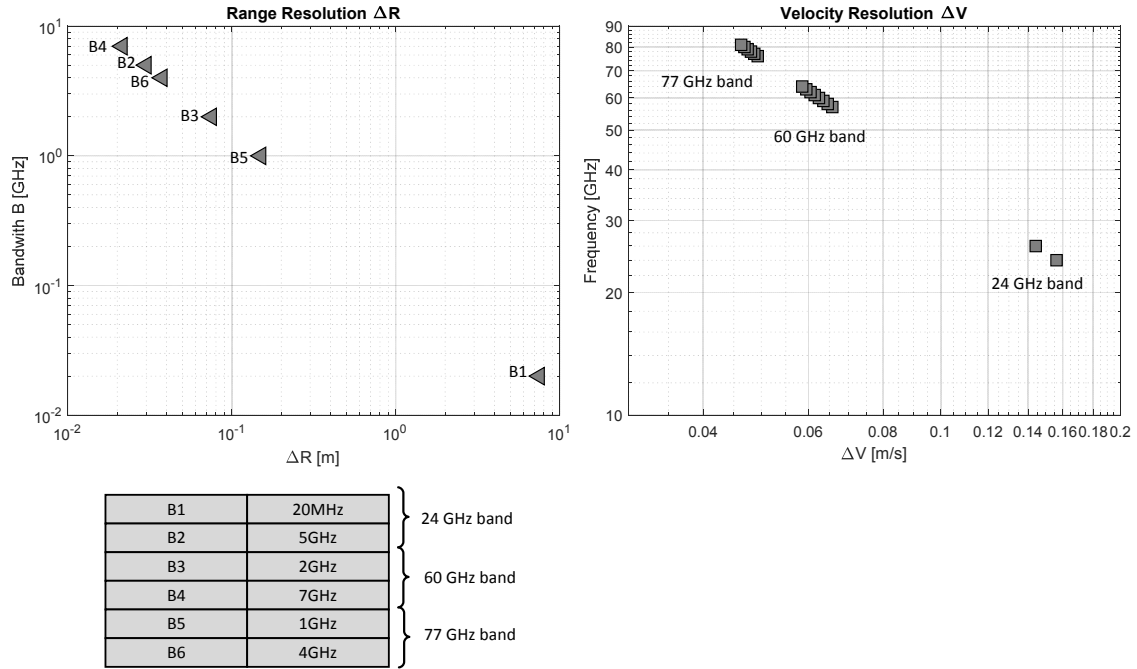


Figure 1.2: The relation of the range and velocity resolution at microwave and mm-wave frequencies. The data is obtained from [14].

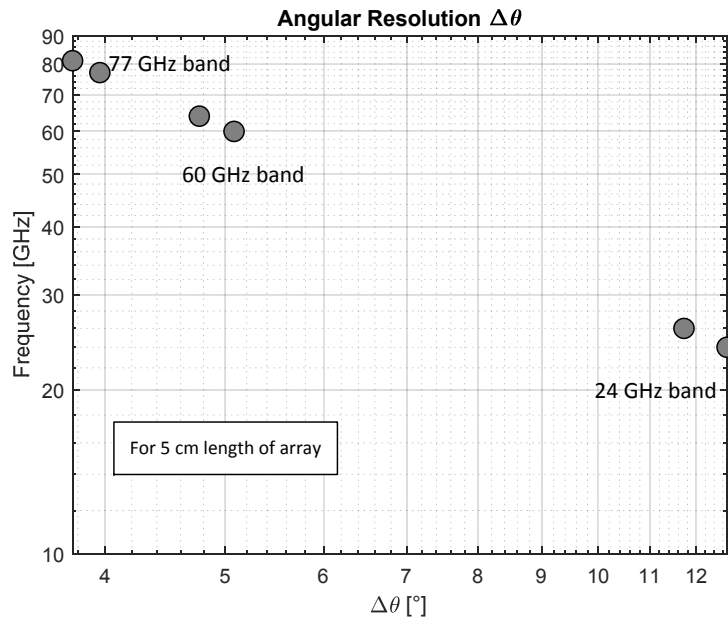


Figure 1.3: The relation of the angular resolution at microwave and mm-wave operating frequencies, where the length of the array is the same for all ranges. The data in the figure is obtained from [14].

will require a large number of elements. For example, in Fig. 1.3, for a 5 cm length of the array, the 24 GHz band will need two antenna elements in the array, while the 60 GHz band and 77 GHz band will need 20 and 30 antenna elements, respectively. Therefore, even though mm-wave frequencies provide higher resolution, they come with the challenge of high cost and complexity with large systems.

The alternative to phased-array radar, i.e. MIMO radar, is gradually taking precedence over traditional radars because of its inherent ability to provide higher resolution than an equivalent phased-array radar without increasing the number of elements, see [15]. Although MIMO radars give an advantage in terms of high resolution, it comes at the cost of increased power, larger array size and increased signal-processing cost. The next question is whether it is possible to break the limit of angular resolution in conventional MIMO radars through a sparse topology, while assuming that the transmit power, antenna gain, SLL and number of elements are not compromised.

1.3 Research objectives

The objective of this thesis is primarily to investigate and address the challenges of the design, integration and evaluation of a radar imaging system at mm-wave frequencies. When integrating radar chips and RF components at these frequencies for a MIMO radar design, the topology of these components requires considerable scrutiny as it affects performance measures, such as isolation, signal stability, and scanning capability. A promising technology is a sparse array topology of radar chips to achieve high resolution and better detection of the targets by radar imaging systems. The sparse array topology concept has the potential to improve the radiation properties of the array, such as improved beamwidth and high isolation, which translate into improved angular resolution. The main advantage of sparse arrays is that angular resolution can be improved without the increase of the number of array elements. However, sparse arrays also have the challenge of high side lobe level and grating lobes, which translate into false detection of the targets due to high interference. Thus, the goal in this thesis is to investigate methods to design a sparse topology that addresses and resolves these challenges. A part of this thesis research has been conducted at ASTRON (Netherlands institute of Radio Astronomy), during a four month research visit and the sparsity is then first analyzed to address the avoidance of grating lobes and better performance in receiving systems of radio telescopes, which can be considered as the receiving half of a radar system. Next, the sparsity is systematically exploited in MIMO radar systems, where both transmit and receive array topologies are designed to address the dilemma of high side lobe level and grating lobes in a sparse array. Further, a well-designed transmit and receive array in MIMO radar raises the question of experimentally vali-

dating such a system, for which a well-defined measurement strategy is desired without the need to build an entire and fully functional radar platform.

1.4 Research Activities

The research activities (RA) involved in the construction of this thesis are summarized as follows:

- RA1: Feasibility of a 60 GHz MIMO radar demonstrator:** Single-chip radar modules that include antennas-on-chip are attractive because of their small size and low-cost, but they also open up the opportunity to be used in a MIMO radar system. The idea brings in design challenges of the stability of the input reference frequency and the integration of components, as it affects the signal-to-noise ratio (SNR) of the received signals and hence the direction of arrival of the targets. This has been investigated and addressed with a complex 60 GHz demonstrator which has been designed and evaluated, see Chapter 3.
- RA2: Sparse array analysis for connected aperture arrays:** In order to explore interesting concepts for future automotive radars, the sparse array concept is used in astronomical application areas. For astronomical observations, connected aperture arrays are largely used for radio telescopes and Vivaldi antennas are a strong candidate because of their wide-band performance. However, in order to achieve a higher system sensitivity, a larger radio telescope is required with the number of antenna-array elements in the order of millions. Two concepts of regular and irregular sparse arrays are proposed and evaluated, which allow to reduce the number of elements to half as compared to a regular dense array, while keeping the system performance in terms of effective area and array noise temperature, see Chapter 4.
- RA3: Sparse virtual array synthesis for MIMO radars:** The concept of MIMO radars is becoming increasingly popular for radar imaging systems to achieve a higher angular resolution. MIMO radars inherently prove to have higher angular resolution as compared to phased-array radars [16], but in this thesis, the limit to achieve higher angular resolution in conventional MIMO radar is pushed further with the help of sparse virtual-array synthesis, see Chapter 5.
- RA4: Virtual array pattern measurements:** The experimental validation and characterization of a synthesized virtual array for a MIMO radar requires a complete radar platform, which is a tedious task. A method that emulates the TDM-MIMO mode of a MIMO radar using a two-port VNA and corresponding measurement

strategy is formulated and demonstrated to measure the radiation pattern and scanning capabilities of the virtual array for a defined transmit and receive array configuration, see Chapter 6.

1.5 Thesis outline

The remainder of the thesis starts with Chapter 2 that includes the theoretical background of the concepts required to support the content of the core chapters, i.e. Chapters 3 to 7. Chapter 3 to Chapter 6 address the four research activities, described in Section. 1.4. Chapter 7, presents the extension of Chapter 5 but for the planar array case. In Chapter 8, conclusions are drawn and recommendations for future work are listed.

1.5.1 Suggested method of reading

Fig 1.4 shows the outline of the thesis. Chapter 2 is self-contained and can be read independently. Chapter 3 needs the background information provided in Sections 2.1, 2.2, and 2.3. Chapter 4 is self-contained and can be read independently but Section 2.4 as prerequisite is preferable. Chapter 5 uses the technical knowledge from Sections 2.2, and 2.3, but can be read independently. Chapter 6 is also self-contained, but is better read after Chapter 5. Chapter 7, should be read only after chapter 5.

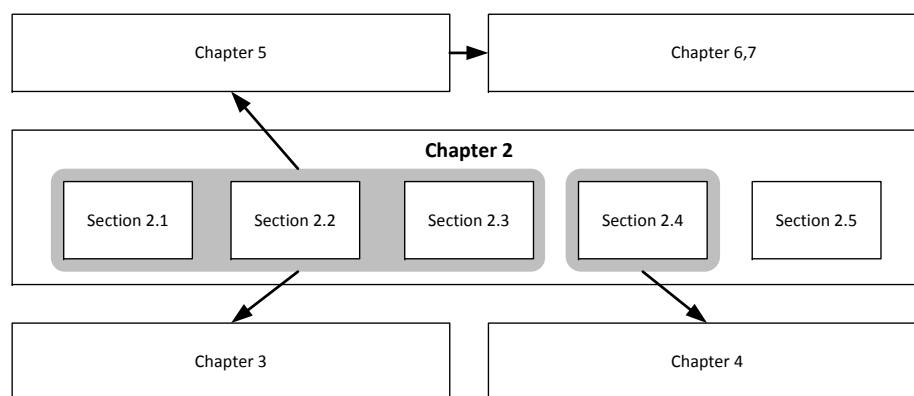


Figure 1.4: Outline of the thesis and suggested method of reading.

1.6 Original contributions of this thesis

The work presented in this thesis contains the following original contributions:

- The design and characterization of an FMCW MIMO radar demonstrator with 13 silicon-based radar chips in a linear array with the functionality of TDM MIMO mode.
- It is shown that a radar chip that has a complete RF front end and on-chip antenna can work well as a stand-alone device, but when put in close proximity to other radar chips and base-band components such as a DDS and a ADC, its performance can deteriorate.
- Two concepts of regular-on-grid and irregular-on-grid sparse array configurations are introduced for the connected Vivaldi aperture arrays for the Square Kilometer Array mid-frequency radio telescope.
- The effect the terminating impedance of inactive antennas has on the receiver noise temperature of a connected array of Vivaldi antennas is investigated.
- For MIMO radar imaging systems, two synthesis methods to determine the topology of the sparse transmit and receive arrays are proposed and validated with numerical examples. The arrays are either synthesized independent of each other or one dependent on the topology of the other. An improvement of a maximum of 3° in beamwidth and a maximum of 7 dB in side lobe level is reported in the examples.
- A measurement strategy for the characterization of the radiation pattern performance of a virtual array is developed by using only a two-port VNA and by emulating the TDM MIMO mode of a MIMO radar.

CHAPTER TWO

En route to MIMO radar

2.1 Introduction

Radar is an acronym for "**R**adio **D**etection and **R**anging" and, as name suggests, a system that uses electromagnetic waves to detect the moving and non-moving objects. The history of radar is as old as the discovery of radio waves. Christian Hülsmeyer, a German scientist, is considered to be the inventor of radar as he, in 1904, patented and developed the spark-gap transmitter-receiver system. However, a complete working radar system was first demonstrated by Robert Watson Walt, an English scientist, in 1935 [17]. Most of the early research in the field of radar was mainly carried out for military application during World War II, but radar in the civil sector also flourished in the 1940s. Since then, many techniques have been established and pulse radar with one antenna was the first to mature for search and track of single targets. Over the next 80 years, the field of radar has evolved and now radars are being used in commercial applications like automotive, security and medicine.

The basic principle of operation in radars is based on the reflection of electromagnetic waves from a target. The electromagnetic signal is transmitted and the reflected signal from the target is received. The time delay and change in the reflected signal frequency contains the information of the target's position, range and velocity. A typical commercial radar uses several integrated components. A basic block diagram of a typical radar is shown in Fig. 2.1. This basic system consists of antennas, an RF front end, and a base-band signal processing unit. The RF front end consists of a transmit unit that generates a transmit waveform and a receive unit that performs signal condi-

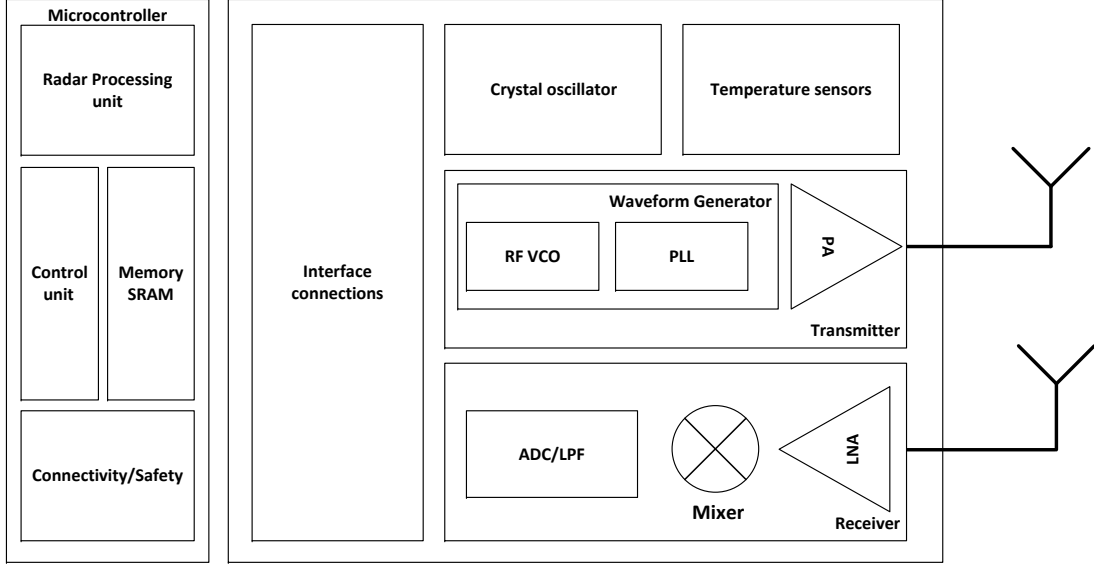


Figure 2.1: Block diagram of an RF radar system with a transmitter and a receiver, along with a signal processing unit. (VCO: voltage controlled oscillators, PLL: phased locked loop, PA: power amplifier, LNA: low-noise amplifier, ADC: analog to digital converter, LPF: low pass filter).

tioning. The RF front end is typically connected to a micro-controller for further radar signal processing and control.

The radar equation is an important equation for radar systems as it gives a relationship between the relevant parameters related to a radar, such as the transmit power and sensitivity of the receivers. The complete expression for the radar range equation is given by [18]:

$$R_{max} = \left[\frac{P_t G_t G_r \sigma_{tgt} \lambda_0^2}{(4\pi)^3 k T_0 B F(S/N)_{min}} \right]^{1/4}, \quad (2.1)$$

where P_t is the transmitted power at the transmitter, $(S/N)_{min}$ is the minimum detectable signal-to-noise ratio at the receiver input, σ_{tgt} is the radar cross section (RCS) of the radar target, G_t and G_r are the gain of the antennas respectively. The expression kT_0B represents the thermal noise where k is the Boltzmann constant, T_0 is the system temperature, λ_0 is the free-space wavelength, and B is the bandwidth of the radar system.

For determining the angular position of multiple targets and wider view angle, mechanical movement of a radar system was required which is tedious, slow and expensive.

To remove the curse of mechanical steering, phased-array radar systems were introduced and used to electronically steer the radar beam using multiple antennas to detect multiple targets rapidly or even simultaneously. Most recently, an advanced version of phased-array radars, namely Multiple-input Multiple-output (MIMO) radar systems, is gaining popularity.

2.2 Phased-array vs MIMO radar

2.2.1 Phased-array radars

A phased-array antenna is a multi-antenna system that allows electronic steering of the main beam towards a particular direction. Phased-array antennas use a phase shifter or true time delay [19] for each of the radiating elements, which shifts the phase of the signal of each radiating element and hence steers the beam in the desired direction. This electronic scanning eliminates the curse of mechanical scanning, thus giving rise to a broad range of applications for phased-array technology. For more than half a century, phased-arrays have been traditionally used in many military radar applications.

From antenna array theory, the antenna elements are placed in a periodic arrangement (dense configuration with $\lambda_0/2$ spacing) in order to make the beam pattern more directive and avoid the appearance of grating lobes in the field-of-view (FOV). The added functionality of altering the phase of each element allows constructive and destructive interference of the signals from the individual elements, hence resulting in electronic beam steering. A linear array of N isotropic elements equidistantly positioned along a straight line is shown in Fig. 2.2. Each element is fed with a harmonic signal described by an amplitude and phase, which results in a local plane wave in the far field region either at broadside (top case in Fig. 2.2) or at an angle θ_0 (bottom case in Fig. 2.2). By combining all the transmitted signals from the individual elements in the far field, the array factor of this linear array is given by

$$S(\theta) = \sum_{n=1}^N |a_n| \exp\{jk_0(n-1)d \sin \theta - j\Phi_n\}, \quad (2.2)$$

where $k_0 = 2\pi/\lambda_0$ is the free-space wave number, d is the distance between the elements, $|a_n|$ is the amplitude weighting and Φ_n is the phase-shift term of the n_{th} array element [19]. In order to steer the array factor in the desired direction, the phase term Φ_n of the n_{th} element must be

$$\Phi_n = k_0(n-1)d \sin \theta_0, \quad (2.3)$$

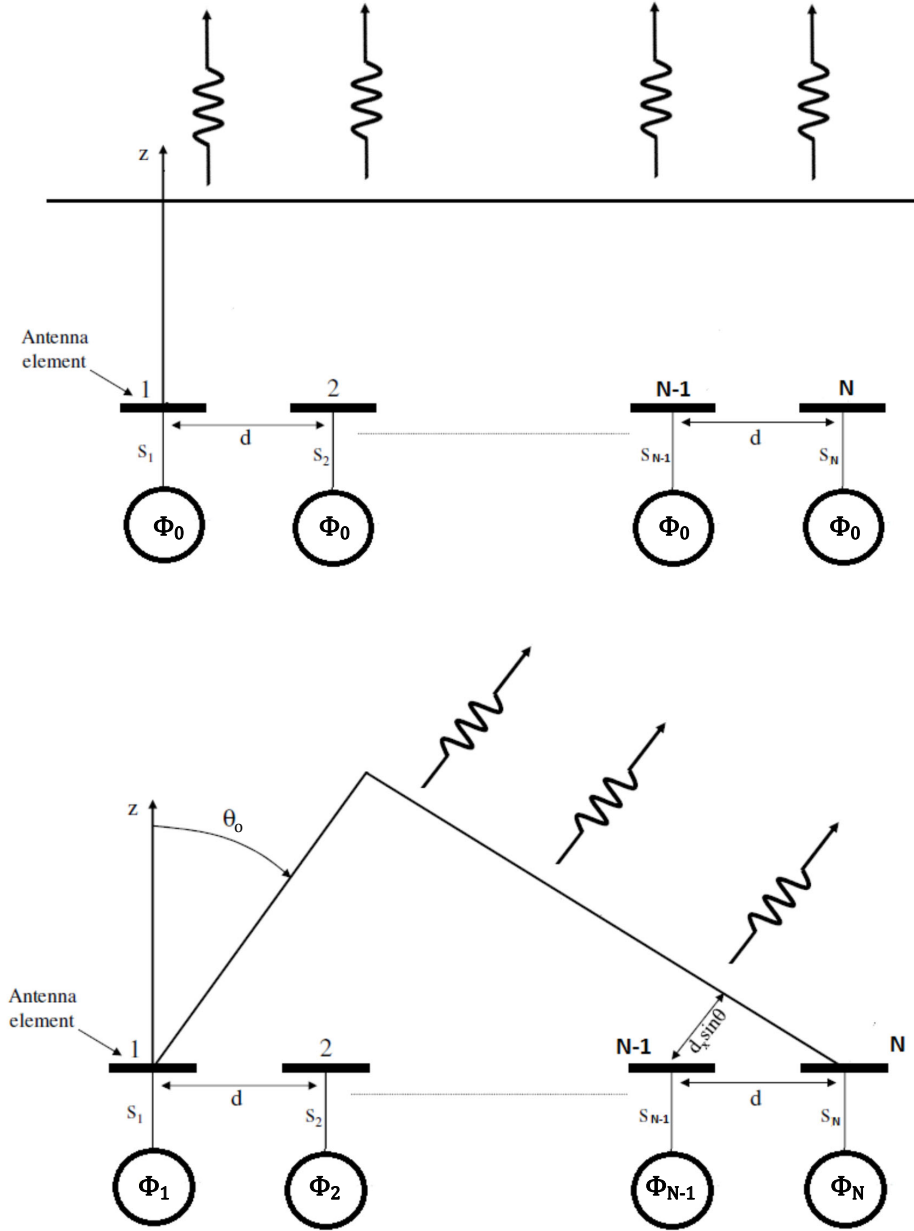


Figure 2.2: Linear phased-array of N isotropic elements equidistantly positioned along a straight line. (top) Feeding with same phase and (bottom) feeding with a linearly progressing phase difference to steer to an angle θ_0

where θ_0 is the desired steering angle. Thus, putting this value into (2.2) gives the maximum of the array factor in the desired direction. If the amplitude weights $|a_n|$ are all equal, then the array is said to have uniform tapering [20]. To reduce the side lobe level of the radiation pattern of the array, amplitude tapering can be used [20].

In the field of radar, phased-array radars are used for steering the beam of the radar antenna system without mechanically moving the radar antenna for the direction information of the target. Mainly two types of phased-array systems are used in radar antennas, as briefly explained below.

Passive electronically steered array (PESA)

The PESA, also known as passive phased-array, is a phased-array antenna system that steers the beam electronically and in which each individual antenna element in the array is connected to a single transmitter and/or receiver through passive phase shifters.

Active electronically steered array (AESA)

An AESA is a more advanced and sophisticated generation of the PESA and differs from a PESA in the sense that each antenna element is connected to a separate transmitter and/or receiver, which is computer controlled.

2.2.2 Limitation of the phased-array

From the theory of phased-arrays we know that in a uniformly excited antenna array, a maximum distance between antenna elements of λ_0 between the array elements is acceptable in order to avoid grating lobes when the array is not scanning, i.e. the main beam is pointed towards broadside. However, in case of scanning this limitation on the maximum distance between elements reduces to $\lambda_0/2$ [19].

Moreover, for high gain and narrow beamwidth, the array aperture must be increased and hence the number of antenna elements in the array. The relationship between the array beamwidth and array aperture is given by [21]

$$\Delta\theta = 0.89 \frac{\lambda_0}{D}, \quad (2.4)$$

where $\Delta\theta$ is the half power (3 dB) beamwidth (in radians) and D is the maximum diameter of the aperture of the array, which can be approximated by Nd (d being the distance between the elements) in case of a linear array.

The limitation of $\lambda_0/2$ spacing in case of radar systems, where you need a very high antenna gain to realize a large range and high angular resolution for uniquely identifying the object, results in a very large number of array elements and hence the systems will become bulky, expensive and power hungry. One solution to this problem is the use of sparse arrays instead of dense arrays, but these also suffer from grating-lobe issues [22].

Recently, MIMO (Multiple Input Multiple Output) arrays in radar systems have gained considerable popularity because of their advantage over conventional phased-

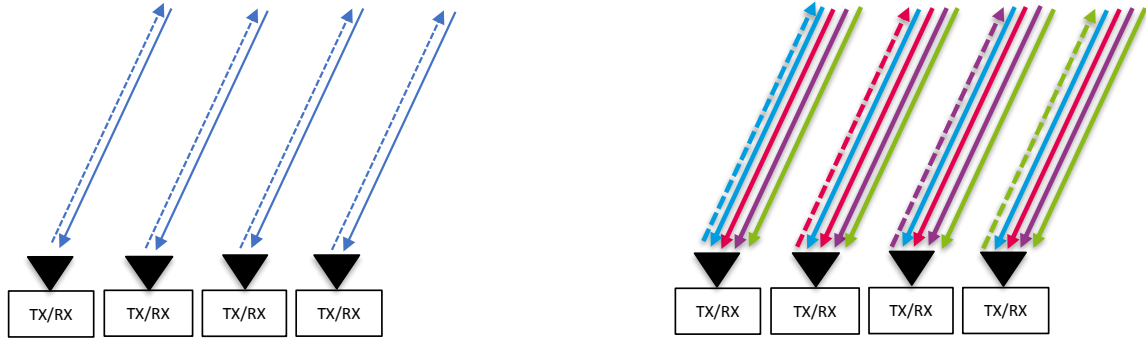


Figure 2.3: Transmit signal (dashed line) and received signal (solid line) representation for AESA (left) and MIMO array (right). The same (blue) color for AESA transmit signals represent coherent transmission and multi-color transmission in MIMO represents orthogonal transmit signals.

arrays. This thesis concerns mainly the study of MIMO radar systems and virtual array antennas, which will be explained theoretically in the following sections.

2.2.3 MIMO radar

The fundamental principle of MIMO radar involves the orthogonal signal transmission from all the transmitters and the reception of all the orthogonal responses from the targets, by all the receivers, as compared to a phased-array radar that involves the coherent transmission of signals from all the transmitters and the coherent reception of the responses from the targets. This results in a virtual MIMO array with an array aperture larger than the array aperture of an equivalent phased-array. A basic diagram showing the difference between phased-array (AESA) and MIMO radar is shown in Fig. 2.3. A MIMO array generally can consist of a transmit array and a receive array. Like in an AESA, each individual array element in a MIMO array has its own transmitter and receiver. In case of AESA, a coherent signal is transmitted from each transmitter and the received signal is the same at each receiver, apart from a potential time delay. On the left side of Fig. 2.3 this is shown by a single blue color which represents the coherency. Hence, the array aperture is the same as that of the receiver array. Contrary to this, in MIMO radars, from the transmitter of each individual array element, an orthogonal signal is transmitted and each receiver receives all the reflected orthogonal signals. This is represented by different colors on the right side of Fig. 2.3. This results in the formation of a MIMO virtual array with a number of array elements larger than that of the actual physical transmit and receive array. Hence the array aperture is larger than the actual physical arrays and results in a narrower beamwidth and higher angular

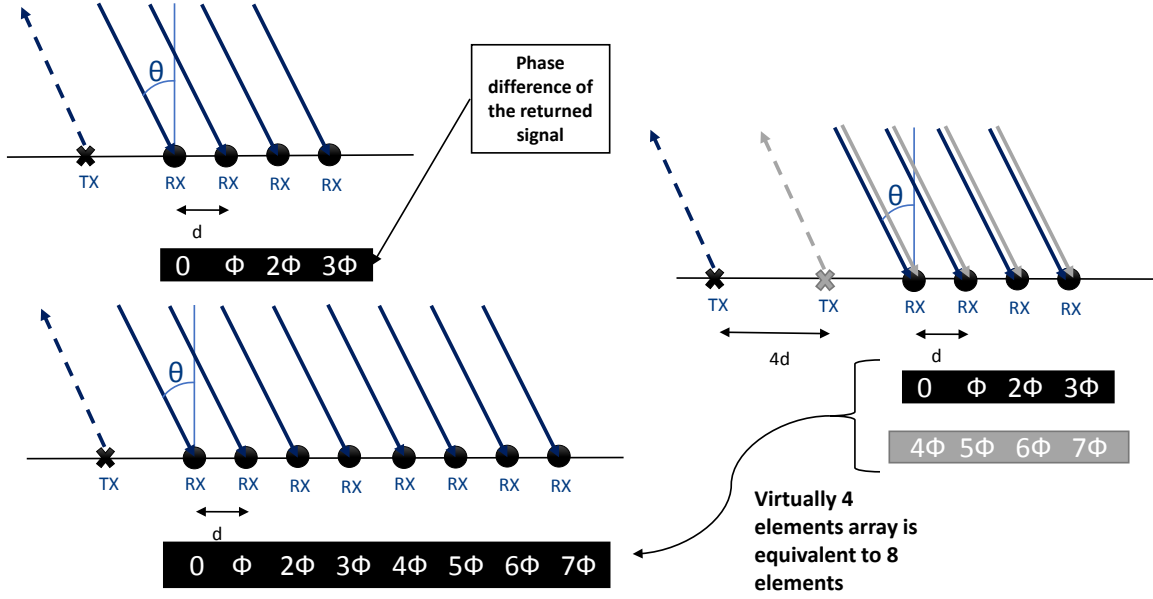


Figure 2.4: Left top: SIMO with one transmitter and four receivers. Left bottom: SIMO with one transmitter and eight receivers. Right: MIMO with two transmitters (with different signals represented by dark shade and light shade) and four receivers.

resolution.

Concept of MIMO virtual array

To explain the concept of the virtual array in MIMO radars and describe the formation of a larger aperture array as compared to a phased-array, a single-input-multiple-output (SIMO) radar is first considered, which is similar to an AESA with a single transmitter and multiple receivers. The description is based on Fig. 2.4. We assume that the target is located in the far-field region of the SIMO radar.

A SIMO radar is a radar with one transmitter and multiple receivers and the angular resolution depends on the number of receive antennas and the inter-element distance between the receive antennas. As an example, for a SIMO radar of four receive elements with an inter-element distance of d as shown in the top left of Fig. 2.4, the progressing phase shifts in the received signal that is reflected by the target at an angle θ are $\{0, \Phi, 2\Phi, 3\Phi\}$, with reference to the first element. This signal phase at each receiver is determined and the angular position of the target can be estimated by performing an angle-FFT. From Equation (2.4), the angular resolution of the radar, can be increased by increasing the number N , which is the number of receive ele-

ments in the SIMO case. Thus, a SIMO radar with eight receive elements, as shown at the bottom left of Fig. 2.4, has received signals with progressing phase shifts of $\{0, \Phi, 2\Phi, 3\Phi, 4\Phi, 5\Phi, 6\Phi, 7\Phi\}$. By performing an angle-FFT on these received signals a better angular resolution is achieved.

Now, a MIMO radar is considered with two transmitters and four receivers as shown on the right side of Fig. 2.4. The two transmitters are placed at an inter-element distance of $4d$, while the four receivers have an inter-element distance of d , the same as the receivers in the case of SIMO. A signal from the first transmitter results in the received signals with phase shifts of $\{0, \Phi, 2\Phi, 3\Phi\}$ and the signal from the second transmitter, being at a distance $4d$, results in the phase shifts of $\{4\Phi, 5\Phi, 6\Phi, 7\Phi\}$. In comparison, there are then collectively eight different received signals for the MIMO radar, which have phases equivalent to the SIMO radar with eight elements. Therefore, even though the MIMO radar has four physical receivers, because of an extra transmitter that transmits a different signal, the angular resolution of the MIMO radar is equivalent to that of the SIMO radar with eight physical elements (2×4).

Generalizing the discussion, if there are N_t transmit elements with inter-element spacing d_t and N_r receive elements with inter-element spacing d_r in a MIMO radar, then the number of virtual elements is $N_t \times N_r$. Thus, by employing MIMO radars, there is an N_t times increase in the number of (virtual) elements and hence the angular resolution is improved.

2.3 Technical background on MIMO radar

The general idea of MIMO radars is explained in Section 2.2.3. Like phased-array radars, MIMO radars consist of a transmit array and a receive array. The transmitted signal from each transmitter is orthogonal to all the others and the received signals at each receiver are then the reflections of all the transmitted signals that occur at the target. This requires a signal model to be developed, which is formulated in Section. 2.3.1. Note that in the rest of the thesis, an ideal environment is assumed where a single radar platform is present and the interference from other radar platforms and communication systems are not present. Furthermore, a large signal-to-noise ratio at the receiver is assumed. It is important to mention that in commercial car-radar applications non-ideal environments will become more and more important in future scenarios, since we expect that in the near future the majority of cars will be employed with radar sensors.

2.3.1 Mathematical formulation of MIMO radars

Consider a MIMO radar with colocated linear transmit and receive arrays, both oriented along the x -axis. The two arrays are colocated such that they are separated by a small distance in the y -direction, which is negligible as compared to the distance between the radar and the targets. Let there be N_t transmit elements, N_r receive elements and K targets. We will assume that the transmitter and receivers are synchronized. The base-band transmit signal at the target position is then given by the expression

$$\mathbf{s}[n] = \sum_{m=1}^{N_t} x_m[n] \exp(-j2\pi f_0 \tau_{m_t}(\theta)) = \mathbf{a}_t^*(\theta) \mathbf{x}(n), \quad (2.5)$$

where $x_m[n]$ is the discrete-time base-band signal of the m_{th} transmitter, τ_{m_t} is the time-delay from the m_{th} transmitter to the target, f_0 is the center frequency and $(.)^*$ represents the conjugate transpose. \mathbf{a}_t represents the transmit array steering vector given by expression

$$\mathbf{a}_t(\theta) = [e^{j2\pi f_0 \tau_1} \quad e^{j2\pi f_0 \tau_2} \dots \quad e^{j2\pi f_0 \tau_{N_t}}]^T, \quad (2.6)$$

where the m_t^{th} transmit signal time delay is given by

$$\tau_{m_t} = \frac{\mathbf{d}_t[m_t] \sin \theta}{c}, \quad (2.7)$$

where \mathbf{d}_t is the vector containing the inter-element distance of the transmit array, $\mathbf{d}_t[m_t]$ is the m_t^{th} element of that vector, and c is the speed of light.

The transmit signal in (2.5) is then reflected from the target and is received by all the receivers. The signal at the output of the receive array is given by the expression

$$\mathbf{y}[n] = \sum_{k=1}^K \beta_k \mathbf{a}_r^c(\theta) \mathbf{a}_t^*(\theta) \mathbf{x}[n] + \mathbf{w}[n], \quad (2.8)$$

where β_k is the complex RCS amplitude of the k_{th} target, $(.)^c$ is the complex conjugate, and \mathbf{w} is the white Gaussian noise. Note that interference between different radar systems is ignored here. \mathbf{a}_r represents the receive array steering vector given by the expression

$$\mathbf{a}_r(\theta) = [e^{j2\pi f_0 \tau_1} \quad e^{j2\pi f_0 \tau_2} \dots \quad e^{j2\pi f_0 \tau_{N_r}}], \quad (2.9)$$

where the m_r^{th} received signal time delay (from target to the receiver) is given by

$$\tau_{m_r} = \frac{\mathbf{d}_r[m_r] \sin \theta}{c} \quad (2.10)$$

where \mathbf{d}_r is the vector containing the inter-element distance of the receive array, and $\mathbf{d}_r[m_r]$ is the m_r^{th} element of the vector.

The received signal in (2.8) then contains the angular information of all the targets and the matrix multiplication expression, followed by vectorizing the matrix ($\text{vec}(\mathbf{a}_r^c \mathbf{a}_t)$), which can be interpreted as the virtual array steering vector given by the expression

$$\mathbf{a}_v(\theta) = [e^{j2\pi f_0 \tau_1} \quad e^{j2\pi f_0 \tau_2} \quad \dots \quad e^{j2\pi f_0 \tau_{N_v}}], \quad (2.11)$$

where N_v is the number of virtual array elements and the corresponding time-delays are

$$\tau_{m_t, m_r} = \frac{[\mathbf{d}_t[m_t] \sin \theta] + [\mathbf{d}_r[m_r] \sin \theta]}{c}, \quad (2.12)$$

for all the path combinations, i.e. the path from the m_t^{th} transmit element to the m_r^{th} receive elements. Note that the mapping between equation (2.11) and equation (2.12) is $\tau_1 = \tau_{1,1}$, $\tau_2 = \tau_{1,2}$, \dots , $\tau_{N_r} = \tau_{1,N_r}$, \dots , $\tau_{N_v} = \tau_{N_t, N_r}$. By this definition, the positions of the virtual array elements can be determined from the positions of the transmit and receive elements. So, if p_{m_t} is the x -coordinate of the m_t^{th} transmit element where $m_t = 1, 2, 3, \dots, N_t$ and p_{m_r} is the x -coordinate of the m_r^{th} receive element, where $m_r = 1, 2, 3, \dots, N_r$, then the x -coordinate of the pertaining element in the virtual array is $(p_{m_t} + p_{m_r})$ for each combination of m_t and m_r .

Equation (2.8) shows that the virtual array steering vector is simply the product of the steering vectors of the transmit and receive arrays. In antenna terminology this corresponds to the radiation patterns of the transmit, receive and virtual arrays. Further, the positions corresponding to Equation (2.12) are all the possible combinations of the transmit and receive positions.

2.3.2 Modes of operations for MIMO radars

The mathematical formulation of the signals in MIMO radars, as discussed in Section 2.3.1, is based on the assumption that the transmitted signals from all the transmitters are orthogonal to each other. In order to achieve this orthogonality, a MIMO radar can generally have three modes of operation.

Time Division Multiplexing

In the time division multiplexing (TDM) mode, the transmit signals originating from different transmitters are transmitted sequentially and the reflected signals from the

targets are received at all receivers simultaneously. An example of a MIMO radar operating in TDM mode is used in [23]. Although, TDM is the most commonly used mode in MIMO radars, achieving a perfect orthogonality is challenging since the multipath reflections and reflections from moving targets can result in additional time shifts, that need to be considered, and involves more resource usage.

Frequency Division Multiplexing

For the frequency division multiplexing (FDM) mode in MIMO radars, the orthogonality is achieved in the frequency domain. The bandwidth with which the radar platform can operate is divided into small frequency bands equal to the number of transmit elements and then the transmit signals from different frequency bands are transmitted simultaneously and the reflected signals from the targets are received at all receivers simultaneously [24]. Like the TDM mode, achieving pure orthogonality is also challenging because of the Doppler shifts due to moving targets, and hence results in more resource usage.

Phase Division Multiplexing

For the phase division multiplexing (PDM) mode in MIMO radars, the orthogonality is achieved in the phase domain. Unlike FDM, the bandwidth under which the radar platform can operate is fully used by each transmitted signal, but the transmit signals are made different by transmitting signals with different orthogonal codes with phase modulation and the reflected signals from the targets are received at all receivers simultaneously [25, 26]. In comparison to TDM and FDM mode, this mode results in maximum orthogonality between transmit signals, but it still requires more resource usage.

2.3.3 Target detection in MIMO radars

Like phased-array radars, the aim for MIMO radars is to detect the three aspects of targets present in their vicinity; range, velocity and angular direction. In this thesis, for the sake of simplicity, the focus is only on static targets, so only the range and angle detection are explained.

Range calculation using FFT

As explained in Section 2.1, the range of a target is defined as the distance between the target and the radar platform. Most MIMO radars employ the principles of either frequency modulated continuous wave (FMCW) radars or phase modulated continuous wave (PMCW) radars for their waveform selections. In both cases, the transmitted signal has a certain bandwidth and is either modulated in the frequency domain or the phase domain, respectively. In case of FMCW radars, the signal $\mathbf{x}[n]$ in (2.5) is a modulated signal vector which at the receive element contains a time shift because of the range of the target. In order to determine the range of the target from the received signal, a simple FFT is performed in the time-domain, resulting in a baseband frequency spectrum, with maximum peak at the frequency corresponding to the range of the target and this range is calculated as [27]

$$R = \frac{f_b c}{2\alpha}, \quad (2.13)$$

where f_b is the base-band frequency and α is the slope of either the frequency-time relation in the transmit waveform [18].

Target angle detection using digital beamforming (phase compensation)

Angle detection of the target refers to the angular position of the target with reference to the radar platform and is determined in one dimension in case of a linear array and in a two dimensions (azimuth and elevation) in case of a planar array. The conventional method of determining the angular information on the position of the target is to use the digital beamforming concept [21, 28], which involves the compensation of the phase shifts introduced in the received signals because of the angle θ_k of the target in (2.8).

In the digital beamforming for MIMO radars, the exact element positions and hence the array factors for both the transmit and receive arrays need to be known in order to compensate for the phase shift in the received signals and the resulting accumulative signal has a maximum at the angle θ_k .

Target angle detection using FFT, NUFFT and super-resolution algorithms

Although digital beamforming is the most common method used for the angle detection of the target and has been solely used in this thesis, there are other methods that can be employed by the signal processing section of a radar platform. For instance, like range determination, angular detection of the target can be obtained by performing a

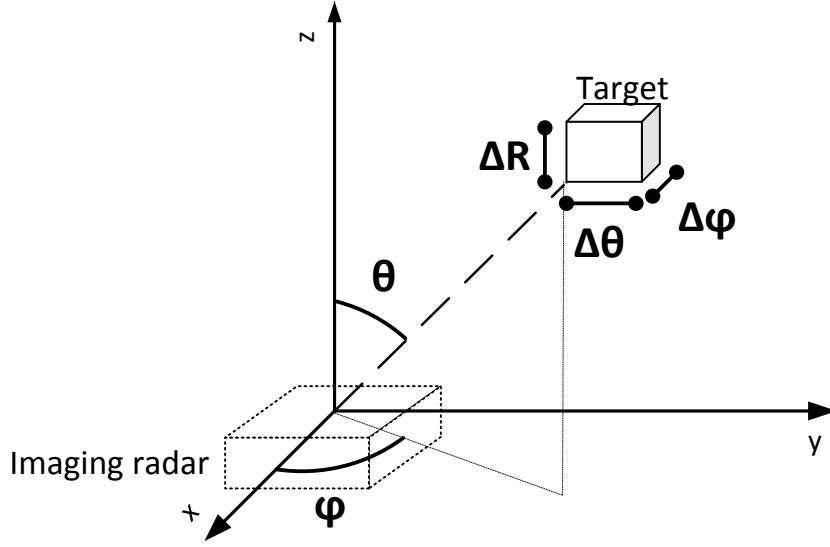


Figure 2.5: Resolution of the radar imaging system is determined by range resolution (ΔR), and angular resolution (both azimuth $\Delta\theta$ and elevation $\Delta\varphi$).

1D FFT on the angular domain of the received signals of a linear array or a 2D FFT on the angular domain of the received signal of a planar radar. Such an operation is also known as angle-FFT [28].

Note that the FFT is performed for the case when both transmit and receive arrays are regularly spaced. For the case of irregular sparse arrays, the less-known version of the non-uniform FFT (NUFFT) can be used [12]. Moreover, extensively established super resolution algorithms such as MUSIC [29] and ESPRIT for angle detection are alternatives that can also be used in MIMO radars [30].

2.3.4 Resolution of a radar imaging system

Imaging radars aim to detect multiple targets in order to create a camera-like three dimensional image from RF signals. Thus, identifiability of targets in a three dimensional domain for radar systems is dependent on the quality of the detection and is determined by the resolution of the radar system. The parameters that influence the resolution of the imaging radars are range resolution (ΔR), and angular resolution (both azimuth $\Delta\theta$ and elevation $\Delta\varphi$) as shown with the coordinate system in Fig. 2.5.

The range resolution of a radar depends on the bandwidth of operation B of the radar and is given by the inverse relation [18]

$$\Delta R \leq c/2B. \quad (2.14)$$

This equation assumes a static target. The angular resolution of the MIMO radar is estimated using the Rayleigh criterion, defined for azimuth and elevation resolution as [19]

$$\Delta\theta = 1.22 \frac{\lambda_0}{L_{vx}}, \quad \Delta\varphi = 1.22 \frac{\lambda_0}{L_{vy}}, \quad (2.15)$$

where L_{vx} and L_{vy} is the virtual array aperture size in the x -direction and y -direction, respectively. Comparing (2.15) with (2.4) suggests that the resolution of the imaging radar is equivalent to the 3 dB beamwidth of the radiation pattern of the virtual array pattern. Note that in rest of the thesis, the angular resolution and 3 dB beamwidth of the radiation pattern of an array are interchangeably used.

Although the resolution of the radar is an important figure of merit, the unique identifiability of the targets is an equally important performance metric for imaging radars. In radar terminology, it means that the radar platform should not be susceptible to ghost targets. Two aspects in radar can manage this requirement, one is a signal-processing aspect which uses techniques like adaptive array signal processing [31] for null-steering and generalized side-lobe canceller to eliminate the possibility of detecting unwanted targets. The second is the physical antenna array concept of grating lobes, which appear in the array pattern if the antenna element positions in the array are not properly designed. Also, the side lobe levels (SLLs) in the array patterns play an important role in the appearance of unknown targets in the field-of-view of the radar system. Higher SLLs make a radar more susceptible to the appearance of ghost targets in a radar image. Therefore, for MIMO radars, no grating lobes and low SLL in the virtual array pattern are the key design parameters that are considered in this thesis, to obtain better resolution of the radar platform.

2.4 Technical background on antenna array sparsity

One of the main research aspects of this thesis, explained in Chapter 1, is to investigate the improvement in the resolution of MIMO radars with the use of antenna array sparsity in the design of virtual array configurations. In order to avoid confusion in the rest of the thesis, a few terminologies are defined below that are frequently used.

Dense and sparse arrays

When an array has an inter-element distance equal to or less than $\lambda_0/2$, it is referred to as a dense array and when the inter-element distance is more than $\lambda_0/2$, it is called

Table 2.1: Four different types of array configurations: dense regular, sparse regular, dense irregular, and sparse irregular

	Dense	Sparse
Regular	regular grid with $\lambda_0/2$ or less spacing	regular grid with more than $\lambda_0/2$ spacing
Irregular	irregular grid with $\lambda_0/2$ or less spacing	irregular grid with more than $\lambda_0/2$ spacing

a sparse array.

Regular and irregular arrays

A regular array is one where each element of the array is placed on a regular grid and the inter-element distance is the same for all adjacent elements. However, in case of irregular arrays, the elements are placed on an irregular grid and the inter-element distance is different for adjacent elements.

The four different types of array configurations that are possible for a transmit or receive array in MIMO radars are given in Table 2.1

2.4.1 Antenna array sparsity

Antenna array sparsity is the synthesis process of the antenna array pattern where constraints on the beamwidth (directivity) and SLL are placed to determine a new configuration of the antenna array which is sparse and has a desired array pattern [32]. A number of algorithms exist in literature for the synthesis of sparse antenna configurations, such as the deterministic synthesis procedure in [33, 34], global optimization algorithms in [35], randomly rotated linearly polarized antennas in [36], antenna selection by solving combinatorial problems in [37] and iterative convex optimization in [32, 38–40].

The use of convex optimization for antenna array pattern synthesis was first introduced by H. Lebrete and S. Boyd in [32] and has by now been extensively used by several design engineers for antenna array synthesis [41–43]. In this thesis, convex optimization has also been used and made the basis of the algorithms developed in Chapter 5, particularly because of its numerical efficiency and ease of use. For a linear antenna array, the optimization problem formulation for the sake of achieving sparsity and the solution through convex optimization is illustrated below. Note that by achieving sparsity, in the context of this thesis, it is meant that the number of antenna array elements is reduced for the same array pattern performance, such as half-power beamwidth, side lobe levels, gain and wide scan range.

Consider a linear array of isotropic antennas with N elements. The array factor of such an array is given by

$$AF = \sum_{n=1}^N w_n e^{jk_0 d_n \sin \theta}, \quad (2.16)$$

where d_n is the n^{th} element position and w_n is the complex-valued weight coefficient of the n^{th} antenna element in the array.

The optimization problem for the sparse array synthesis of this linear array involves minimizing the number of non-zero elements of the vector \mathbf{w} that contains the weight coefficients, while keeping the beam pattern of the linear array as required (fixing the shape of the beam, beamwidth and side lobe levels). Such an optimization problem is an ℓ_0 -minimization problem and is formulated as [32]

$$\begin{aligned} & \min_{\mathbf{w}} \|\mathbf{w}\|_{\ell_0} \\ & \text{subject to} \\ & AF(\theta_{\max}) = 1 \\ & AF(\theta_s) \leq \text{SLL}, \forall \theta_s \notin [\theta_{\max} \pm \theta_{\text{FN}}] \end{aligned} \quad (2.17)$$

where θ_{\max} is the angle in the maximum radiation direction, θ_s contains the set of angles in the side-lobe region and θ_{FN} is the angle corresponding to the first null in the radiation pattern.

The formulation in (2.17), is a non-convex problem and is computationally hard. Therefore, it is relaxed by approximating it to an iterative weighted ℓ_1 -minimization problem, which is formulated as

$$\begin{aligned} & \min_{\mathbf{w}_i} \|\mathbf{Z}_i \mathbf{w}_i\|_{\ell_1} \\ & \text{subject to} \\ & AF(\theta_{\max}) = 1 \\ & AF(\theta_s) \leq \text{SLL}, \forall \theta_s \notin [\theta_{\max} \pm \theta_{\text{FN}}] \end{aligned} \quad (2.18)$$

where the diagonal matrix \mathbf{Z} is updated in every iteration, indicated by the subscript i , and the new value of the diagonal entries depend on the current excitation value i.e. $\mathbf{Z}_i = 1/(|\mathbf{w}_{i-1}| + e)$ where the division is understood element-wise on the diagonal of \mathbf{Z}_i and e is generally very small. This ℓ_1 -norm optimization problem thus is a convex problem and works by penalizing the larger weight coefficients more than the smaller coefficients, in the iteration process. Moreover, keeping $e > 0$ provides stability and prevents the zero-valued components in the excitation weights to avoid the non-zero estimate of w in next iteration [40].

The ℓ_1 convex optimization method for antenna array sparsity is numerically efficient and typically converges after few iterations. The termination criterion is chosen to be a threshold placed at the number of elements that reach a certain minimum expected weight value. If at the end of the iteration the selected number of elements have weight values lower than the set minimum value, then the solver terminates. Note that on such a formulation, there is a trade-off between beamwidth and SLL.

2.5 State-of-the-art on MIMO radar in radar imaging applications

The concept of MIMO radar technology has been in research for more than two decades now. The formal use of the term ‘MIMO radar’ appeared in literature by E. Fishler et. al in their paper ‘MIMO radar: An idea whose time has come’ [44]. Only recently this concept has been practically realized by the development of MIMO radar systems and demonstrators. These MIMO radar demonstrators have not only been developed for research purposes but they are increasingly available off-the-shelf in the commercial radar industry. Here we summarize MIMO radar systems that have been developed at different frequencies for many different applications and with many different approaches of design and functionality. An overview of MIMO radar demonstrators available in literature and market is presented in Table 2.2 and Table 2.3, respectively.

MIMO radar concepts have been extensively applied in research to develop mainly compact and small demonstrators with a small number of transmit and receive elements. The most prominently used mode of the MIMO radar has been TDM as it makes the implementations with the IC and signal processing much easier and less complex [10, 12, 23, 45–48]. However, some studies like [49–52] have developed innovative architectural designs for the FDM mode of MIMO radars, but these designs make the architecture of the demonstrator quite complex. Only recently, the PDM mode has been getting the focus of researchers as possible alternative to the FDM mode. Most of the research is focused on the application of MIMO radar in the automotive industry,

thus the frequency band of 76-81 GHz is mostly utilized. Although, for security applications, UWB frequencies are used for their large bandwidth. More recent state-of-art research in radars use frequencies of 100 GHz and above. Furthermore, from Table 2.2, it can be seen that the angular resolution of these radars increases when the number of transmit and receive channels is increased, either in a linear configuration or a planar configuration. Also, by comparing [10, 46–48] and [53] in Table 2.2, the advantage of using a sparse configuration is evident. [10, 46–48] use a planar configuration of the virtual array with 8×8 transmit and receive elements and an angular resolution of 6° is achieved. On the contrary, in [53], a linear configuration of the same number of transmit and receive elements is used, but because of the sparse configuration, the achieved angular resolution is 1.5° , four times better than in [10, 46–48].

The availability of MIMO radars in the industrial market has been gradually increasing over the past few years. During the earlier stages of development of a MIMO radar demonstrator, manufacturers like NXP [54] and Texas Instruments [55] only developed a version of a linear array of three transmit and four receive elements. These MIMO radars have the complete front end for all the channels on a single chip with a single PLL shared by all the receivers. An important functionality in these single chip MIMO radars is their ability to work in a cascaded master-slave system, with multiple of these single MIMO radar chips in an array, see [56]. Silicon Radar, in [57], claims to have achieved higher resolution of approximately 1° only in one dimension but it is important to note that such a high resolution with only two transmit and four receive elements has been achieved with the help high resolution algorithms like MUSIC and CAPON. However, there are also some fully 3D imaging radars from manufacturers like Vayyar and Arbe Robotics, which provide a high angular resolution and can be used for complete three dimensional imaging.

Reference	MIMO mode of operation	Transmit elements	Receive elements	Angular resolution	Range resolution	Virtual array orientation	TX/RX array aperture	FOV	Dense/Sparse configuration		Frequency of operation
									Transmit array	Receive array	
[12, 23]	TDM	4	4	$\approx 14^\circ$	-	Linear	Collinear	180°	Sparse	Dense	77 GHz
[10, 46–48]	TDM	8	8	$\approx 6^\circ$		Planar	T-shaped	$26^\circ \times 120^\circ$	Dense	Dense	24 GHz
[45]	TDM	12	13	$\approx 1.42^\circ$	≈ 1.25 cm	Planar	X-shaped	-	Dense	Dense	3–18 GHz
[58]	TDM	4	16	$\approx 3.45^\circ$	-	Planar	Square/collinear	120°	Dense	Dense	10–18 GHz
[59, 60]	TDM	22	22	$\approx 5^\circ$	≈ 2 cm	Planar	Square	-	Dense	Dense	100 GHz
[53]	TDM	8	8	$\approx 1.5^\circ$	≈ 1 cm	Linear	Collinear	-	Sparse	Sparse	160 GHz
[51]	FDM	6	8	-	-	Linear	Collinear	120°	Sparse	Dense	77 GHz
[49, 50]	FDM	4	4	$\approx 30^\circ$	-	Linear	Collinear	-	Dense	Dense	77 GHz
[52]	Orthogonal FDM	4	4	$\approx 30^\circ$	≈ 0.5 m	Linear	Collinear	-	Dense	Dense	77 GHz
[26]	PDM	3	4	-	-	Linear	Collinear	-	-	-	76–81 GHz

Table 2.2: An overview of MIMO radar demonstrators in literature

Reference	Manufacturer	Transmit elements	Receive elements	Angular resolution	Range resolution	Virtual array orientation	TX/RX array aperture	FOV	Dense/Sparse configuration		Frequency of operation
									Transmit array	Receive array	
[54]	NXP	3	4	$\approx 14^\circ$	≈ 3.75 cm	Linear	Collinear	-	Sparse	Dense	76-81 GHz
[55]	Texas Instruments	3	4	$\approx 14^\circ$	≈ 3 cm	Linear	Collinear	$60^\circ \times 40^\circ$	Sparse	Dense	76-81 GHz
[61]	Texas Instruments	3	4	-	-	Linear	Collinear	$60^\circ \times 120^\circ$	Sparse	Dense	60-64 GHz
[62]	InnoSent	-	-	$\approx 8^\circ$	-	Linear	Collinear	$75^\circ \times 13^\circ$	Dense	Dense	24 GHz
[57]	Silicon Radar	2	4	$\approx 1^\circ$	≈ 7 cm	Linear	optimized	-	-	-	24 GHz
[56]	Texas Instruments	12	16	$\approx 1.5^\circ$	-	Planar	Optimized	$60^\circ \times 120^\circ$	Sparse	Dense	76-81 GHz
[63]	Vayyar	20	20	$\approx 6.7^\circ$ Az and El	≈ 1.25 cm	Planar	L-shaped	$180^\circ \times 80^\circ$	Dense	Dense	62-64 GHz
[64]	Arbe Robotics	48	48	$\approx 1.25^\circ$ Az $\approx 1.5^\circ$ El	≈ 9.5 cm	Planar	-	$100^\circ \times 30^\circ$	-	-	76-81 GHz
[65]	Smartmicro	8	8	$\approx 15^\circ$	≈ 66 cm	-	-	$100^\circ \times 15^\circ$	-	-	76-77 GHz

Table 2.3: An overview of the MIMO radar demonstrators available off-the-shelf in the automotive market

CHAPTER THREE

A mm-wave MIMO radar demonstrator with an array of FMCW radar chips

Single-chip millimeter-wave FMCW radars with on-chip integrated antennas give rise to the idea of a multi-node radar system. Using these single-chip radars with their own transmitter and receiver and on-chip antennas comes with the challenge of integration and assembly of the components required for the functionality of MIMO radar modes. The design of a complete 60 GHz FMCW-MIMO radar demonstrator comprising an array of single-chip radars, signal conditioning components and signal processing capabilities, is presented. The system architecture of the demonstrator with the detail of the components needed for the functionality of MIMO radar is explained. For the synchronization between the transmitters and receivers, use of a single reference clock at low frequency is proposed. The prototype is evaluated and the measured results show that better SNR for the receivers of radar chips is required for lower phase errors and that a steady control of PLLs is required for clean generated mm-wave signal when a low-frequency reference is used.

3.1 Introduction

For short-range 3D environment scanning applications, be it in the field of security, medicine or automotive, radar imaging systems are commonly used, see Section 1.2. In state-of-the-art radar imaging systems, mm-wave frequency band is increasingly becoming popular and a list of such systems is presented in Table 2.2 and Table 2.3.

At mm-wave frequencies, the unlicensed ISM (industrial scientific and medicine) band of 60 GHz is a good candidate for radar imaging systems that can provide very high range and angular resolution, while keeping size and cost to a minimum. The large bandwidth (7 GHz) available in this band allows to have a range resolution in the order of 2 centimeter. It can be argued that for high angular resolution a large aperture is needed and due to a small free-space wavelength the number of array elements must be large in order to satisfy the spatial Nyquist sampling criteria. This problem can be solved by using a Multiple Input and Multiple Output (MIMO) radar technique, which allows to achieve a larger dense virtual array aperture even with a smaller non-regular physical aperture [11]. Hence, 60 GHz imaging systems are a potential small-size and low-cost solution for high-resolution radar imaging systems.

The advancements in semiconductor technologies at mm-wave frequencies have led to the development of a low-cost, low-power single-chip mm-wave radar with highly integrated transceivers and integrated mm-wave antennas [12]. This high level of integration gives rise to the idea of multi-node radar systems that consists of an array of single-chip radars. Due to the low-cost and low-power consumption of single chip radars, the MIMO radar systems have much potential in short- to medium-range consumer market applications.

We present a complete design and realization of such a multi-node radar system using multiple single-chip FMCW radars at 60 GHz as the individual elements of the MIMO radar system. Our demonstrator consists of a quasi-linear array of 13 single-chip 60 GHz radar chips, with one transmitter and two receivers with on-chip antennas [11] and three sections of supporting hardware for complete MIMO radar functionality. The challenge of synchronization between array nodes is addressed by using a low-frequency (50 MHz) single clock reference for all the radar chips. The designed application board is then evaluated for range measurements and the transmit phase-synchronization. Finally, a statistical analysis is performed to show that the phase tolerances of MIMO virtual arrays are better than that of phased-array radars.

3.2 TDM-MIMO FMCW radar

MIMO radar is a recent terminology used for multiple-antenna array radar systems like phased-array radars [66]. The main difference between a phased-array radar and a MIMO radar is that a MIMO radar transmits orthogonal waveforms from each of the transmitters and at the receiver side, every receiver receives the returned waveform of every transmitter. These can be distinguished because of the waveform orthogonality. The most common ways to implement orthogonality in the transmit waveform are Time Division Multiplexing (TDM) and Frequency Division Multiplexing (FDM). The transmitter and receiver arrays in the MIMO array system can be either widely separated or co-located. Further, in FMCW radar, the transmitted continuous wave signal is linearly frequency modulated and the received signal is mixed with the transmitted signal to achieve a baseband signal [30]. Combining these FMCW and MIMO radar concepts results in multiple transmit and receive FMCW radar pairs arranged in an array configuration such that all transmitters transmit orthogonal linear frequency chirps, which are separable at all receivers. In such a system, sophisticated signal processing algorithms like the Fast Fourier Transform (FFT) and Delay and Sum Beam-former (DSB) can then be used to detect the range and angular positions of the target. Here, we present the design of such an FMCW-MIMO radar demonstrator that consists of a waveform generator, a data acquisition module and a control module to evaluate the system in TDM mode. For such a system, an accurate synchronization of the transmitters and the receivers at 60 GHz is crucial and is implemented with a single reference clock at a lower frequency. The design is explained in the following sections.

3.3 60-GHz MIMO radar prototype design

The 60 GHz MIMO radar prototype consists of an array of 13 FMCW radar chips, each with its own transmit and receive sections, all implemented on a single PCB platform. Each radar chip has its own chirp generator and data acquisition section. To process the acquired data from the MIMO array, a signal-processing hardware platform, i.e. an FPGA development board, is used. Each section of the prototype is further explained in detail below.

3.3.1 System architecture functionality

The system architecture of the MIMO radar application board for the demonstrator, with the details of the components, is shown in Fig. 3.1 and the realized demonstrator

is shown in Fig. 3.2.

The application board generates a linear chirp at low frequency in the digital domain and converts it into an analog signal. This low-frequency chirp is then up-converted to the 60 GHz band and the RF signal is then transmitted. The received RF signal is down-converted to baseband frequencies, filtered and amplified. For processing, the received signal is converted into a digital signal and stored in an external device, i.e an FPGA. In designing the board, these functionalities were divided into three sections: the chirp-generator section, the 60 GHz RF radar-chip section and the data-acquisition section. These three functional sections are explained below.

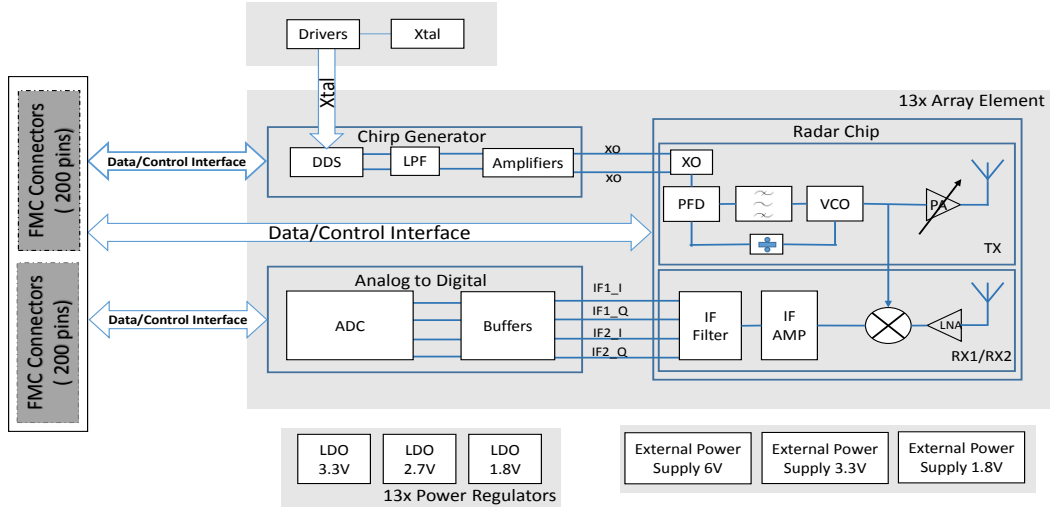


Figure 3.1: Block diagram of the MIMO radar application board consisting of a chirp-generator section, a radar chip and analog to digital converter, each for one of the 13 array elements. The FMC connectors on the left are for the FPGA connection to the FPGA board.

3.3.2 Chirp generation section

In FMCW radars, the range resolution of the target depends inversely on the bandwidth of the transmitted chirp. However, it has been shown in [28] that the range resolution degrades with the non-linearity of the chirp. Therefore, the linearity of the chirp is important and there are several techniques used to realize linearity in literature, see [67], for example via a look-up table, a phased locked loop (PLL) and a direct digital synthesizer (DDS). In our design, we use a DDS, since it can generate very accurate waveforms

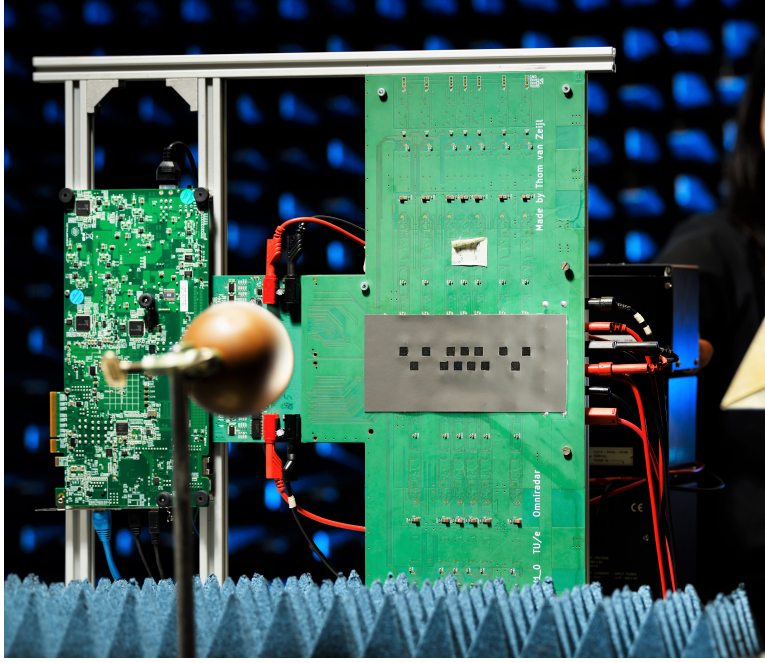


Figure 3.2: Front-view of the 60 GHz FMCW-MIMO radar demonstrator along with application board (on the right) and the FPGA system for post processing (on the left). Picture credits: Bart van Overbeeke.

of various frequencies and profiles such as up-chirp, down-chirp and bi-directional chirp. In a DDS, the waveform is generated first in the digital domain and then converted into the analog domain. The DDS used in our application board is from Analog Devices AD9913, which is fully programmable and generates a frequency-modulated linear chirp from 24 MHz to 26 MHz. This selection depends on the lowest phase noise at the reference frequency for the PLL of the radar chip, which is based on the study presented in [68].

3.3.3 60 GHz RF radar-chip section

The 60 GHz radar chip used in our system is the "One Chip Radar" developed by Omniradar, which is a fully integrated front-end radar with antennas-on-chip (AoC) [69, 70]. The radar provides a large bandwidth of 7 GHz (57 GHz to 64 GHz) and hence a high range resolution of approximately 4 cm. It has one transmitter and two receivers and the radar architecture is based on FMCW radar. The top view of the assembly of the radar IC package with on-chip integrated antennas is shown in Fig. 3.3. In this figure, the area indicated as "ground plane" for the monopole antennas represents the transmit and receive RF front end on the original radar IC assembly. The dimensions of the radar chip package are 7 mm \times 7 mm.

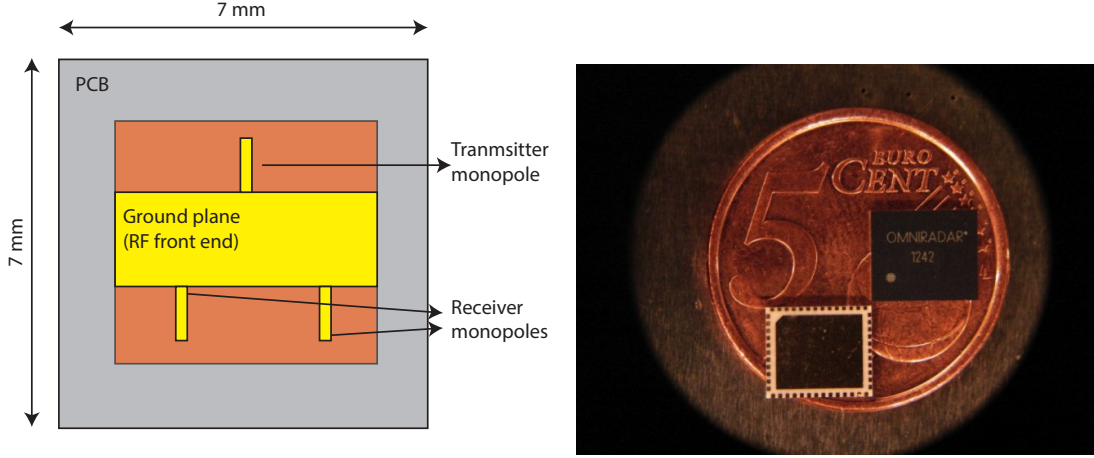


Figure 3.3: Left: transmit and receive monopole antennas on the silicon die (orange), and RF front-end modeled as a ground plane. The silicon die is mounted on a PCB (grey) as part of the IC package. Right: Omniradar 60 GHz radar chip.

There is an on-chip oscillator, which is fed with a low-frequency chirp from the DDS. Using the on-chip voltage controlled oscillator (VCO), frequency multiplier, programmable divider and PLL, this chirp is then up-converted to 60 GHz. By using a programmable power amplifier, the effective isotropic radiated power (EIRP) of the on-chip antenna can be varied. With a programmable mixer, low-noise amplifier, Intermediate Frequency (IF) amplifier and filter, the signal-to-noise ratio (SNR) of the received signal can be varied e.g. to save energy by reducing the transmit power in short-range applications. Further information on these radar chips and the on-chip antennas can be obtained from [11].

3.3.4 Data acquisition section

The data acquisition section consists of analog-to-digital converters (ADCs) and an FPGA for data storage and processing. The required ADC Nyquist bandwidth depends on the maximum of the IF signal and for FMCW radars this bandwidth can be derived from the relationship between the sweep slope and beat frequency. For example, for a bandwidth of 2 GHz, a chirp time of 1 ms, and maximum distance of 50 meters gives the maximum IF of the a FMCW radar to be 500 kHz (cf. Eq. (2.13)). This sets the requirements for the sampling rate of the ADC. Furthermore, an important feature included in the design is that the ADCs simultaneously sample all the receive IF channels for the synchronization. The analog quadrature IF data from the radar chips is then sampled and stored in the FPGA for further signal processing. A complete software module has been developed in verilog HDL and C-language, which allows the designer

to interact with and configure the radar chips, DDSs and ADCs, based on the required settings. Also, it allows the prototype to operate in TDM mode of MIMO radars. A very extensive debugging of the hardware was required to make the application board and its integration with software module completely functional. More details can be found on [30].

It is important to note here that the demonstrator consists of an array of 13 radar chips and each radar chip has its own chirp generator section and its own ADC, all of which are programmable through the external FPGA board. This allows the demonstrator to be flexible in functionality.

3.3.5 MIMO array of radar chips

The design of the MIMO array for the multi-node radar system presented in this study is challenging because contrary to a conventional array design, whose array elements are antennas, the MIMO array of our system uses single-chip radar nodes, with one transmit and two receive RF front ends with on-chip antennas, as a single array element. Use of these radar nodes puts a limitation on the distance between the individual elements for the design of the MIMO transmit and receive array. This challenge is addressed in this section.

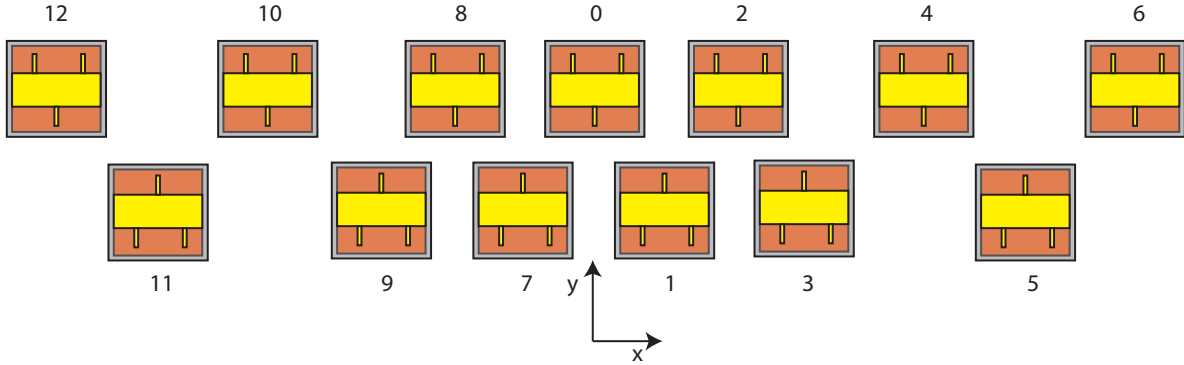


Figure 3.4: Non-regular sparse MIMO radar array configuration with two linear arrays.

The positions of the transmit and receive antennas on one chip are fixed. Also, the dimensions of the radar chip are fixed, which by including the landing pads are 12 mm \times 12 mm. Therefore, the limitations on transmit and receive antenna positions in terms of the free-space wavelength (λ_0) at 60 GHz are as follows:

- the minimum distance between two transmitters of two separate radar chips is

$$2 \cdot \lambda_0.$$

- the distance between two receivers on the same radar chip is $0.28 \cdot \lambda_0$
- the minimum distance between two receivers on two separate radar chips is $1.72 \cdot \lambda_0$

These limitations suggest that the transmit and receive antenna positions in a linear array of radar nodes can not fulfill the spatial Nyquist sampling criterion, which requires $\lambda_0/2$ spacing between the array elements to avoid grating lobes. Therefore, the array configuration of radar nodes must be non-regular sparse to avoid both grating lobes and high side-lobe levels [19]. For this reason, a non-regular quasi-linear sparse array of radar nodes has been designed that consists of two linear arrays, one with six radar nodes and the other with seven radar nodes, which amounts to a total of 13 transmitters and 26 receivers, see Fig. 3.4. The x and y positions of the radar chips are given in Table 3.1. Note that in Fig. 3.4, because of the placement of the radar chips in two linear arrays, the above listed limitations between the transmit and receive on-chip antennas has been overcome and the transmit monopole and receive monopole arrays form a triangular irregular grid in the x -direction. This results in a radiation pattern of the virtual array without high sidelobe levels and without grating lobes.

Table 3.1: x and y center positions of the radar chips on the non-regular sparse array grid.

Chip number	x -position (mm)	y -position (mm)
0	0	6
1 & 7	+/- 5.57	-6
2 & 8	+/- 11.81	6
3 & 9	+/- 17.38	-6
4 & 10	+/- 32.57	6
5 & 11	+/- 42.69	-6
6 & 12	+/- 51.81	6

More details on the optimization process of this sparse array and the corresponding radiation patterns of transmit, receive and virtual arrays can be found in [71]. In this chapter, the system level performance and limitations of the prototype as a whole are subsequently evaluated and presented.

3.4 Comparison of SIMO and MIMO direction of arrival

Using the formulation of the signal model for TDM mode of an FMCW-MIMO radar given in [10], we developed a Matlab model for the direction-of-arrival (DOA) estimation. Using the Matlab model, we compare DOA of different targets for three scenarios. First, we consider the scenario of single input multiple output (SIMO) for a dense array of 13 radar nodes, where one transmitter transmits a chirp and all the receivers receive simultaneously. Secondly, SIMO is used for our non-regular sparse array, and finally in the third scenario, we apply TDM-MIMO for our non-regular sparse array, see Fig. 3.4. The simulation results of DOA estimation for three targets at -50 , 20 and 30 degrees for all scenarios are shown in Fig. 3.5. It shows that by using the TDM-MIMO approach with the non-regular sparse array configuration, we can achieve an average side-lobe level comparable to that of a dense array, while maintaining the angular resolution, owing to the sparse array (with 3° improvement).

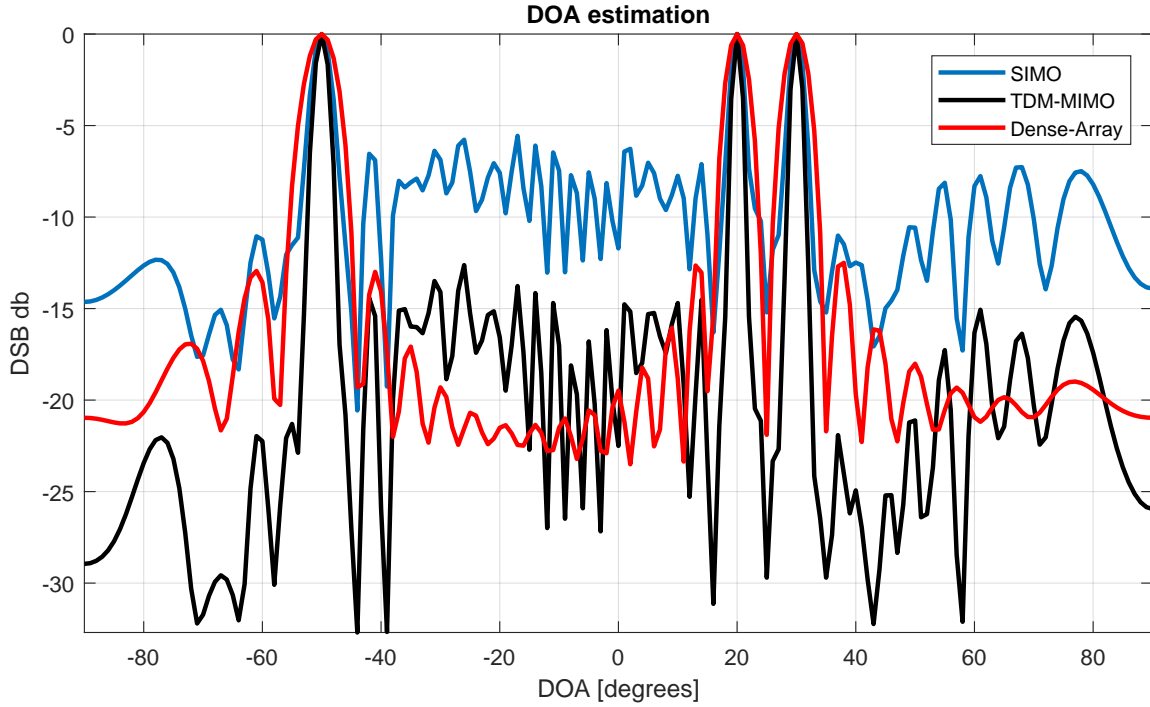


Figure 3.5: Beam patterns for DOA estimation of three targets located at 20 , 30 and -50 degrees, showing the comparison of three scenarios, i.e SIMO for a dense array, SIMO for the non-regular sparse array, and TDM-MIMO for the non-regular sparse array.

3.5 Performance and evaluation of the prototype

As explained before, the prototype of the mm-wave MIMO radar demonstrator has been designed for a TDM-MIMO mode of operation. This mode is possible because of the re-configurable power amplifiers on the radar chips. The transmitter of a particular chip that transmits a signal has its power amplifier "ON" (we call it transmitting chip) while all other radar chips do not transmit by turning their power amplifiers "OFF" (we call them silent chips). In order to evaluate the performance of the prototype, we measured the range profiles of both transmitting and silent chips and compare their SNR. Later, we measure the target phase of each receiving element in TDM mode and the transmit phase of the transmitting elements. The results are presented below.

3.5.1 Range measurements

In case of TDM operation, one of the transmitters transmits an FMCW chirp, with a chirp bandwidth of 4.8 GHz and chirp period 4 ms, while the transmitters of the other radar chips remain silent by turning the power amplifier off. The range profiles of the target, a corner reflector with RCS of 1 cm^2 at 60GHz, placed at 25 cm distance from the demonstrator are shown in Fig. 3.6. The top figure shows the range profiles at the receivers due to the transmitting radar chip, in the middle of the array (chip 0 in Fig. 3.4) and the bottom figure shows the range profiles at the silent radar chip at the end of the array (chip 6 in Fig. 3.4). It can be seen that the signal to noise ratio* of the received signal in case of the transmitting radar chip is more than 40 dB. However, for a silent radar chip, it is reduced to approximately 20 dB. This can be explained with the phenomenon of range correlation in FMCW radars according to which the phase-noise correlation between the transmitter and receiver results in a lower noise floor in range profiles for the transmitting chip [68]. Moreover, since the corner reflector for the silent chip is not at broad-side, but at a certain angle, this results in lower antenna gain for the silent chip. Also, since the corner reflector is a highly directive reflector target, the radar cross section towards the silent radar chip is lower than towards the transmitting chip and results in lower signal power. Therefore, for all the silent chips, the receivers have a higher noise floor and lower signal power, this results in a lower SNR and ultimately the error in the phase estimation at the target location will be higher. Note that these range-profile results are obtained after averaging over 1000 chirps.

It is to be noted that the range profiles of all the receivers of all other silent radar

* Note that here the signal to noise ratio (SNR) at the target is defined as the signal power at the beat frequency over the noise floor in the range profiles.

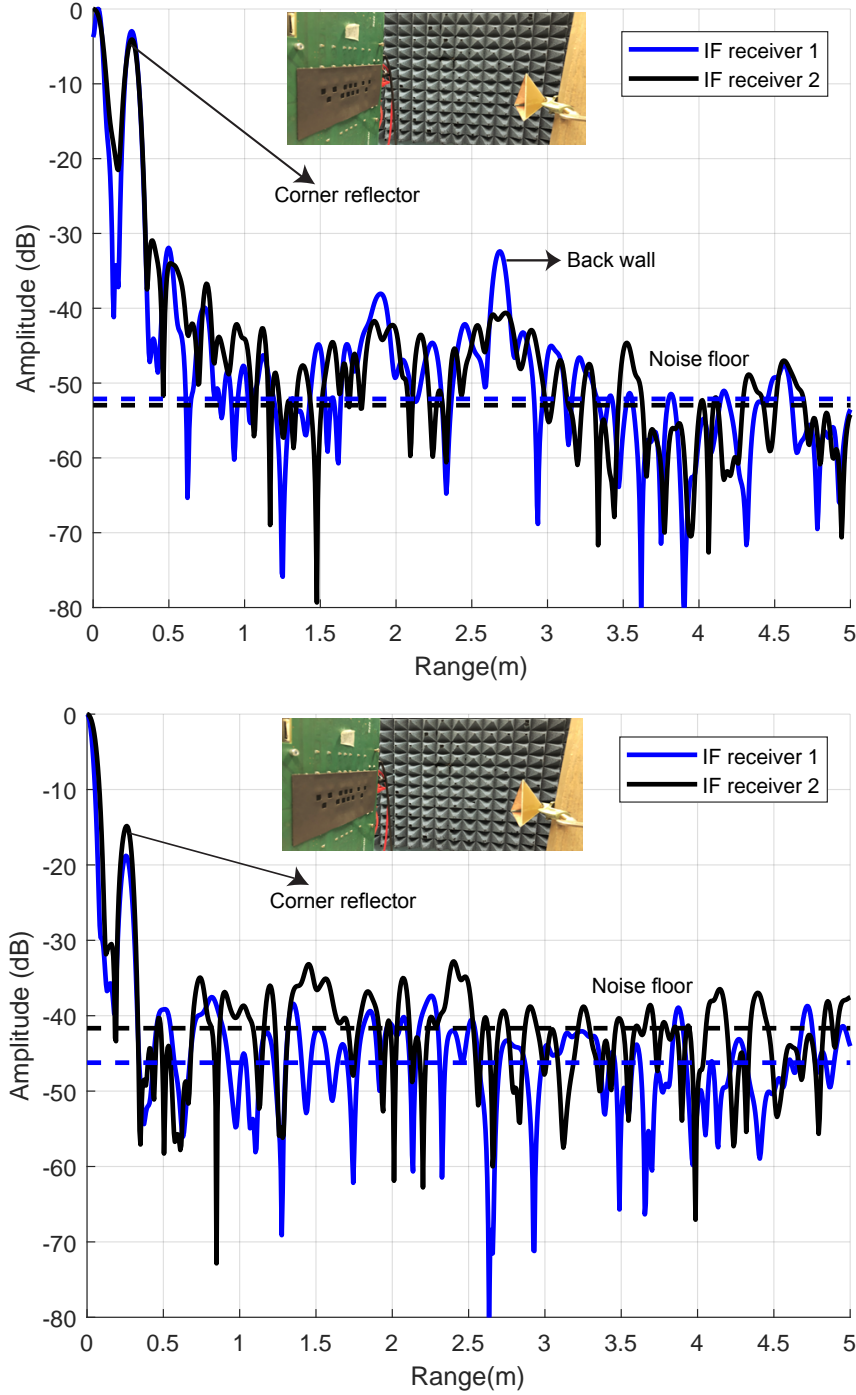


Figure 3.6: Range profile of the target at 0.25m from the receiver of (top) the transmitting chip in the middle of the array and (bottom) the silent chip at the far end of the array. The dashed lines show the noise-floor in each case.

chips also show a SNR at the target lower than 15 dB. This is crucial in our study since the target phase in range profiles is ultimately relevant for the phase compensation of each receiver element for a focused array pattern of the non-regular sparse array in Fig. 3.4. Note that the above results have been achieved by averaging the baseband signal over 1000 transmitted chirps in order to achieve maximum possible SNR.

3.5.2 SNR and target phase error

In order to determine the angular information of the target, the phase at the target is calculated from the range profiles by determining the phase of the FFT index at the range location of the target, for example at 25 cm in Fig 3.6. This target phase at the receivers of each radar chip (transmitting or silent) is then compensated by using the array factor of the radar chips of Fig 3.4, to determine the angle of arrival of the target signal. It is important that the target phase is not affected by the lower SNR in the range profiles. The white-noise in the transmit and receive path influences the accuracy in determining the amplitude and phase of the sinusoidal signal. Since the beat signal in FMCW radars, after filtering, is a sinusoidal signal of the frequency related to the range of the target, and thus additive white-noise determines the phase accuracy of the target signal. The effect of additive white-noise on the amplitude error and phase error of a sinusoidal signal is described in [72] and is briefly explained here.

The received signal in the FMCW radar chips is a baseband sinusoidal signal of frequency ω_0 , and can be modeled as $V = \cos(\omega_0 t) + B_n \cos(\omega_n t + \phi_n)$, where B_n is the amplitude of the noise, ω_n is the frequency of the noise component and ϕ_n is the phase of the noise component. The amplitude of the wanted baseband signal is normalized to 1 and $\omega_0 = \omega_n$ because we are interested in the noise at the range bin where the target is present. Note that the maximum amplitude variations occur when the phase of the noise component ϕ_n is either 0° or 180° , while the maximum phase variations occur when ϕ_n is $\pm 90^\circ$. It follows that the parameter B_n is an essential parameter because the amplitude variations in the received signal are then given by the term $1 \pm B_n$ and phase variations are given by the term $\pm \arctan(B_n)$. Using this model, we can determine the amplitude and phase variations in the received signal based on the value of B_n and consequently the SNR (obtained as $20 \log_{10}(1/B_n)$). Some of the values are shown in Table 3.2. Since, B_n and ϕ have a Gaussian distribution, the rms values of the amplitude and phase of the noise component are provided.

It can be seen that for a SNR below 20 dB, the phase error is considerably high. We showed in Section 3.5.1 that the SNR at the target location is below 15 dB for the silent chips, therefore as per Table 3.2, a large target phase error occurs on the silent chips. This results in the inability to determine the angular direction of the target. It is to be

B_n	SNR (dB)	Amplitude error (dB)	Phase error (deg)
1e-3	60	8.7e-3	5.7e-2
1e-2	40	8.6e-2	5.7e-1
1e-1	20	0.83	5.7
0.5	10	3.5	26
1	0	6.0	45

Table 3.2: Amplitude and phase variations and SNR versus noise amplitude for a sinusoidal received signal, $V = \cos(\omega_0 t) + B_n \cos(\omega_0 t + \phi_n)$. We use rms values of B_n (in the first column), hence SNR is determined from $20 \log_{10}(1/B_n)$, the maximum amplitude variation from $20 \log_{10}(1 + B_n)$ and the maximum phase variations as $+\arctan(B_n)$.

noted that in obtaining Fig. 3.6, the setting of all the components of the radar were set to achieve the maximum output power from each radar. Therefore, in order to solve the issue of this low SNR on the silent chips, it is required to improve the noise figure of the radar chips by improving the receive chain, especially when the transmitters of the radar chips are turned off.

3.5.3 Transmit phase synchronization analysis

In the preceding section, we showed that the phase error at the received signal could be high because of low SNR at the silent chips, which results in high phase errors when using range profiles. Therefore, determining the phase synchronization at baseband among all the chips is not possible. For further evaluation of the demonstrator, we performed over the air measurements with a spectrum analyzer and a standard horn antenna, to determine the phase synchronization of the transmitted signal.

The experimental set-up and results of the radar prototype are presented in Appendix A and the reader is referred to the appendix for further details. The experiments performed with a spectrum analyser resulted in observations in the measurements that could be explained by different potential causes. However, the most probable explanation of these measurement results is that the PLLs of the transmitting chips do not lock the phase properly when fed with the lower reference frequency signal at 24 MHz. This would imply that there is no synchronization between the radar chips when fully configured.

The whole evaluation of this designed prototype allowed to determine some learning points for a future development of the radar platforms intended to be manufactured as an array of individual radar chips with their own PLL at higher frequencies. Firstly, it

has been shown that such a design where the reference signal is at a lower frequency (25 MHz in our case) is possible. However, a steady phase of transmitted signal is a stringent requirement and can be achieved by designing the PLLs of each chip such that they are accurately phase-locked. The reader can refer to [73] for further information and details on the issues of stability of PLL at mm-wave frequencies. Secondly, the noise-floor level of the radar chips (especially for FMCW radars) needs to be improved even for the case when the transmitter is not active in case of TDM-MIMO operation.

In the following section, we show how to determine the effect of phase errors, caused by the above mentioned problems, for MIMO radar arrays, in case of uniform and non-uniform configurations.

3.6 Phase-error tolerances for MIMO virtual arrays

MIMO radar arrays, in addition to better resolution, can also have improved phase-error tolerance as compared to phased-array radars for a certain maximum required side-lobe level. We perform statistical simulations and the results highlight the phase-error tolerance of MIMO virtual arrays for both uniform and non-uniform configurations.

Using FMCW radars in a MIMO array concept is considerably challenging because it is crucial to synchronize the transmit and receive electronics of which a PLL is the main component and has shown to be the cause of phase noise [68]. Thus, to be able to set proper phase-tolerance requirements for these electronics in each radar chip, it is essential to analyze the effect of phase errors in case of MIMO radar systems.

It is well known that the phase errors in the antenna-element excitation of an array result in higher side-lobe levels and consequently false detection in radar target localization [74]. Amplitude and phase errors in the antenna-element excitation of uniform arrays have been studied extensively using statistical models in literature, for example in [74] and [75]. In case of radars, these errors result in false target detection. Here, we determine the effect of phase errors on peak (SLL) in case of virtual-array radiation patterns of MIMO radars by modeling the phase errors in transmit and receive array excitation elements. One case where this analysis is of importance is when the single-chip FMCW radars, as given in [11], are used in a MIMO array configuration with transmit and receive antennas on chip and each with their own RF front end. In such a case, the transmit and receive chains can have independent phase errors and hence they affect the virtual-array radiation patterns. We show that the high phase-error tolerance of virtual arrays can result in lower phase accuracy requirements for transmitter and receiver design in such systems. From [76], the excitation errors in antenna arrays caused by the electronics and positioning errors can be modeled as statistically random errors.

Moreover, we compare the phase-error effect on both a uniform and a non-uniform configuration of the transmit and receive arrays and show that for a certain side-lobe threshold, the non-uniform array configuration is more tolerant to phase errors.

3.6.1 Transmit, receive and virtual array with errors

In MIMO radars, the virtual-array radiation pattern is defined as the product of the transmit and receive array radiation patterns [66]. Considering a transmit linear array of N_t elements with spacing \mathbf{d}_t and a receive array of N_r elements with spacing \mathbf{d}_r , the virtual array pattern is given by

$$V(\theta) = \sum_{t=1}^{N_t} \sum_{r=1}^{N_r} A_t A_r \exp\{-jk_0 \mathbf{d}_t \sin(\theta) - jk_0 \mathbf{d}_r \sin(\theta)\}, \quad (3.1)$$

where k_0 is the free-space wavenumber, and A_t and A_r are the amplitudes of the transmit and receive array patterns, respectively. Since in MIMO radars each transmit and receive array has its own RF front-end chain, the amplitude and phase errors can be modeled as independent random variables. Let δ_{at} and δ_{ar} be the amplitude errors, and ϕ_{pt} and ϕ_{pr} be the phase errors in the transmit and receive array elements, respectively. The distorted virtual-array radiation pattern including the errors in transmit array and receive array is then given by

$$V_d(\theta) = \sum_{t=1}^{N_t} \sum_{r=1}^{N_r} A_t(1 + \delta_{at}) A_r(1 + \delta_{ar}) \exp\{-jk_0 \mathbf{d}_t \sin(\theta) - jk_0 \mathbf{d}_r \sin(\theta)\} e^{j\phi_{pt}} e^{j\phi_{pr}}. \quad (3.2)$$

V_d is now a complex random variable that depends on the random variables δ_{at} , δ_{ar} , ϕ_{pt} and ϕ_{pr} . Here, the focus is on the phase errors of each array element, thus the amplitude errors are assumed to be zero, i.e. $\delta_{at} = \delta_{ar} = 0$. The random variables for phase errors ϕ_{pt} and ϕ_{pr} are modeled as normally distributed with zero mean, which is mathematically represented as $\phi_{pt} \sim N(0, \sigma_p^2)$, $\phi_{pr} \sim N(0, \sigma_p^2)$ where σ_p^2 is the variance of the phase error.

3.6.2 Uniform and non-uniform array configurations

To analyze the effect of phase errors on transmit, receive and ultimately virtual-array radiation pattern, two array configurations are used here; a uniform and a non-uniform. For the uniform array, 4 transmit array elements and 8 receive array elements with a spacing of half a wavelength are considered, which according to the MIMO concept

results in 32 virtual array elements with half-wavelength redundant element spacing. For the non-uniform array, the number of array elements in the transmit and receive array has been kept the same but the element positions are determined by using convex optimization algorithms for the sparsity of the antenna array (see [77] for more details). The design parameters of the two array configurations used in this study are listed in Table 3.3.

Table 3.3: Uniform and non-uniform array configurations

Parameters	Array Configurations	
	Uniform	Non-Uniform
Nt	4	4
\mathbf{dt}	$\lambda_0/2$	$[-0.5\lambda_0 \ 0\lambda_0 \ 0.25\lambda_0 \ 0.75\lambda_0]^*$
Nr	8	8
\mathbf{dr}	$\lambda_0/2$	$[-1.5\lambda_0 \ -1\lambda_0 \ -0.75\lambda_0 \ -0.25\lambda_0 \ 0\lambda_0 \ 0.5\lambda_0 \ 0.75\lambda_0 \ 1.25\lambda_0]^*$
Nv	32	32
SLL transmit**	-11.3 dB	-20.05 dB
SLL receive**	-12.8 dB	-14.08 dB
SLL virtual**	-20.50 dB	-22.51 dB

* Positions of individual elements

** First highest SLL of un-distorted

3.6.3 Resulting effects of phase errors

To determine the effect of phase errors on side-lobe levels of transmit, receive and virtual-array radiation patterns, 10,000 Monte-Carlo simulations have been performed on the two configurations of the transmit and receive array pair. In the simulations, it has been assumed that each array element is subject to independent random errors with the same variance, which have been modeled as independent identically distributed random variables with zero mean and variance σ_p radians.

Peak SLL vs phase error

The variation of the peak side-lobe level due to the presence of phase errors in transmit, receive and virtual array elements in both uniform and non-uniform configurations is presented in Fig. 3.7a and 3.7b. For the uniform array case, it can be seen that although the peak side-lobe level of the virtual array is low because of its definition, the increase

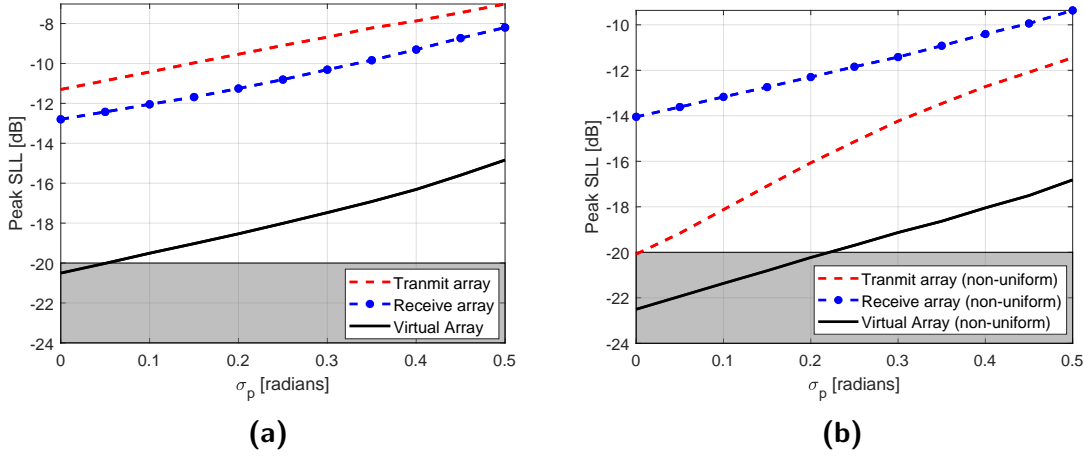


Figure 3.7: Peak SLL variation with respect to variance of the phase error in transmit, receive and virtual array radiation patterns for (a) uniform and (b) non-uniform array configuration.

in the peak side-lobe level due to phase errors follows the same trend as for a transmit and receive array. However, for the non-uniform configuration, the virtual array is more tolerant to the phase errors that cause increased side-lobe level in the transmit array. In conclusion, for a certain required peak side-lobe level (which is -20 dB for many applications), the non-uniform configuration in MIMO radars can be used to relax the strict bounds on phase variation caused by electronics and fabrication errors. The reason is that sparseness in the virtual-array positions caused by the non-uniform transmit and receive array pair distributes the errors randomly.

The error-free and distorted radiation patterns for the transmit, receive and virtual arrays for both uniform and non-uniform configurations are shown in Fig 3.8a and 3.8b for phase errors of $\sigma_p = 0$ and $\sigma_p = 0.5$. Note that because of the phase errors, the main beam also deviates from the desired pointing direction, which can be seen in Fig. 3.8a and 3.8b, but the deviation is not more than 1 degree for a phase error variance of $\sigma_p = 0.5$ radians.

SIMO/MIMO with phase errors

Determining the maximum phase error variance, caused by electronics and element positioning errors, is necessary because an increase in the peak side-lobe level above a certain threshold is crucial since it results in the false detection of targets in radar array systems. In traditional phased-array radar systems, also known as SIMO radars, the peak sidelobe level in the presence of phase errors is higher than in MIMO radars. This effect is shown in Fig. 3.9. For these simulations, it was assumed that parameters like sweep time, bandwidth, power, sampling rate etc. are the same for both the cases.

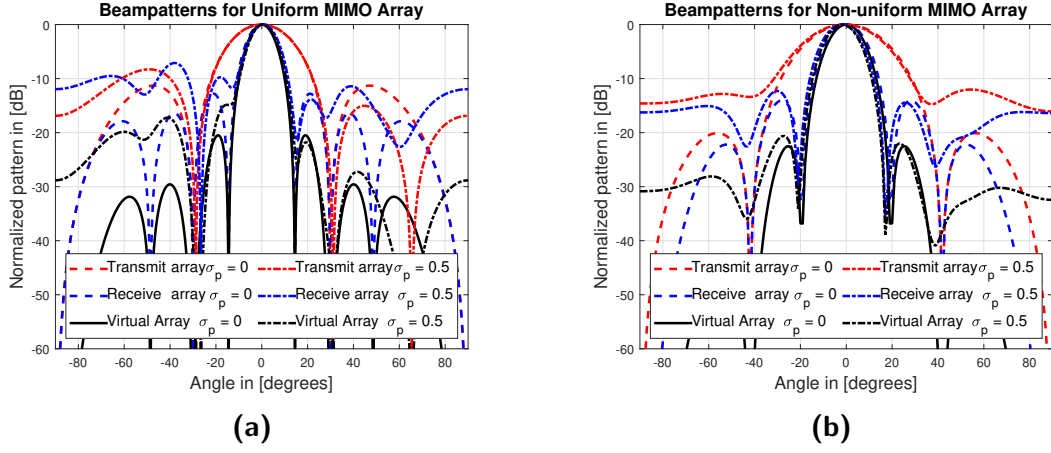


Figure 3.8: Normalized radiation patterns for (a) uniform and (b) non-uniform transmit, receive and virtual array for phase errors, $\sigma_p = 0$ and $\sigma_p = 0.5$ radians.

This demonstrates that MIMO radars can be more tolerant to phase errors, which will ultimately lead to relaxed accuracy requirements for synchronization of transmitters and receivers in MIMO radars.

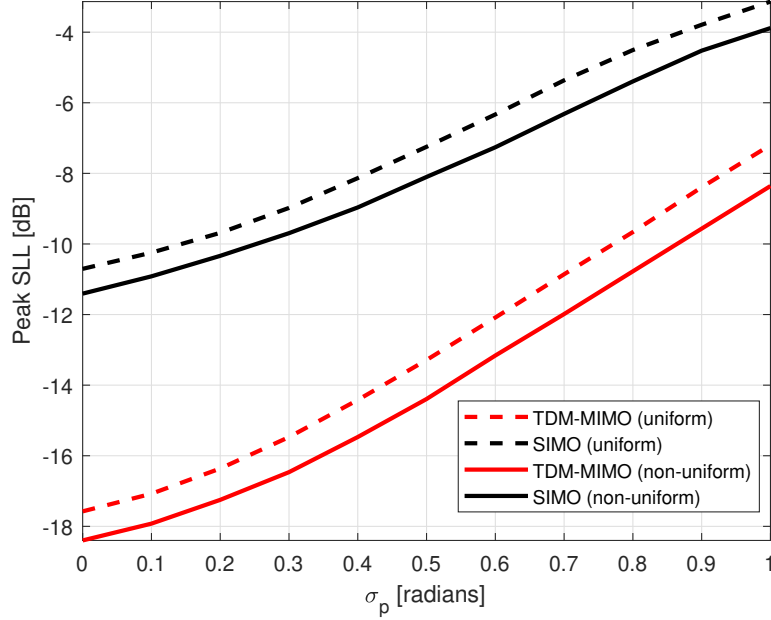


Figure 3.9: Comparison of the effect of phase errors in the transmit and receive chain on the peak side-lobe level between SIMO and TDM-MIMO techniques with both uniform and non-uniform array configurations.

3.7 Conclusion

The design of a complete FMCW-MIMO radar demonstrator has been presented here, which is a multi-node array of FMCW single-chip radars, each with one transmitter and two receivers. The components required for the functionality of a MIMO radar in TDM mode were illustrated and explained. Further, the simulation results for the direction of arrival estimation showed that non-regular sparse MIMO arrays can be used to achieve the resolution of a sparse SIMO array and the dynamic range of a dense array. Furthermore, range measurements in a TDM scenario showed that the SNR of the receivers of the transmitting chip is 20 dB higher than that of the receivers of other (silent) chips in the array. It was shown that the lower SNR results in large phase errors at the target locations, which makes it impossible to determine the direction of arrival. Moreover, it has been shown that there is no phase synchronization between the radar chips when fully configured, which is due to the reason that the PLLs of the radar chips do not phase-lock. Therefore, a steady phase of the transmitted signal is a stringent requirement for such systems to work, see for example in [73].

Moreover, a statistical analysis was performed on the effect of phase errors on the peak SLL of the transmit, receive and virtual-array radiation patterns of MIMO radar arrays caused by radar electronics and positioning errors. It has been shown with simulations that the virtual array for non-uniform transmit and receive pairs show better phase tolerance as compared to uniform arrays.

CHAPTER FOUR

Regular and Irregular-on-Grid Sparse Array Comparison of Connected Aperture Arrays

For SKA mid-frequency aperture arrays, dense connected aperture arrays such as Vivaldi antenna arrays are being considered, but to achieve the required system sensitivity for radio astronomical observations, this would mean that a large number of antenna elements are required, particularly in the order of millions. Two concepts of regular-on-grid and irregular-on-grid sparse array configuration are introduced for these connected arrays to reduce the number of antenna elements and the sensitivity performance of the two concept arrays is compared. Comparing the effective area of these two configurations, it is shown that a regular-on-grid sparse configuration achieves a slightly larger effective area than an equivalent irregular-on-grid sparse configuration. Using the regular-on-grid sparse configuration as case study, the effect the terminating impedance of the inactive antennas has on the receiver noise temperature of a connected array of Vivaldi antennas is investigated.

The content of this chapter is based on [J2] and the work has been performed in collaboration with the Netherlands Institute for Radio Astronomy (ASTRON)

4.1 Introduction

Aperture Arrays (AAs) for the next generation radio telescopes, such as the Square Kilometer Array (SKA), are considered to be the most promising concept for radio astronomical observations [78]. At the mid-frequencies 500 MHz - 1500 MHz, the Mid-Frequency Aperture Array (MFAA) for SKA phase II is still in the research stage especially for the design of antenna array configurations. The sensitivity requirement for these telescopes is more than $10,000\text{m}^2/\text{K}$ [79], which means at these frequencies a dense array configuration would result in 10^7 or more antennas. This is very expensive to realize especially for the case of all-digital aperture arrays. In order to reduce the number of elements, an irregular-sparse array configuration seems a viable solution but the sensitivity drops significantly at higher frequencies [80]. Moreover, since the antennas are randomly placed, the signal processing is more computationally expensive.

Apart from irregular-sparse array configurations, regular-sparse arrays have also been considered for MFAA. The main issue with regular-sparse arrays is the appearance of grating lobes within the field-of-view, but the impact of these grating lobes can be reduced using station rotation, chromatic dispersion or time averaging [81, 82]. The advantage, however, is lower cost due to a smaller number of antennas and less computationally expensive signal processing. However, the impact of these configurations on the performance characteristics of connected antenna tiles, like MFAA Vivaldi antenna tiles for SKA, are not well known.

We use a single dense tile of the connected antenna array and compare the performance characteristics such as effective area, active reflection coefficient and antenna noise temperature in two proposed configurations, i.e regular-on-grid and irregular-on-grid. A number of connected antenna array options have been presented in literature such as connected dipole arrays [83, 84], orthogonal ring antenna arrays [85] and connected slot arrays [86–88]. We choose here the Vivaldi antenna array developed at ASTRON presented in [88], however the proposed analysis can be implemented on aforementioned connected arrays. Note that a finite array tile has been analyzed in order to take edge effects into account for the case of a sparse tile arrangement within a single MFAA station.

4.2 Sparse Configurations

For this study, we use an 8×8 planar array tile of Vivaldi antennas designed at ASTRON for MFAA [88], which is a dual-polarized, triangular grid of connected antennas. The antennas are connected in a W-shaped arrangement for easy manufacturing and

placement of antennas in larger arrays especially when numbered in the millions (a small array is shown in Fig. 4.1c). The tile is a dense array at center frequency, $f_0 = 1$ GHz, therefore the distance d between the array elements is $\lambda_0/2 = 15$ cm, along x and y axis. It is worthwhile to note here that we assume that an array is in the sparse regime whenever $d/\lambda_0 > 1^*$. Therefore, the original tile is dense for the whole frequency range from 500 MHz to 1.5 GHz. The two sparse configurations considered here are regular-on-grid and irregular-on-grid and are shown in Fig. 4.1a and 4.1b, respectively.

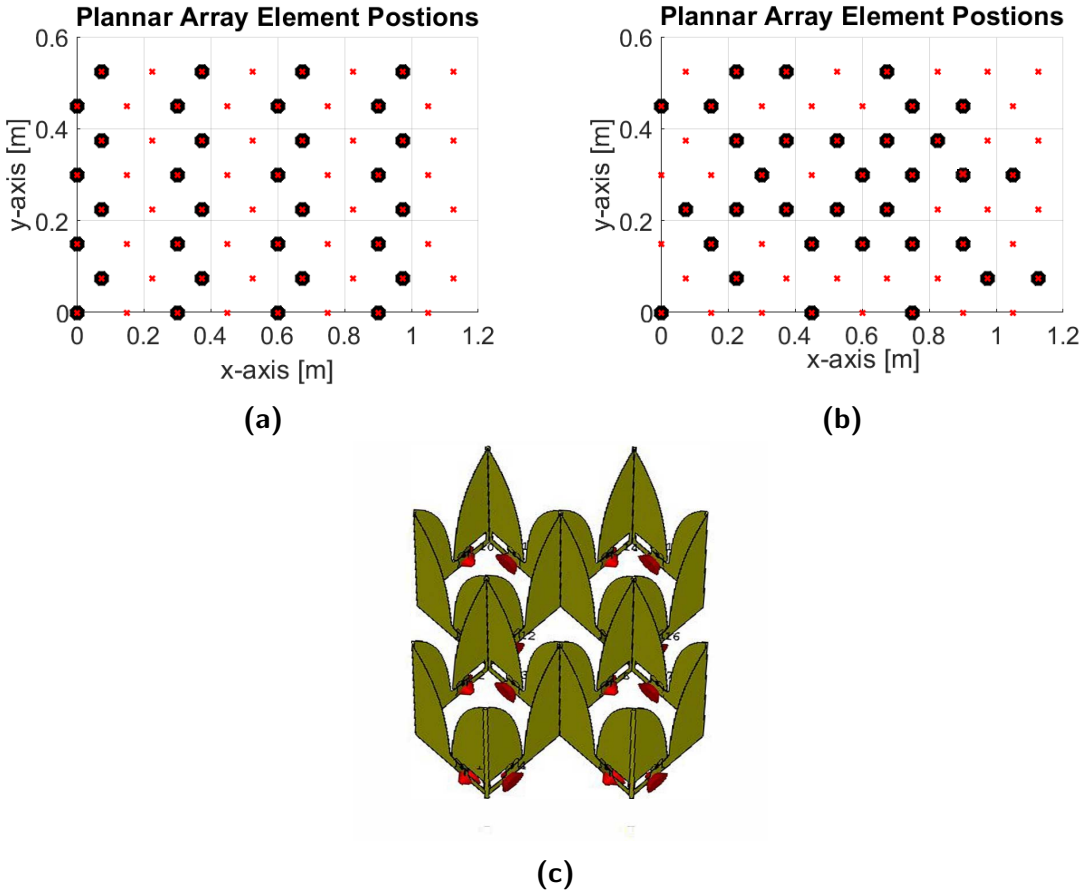


Figure 4.1: Sparse configurations for an 8×8 MFAA planar array tile: (a) Dense vs Sparse Regular-on-grid; (b) Dense vs Sparse Irregular-on-grid. The red crosses are the element positions in a dense tile while the black circles are the active antenna elements in the sparse configuration; (c) W-shaped arrangement of 4×4 Vivaldi antenna array.

*This definition is mainly used in radio astronomy and note that it is different from the one explained in Section 2.4.

The regular-on-grid sparse array is regularly sparse along the x -axis at 1 GHz, and thus the distance between the elements in the x -direction is $\lambda_0 = 30$ cm. This distance makes the array sparse along the x -axis for the frequency range from 1 GHz to 1.5 GHz because $d/\lambda_0 > 1$ for these frequencies. However, it is dense along the y -axis as the original dense tile.

The irregular-on-grid sparse array is randomly sparse but still on the grid of the dense array and the element positions are obtained using the well-known weighted L1-norm convex optimization algorithm for a fixed beamwidth and a maximum side-lobe level of -15 dB. The algorithm optimizes the weights of a dense array to determine the active element positions (see [40] for more detail). Note that in both cases the total number of active elements is almost reduced to half (32 elements for regular and 33 elements for irregular arrangement) but the physical size of the array remains the same. We simulate the complete array with all three array configurations in a full-wave simulation solver, where the inactive antennas on the tile are terminated with 50 Ohm termination. More practical details on the termination of the inactive ports in a physical array are addressed in Section 4.3.2.

4.2.1 Radiation pattern and grating lobes

The simulated radiated far-field patterns of the x -polarized antennas in the $\phi = 0$ plane for two sparse array configurations introduced in Fig. 4.1 are shown in Fig. 4.2. In the case of the regular-on-grid sparse array (Fig. 4.2a), grating lobes appear because of the λ_0 spacing along the x -axis. However, as proposed in [81], the impact of these grating lobes can be controlled by the frequency smoothing effect, or by time averaging. Also, [82] proposes that station rotation can reduce the impact of grating lobes.

However, in the case of the irregular-on-grid sparse array (Fig. 4.2b), no grating lobes appear because of the random placement of the antenna elements on the grid, but the side-lobe levels are dispersed over different frequencies. The comparison of x -polarized patterns of both the configurations scanned to zenith for different frequencies is also shown in Fig. 4.2, and it can be seen that grating lobes appear at higher frequencies for regular-on-grid array while for irregular-on-grid side-lobes remain below -15 dB.

4.2.2 Total effective area

In radio astronomy, an important figure of merit for radio telescopes is the sensitivity of the receiving system which is directly proportional to the effective area of the antenna array. Since the total effective area of an antenna array is directly related to the gain

of the array, by the expression $A_{eff} = \lambda_0^2 G(\theta, \phi) / 4\pi$, the reduction in gain of the array due to fewer active antennas results in a reduction in the total effective area. However, the gain of an array also depends on the distance between the antenna elements. In Fig. 4.3, the total effective area for the two sparse cases (c.f. Fig. 4.1a and 4.1b) with a comparison to the dense arrays (8×8 and 4×8) pointed to the zenith direction is shown.

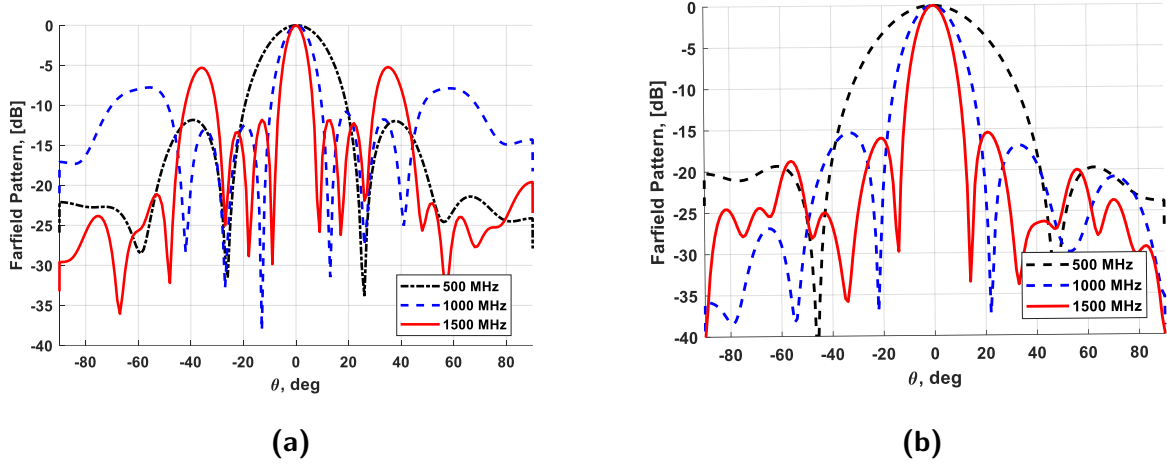


Figure 4.2: Simulated far-field patterns in the $\phi = 0$ plane for (a) Regular-on-grid and (b) Irregular-on-grid sparse arrays for frequencies 500 MHz, 1000 MHz and 1500 MHz.

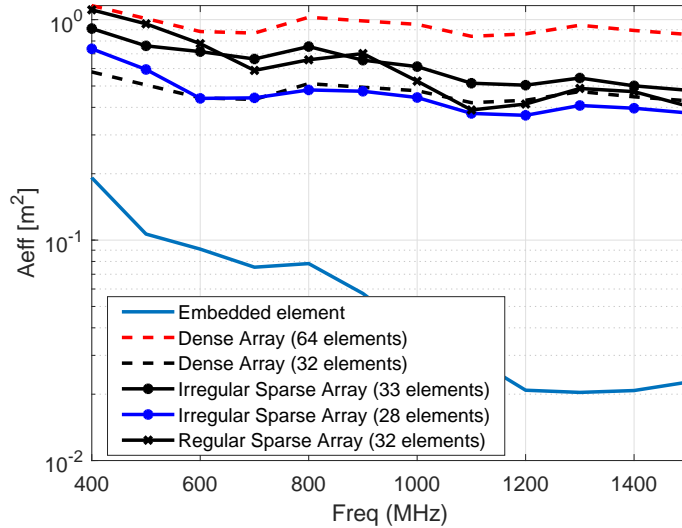


Figure 4.3: Effective area $[m^2]$ versus frequency, for different configurations and number of elements, determined from the gain of the array in the zenith direction.

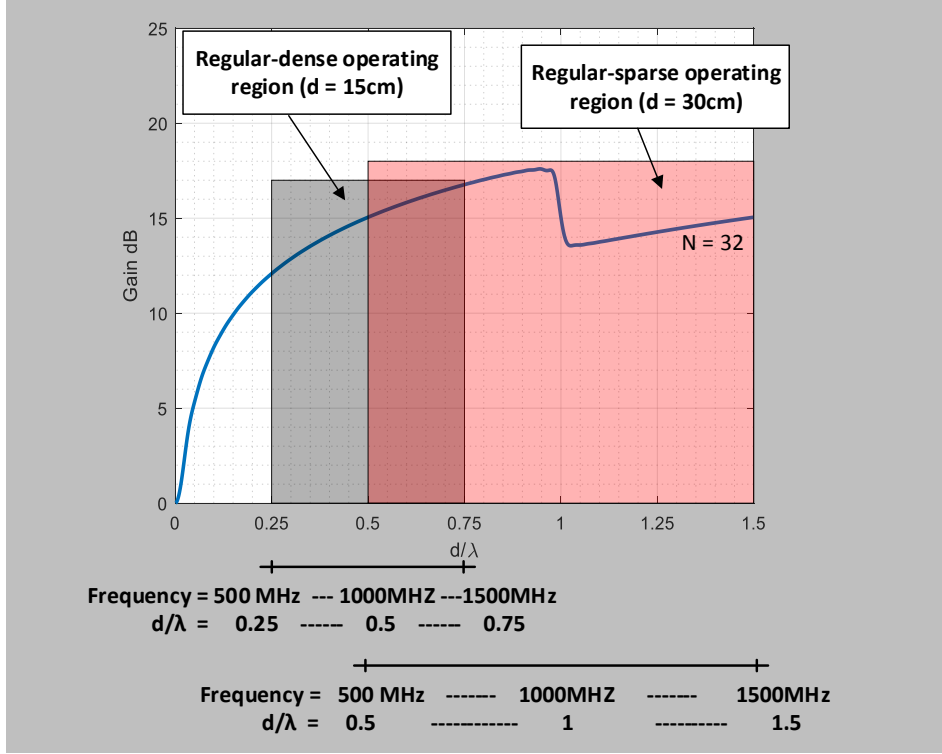


Figure 4.4: Array Gain versus element spacing (d/λ_0) for number of elements $N=32$ and in the zenith direction.

For a regular sparse array, although the array is still dense for the frequencies lower than 1 GHz, the gain is higher than the 32-element regular dense array at these frequencies and hence the A_{eff} is also higher. However, at frequencies greater than 1 GHz the array is sparse and the gain and consequently A_{eff} is the same as the one obtained by the 32-element dense array. The reason for this behavior is explained graphically in Fig. 4.4, which shows the theoretical relation between gain and the element spacing of a regular array for $N = 32$ elements [19]. When the element distance is $d = 15$ cm, the operating region of the regular-dense arrays is $0.25 < d/\lambda_0 < 0.75$ for the frequency range 500 MHz to 1500 MHz. However, for the regular-sparse array with element spacing $d = 30$ cm, the operating region is then $0.5 < d/\lambda_0 < 1.5$. It can be seen that the gain of the array in the region of the regular-sparse array is larger than that of the regular-dense array for frequencies lower than 1 GHz.

For the case of the irregular array, a smaller increase in effective area is achieved as compared to the sparse-regular configuration. Furthermore, A_{eff} reduces consistently when reducing the number of active elements. In Fig. 4.3, this trend is shown by comparison of A_{eff} between the irregular configuration with 33 elements (same as Fig. 4.1b) and a different irregular configuration with 28 elements (not shown in Fig. 4.1).

Therefore, we conclude that with the regular sparse array a better performance in

terms of effective area of the array can be achieved, at lower frequencies. In the rest of the chapter, the regular sparse array configuration is used to determine the performance of the array when the inactive elements in the tile are terminated with either $50\ \Omega$, $\infty\ \Omega$ (open) or $0\ \Omega$ short.

4.3 Element terminations for regular-on-grid sparse array

Since we consider the on-grid sparse options, the inactive antennas can still be connected to the active antennas, but are not connected to the rest of the receiving system, i.e. Low Noise Amplifier (LNA) and beam-former. However, this option raises the question on how to terminate the antennas that are not connected to LNAs and beam-former, but are still physically connected to the active elements, and more importantly, how this termination affects the array performance. In this section, we consider an 8×8 tile of Vivaldi antennas with a regular sparse configuration (Fig. 4.1a) and compare the active reflection coefficient and antenna noise temperature for three different termination options.

4.3.1 Active reflection coefficient

For the active reflection coefficient (ARC), the finite array tile is simulated in CST, first with all elements active, secondly with inactive antennas terminated with $50\ \Omega$, thirdly with inactive antenna ports left open and finally with the inactive antenna port shorted. The comparison of the corner and middle element of the simulated finite array in these four scenarios is shown in Fig. 4.5. It can be seen from Fig. 4.5 that in the case of the corner antenna element, different terminations do not have a significant effect on the active reflection coefficient when compared to the dense array. The small observed effect is due to the fact that the these antenna terminations influence the input impedance of the active elements due to the coupling.

However, in case of the middle element, the array is well matched for the dense case, but for other three cases a larger deviation is observed at lower frequencies, especially around 600 MHz when the ARC is even above 0 dB for open ports. When calculating the active reflection coefficient of a strongly coupled array, it is not uncommon for coupled signals to add constructively with reflected signals at a specific port, ultimately resulting in an $\text{ARC} > 1$. However, when considering the total reflected power from all ports, it is seen that the energy remains conserved within the array.

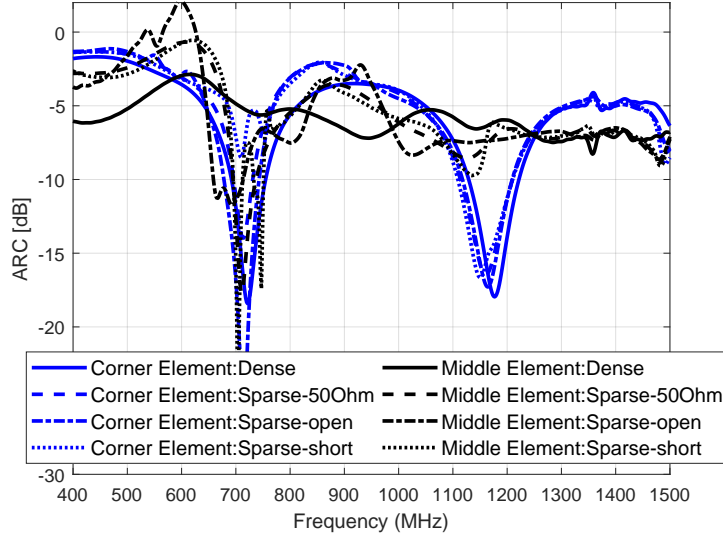


Figure 4.5: Simulated active reflection coefficient of the corner and middle elements of 8×8 Vivaldi antenna array, pointed to the zenith direction, for different terminations.

4.3.2 Antenna array noise temperature

The array noise temperature for an active receiving antenna system is modeled using the S-parameters of the antenna array and LNA, and the noise parameters of the LNA. The beam-former is assumed to be noiseless, meaning that it does not contribute to the noise temperature. This is a valid assumption as long as the electronic gain of the LNA is large enough. Note that each antenna has its own LNA, and are then connected to the beam-forming network, refer to [89] for full system architecture. The mathematical model is described in [90] and [91], and for clarity is briefly explained here. For a passive array, the noise correlation matrix is given by

$$\overline{c_{ACA}^H} = kT_{sky}(\mathbf{I} - \mathbf{S}_A \mathbf{S}_A^H), \quad (4.1)$$

where k is the Boltzmann constant, T_{sky} is the uniform sky noise temperature, \mathbf{I} is the identity matrix and \mathbf{S}_A is the S-parameter matrix of the antenna array. The noise correlation matrix for an active element (LNA in our case) used in the modeling is defined in [89]. The array noise temperature is determined in two steps. In the first step, all the internal noise contributions from the LNA are turned off while the uniform sky noise temperature in Eq. 4.1 is set to 1 Kelvin. The output of the beam-former is then the active antenna array gain, $G_{off} = N_{off}/kT_{sky}$ where N_{off} is the output noise

spectral power density. In the second step, all the noise contributions are included and the uniform sky noise temperature in Eq. 4.1 is set to zero. The output noise spectral power density then is $N_{on} = kT_{out}$, where T_{out} is the output array noise temperature. The array noise temperature referenced to the input is then calculated by $T_{array} = T_{out}/G_{off}$.

In order to determine the effect of different terminations on the antenna noise temperature of a regular sparse tile, in Eq. 4.1 we re-normalize the S-parameter matrix S_A of the passive antenna array to the corresponding new reference impedance of 50Ω , 0Ω for short and $\infty \Omega$ for open, only for the inactive antenna elements in the array, using the expression [89]

$$\mathbf{S}'_A = \mathbf{Y}^{-1}(\mathbf{S}_A - \mathbf{R})(\mathbf{I} - \mathbf{R}\mathbf{S}_A)^{-1}\mathbf{Y}, \quad (4.2)$$

where \mathbf{S}'_A is the re-normalized S-parameter matrix, \mathbf{S}_A is the original matrix, \mathbf{I} is the identity matrix of size N (which is equal to number of antenna elements), and \mathbf{R} and \mathbf{Y} are diagonal matrices whose entries are given by

$$R_n = \frac{Z_{new,n} - Z_{ref,n}}{Z_{new,n} + Z_{ref,n}}, \quad (4.3)$$

$$Y_n = \sqrt{Z_{new,n}/Z_{ref,n}} \cdot \frac{1}{(Z_{new,n} + Z_{ref,n})}, \quad (4.4)$$

respectively. $Z_{new,n}$ is the new reference impedance (either 50Ω , 0Ω for short or $\infty \Omega$ for open) if the n_{th} element is the in-active element otherwise $Z_{new,n} = Z_{ref} = 50\Omega$. For the active elements, the reference impedance remains the same, i.e. 50Ω .

The input referred array noise temperature for the three terminations, at zenith direction and at scan angle $\theta = 45^\circ$ and $\phi = 45^\circ$ are shown in Fig. 4.6 and verified by modeling the system in Agilent ADS [92]. Note that in the above modeling, we used the simulated S-parameters for the antenna array in CST, and the measured S- and noise parameters for the LNA. Furthermore, in-case of sparse array, the beam-former is used only for the active part of the antenna array. It can be seen from Fig. 4.6 that the choice of terminating impedance has a minor influence on the resulting array noise temperature over a large frequency range, particularly above 650 MHz. Also, at

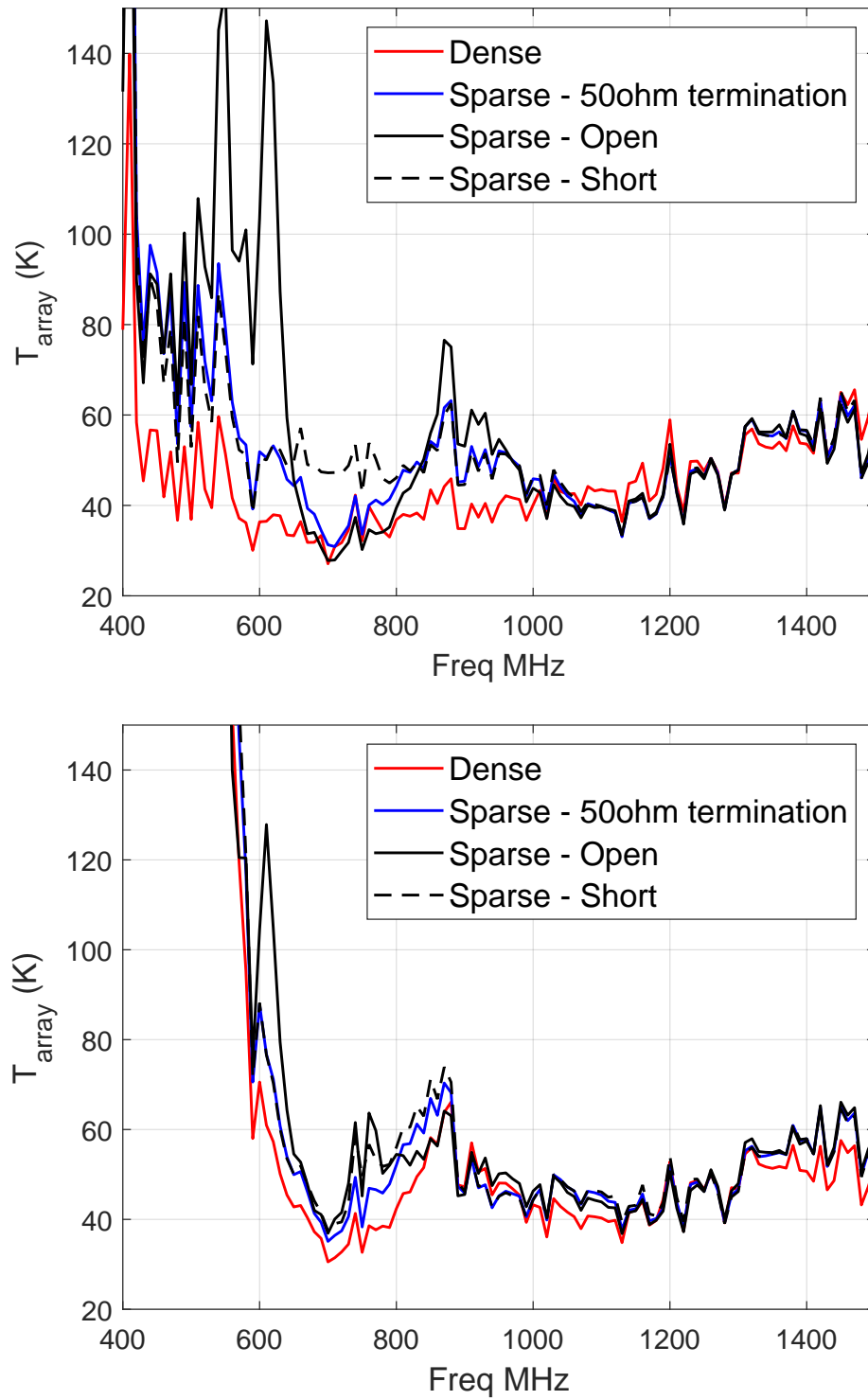


Figure 4.6: Array noise temperature of the 8×8 Vivaldi antenna array for different terminations pointed to the zenith direction (top) and maximum scan angle $\theta = 45^\circ$ and $\phi = 45^\circ$ (bottom).

the maximum scan angle, the original dense array has a high array noise temperature due to high mutual coupling at frequencies below 650 MHz. All other termination scenarios also experience a similar noise penalty. Therefore, it is seen that adopting a sparse-regular configuration in a connected Vivaldi antenna array does not result in a significant noise penalty. From this analysis, it can be concluded that leaving the input port of in-active antennas open would be a suitable practical choice without significantly affecting the system performance. However, using the above stated model, an optimal passive impedance can be determined for an optimal antenna noise temperature for any connected antenna array. This is an interesting research question for the future analysis of sparse arrays based on connected array systems.

4.4 Conclusion

The performance of two sparse configurations, i.e regular-on-grid and irregular-on-grid, for a connected Vivaldi array tile has been compared with the aim to reduce the number of active elements in a tile to achieve the required performance. A comparison of beam-patterns and effective area has been presented for both configurations. It has been shown that the regular sparse array configuration can be used to achieve higher sensitivity at lower frequencies if the impact of grating lobes can be mitigated. Also, actual termination of the in-active antenna elements in case of sparse configurations is addressed and it has been concluded from the results that three termination options, i.e $50\ \Omega$, $0\ \Omega$ for short and $\infty\ \Omega$ for open, do not have a significant effect on the active reflection coefficient and antenna noise temperature for frequencies above 650 MHz. However, using open ports is the most suitable solution when it comes to ease of assembly of these aperture array systems. Also, the model presented in Section 4.3.2, can be used to determine the optimized termination impedance not only for a wide-band performance but also for different scan angles.

In short, to use the MFAAs for an all-sky survey in SKA phase II, the option of digitizing at element level is the most suitable option, but it is not cost effective in case of a dense array arrangement. Therefore, it is essential to look for sparse array configurations, with antenna elements still on grid so that digital signal processing is computationally less expensive by allowing Fast Fourier Transform processing. As this work has shown, both regular-on-grid and irregular-on-grid configurations are a viable option for sparsening of connected aperture arrays.

CHAPTER FIVE

Sparse Virtual Array Synthesis for MIMO Radar Imaging Systems

Multiple-Input-Multiple-Output (MIMO) radar imaging systems require a high angular resolution to realize a high detectability level of the target, which directly relates to the aperture size of the virtual array. Since in MIMO radars, the virtual array topology depends on the transmit and receive array topologies, we propose two novel methods for the synthesis of sparse virtual arrays by designing the sparse transmit and receive arrays using a Two-step Synthesis Procedure (TSP) for antenna array sparsity via convex optimization. Both methods are formulated in detail and it is shown that adjustments in formulations with respect to physical constraints in design specifications are feasible. In the first method, both the sparse transmit and receive array are synthesized using the TSP independently from each other. In the second method, the sparse receive array is synthesized based on the transmit array topology or vice versa, using the method of least squares. With the help of numerical examples, it is shown that a sparse virtual array has a better performance in terms of beamwidth and side lobe level when compared to the traditional dense virtual array, with the same number of transmit and receive array elements. We also show that the proposed design methods lead to a broadband performance.

5.1 Introduction

Radar imaging systems are multi-antenna systems, used for target localization in one or more dimensions providing a high system resolution. These systems cover a wide-range of commercial applications, such as security, medicine, and automotive, which require a high resolution for unambiguous detection of the targets [45, 93–95]. Radar imaging system traditionally use phased-array as multi-antenna systems [96]. The angular resolution of these imaging radars depends on the effective aperture of the phased-array, which means that for a high angular resolution a large aperture, and thus, a large number of array elements for both transmit and receive channels is required to satisfy the Nyquist sampling criterion [97]. Further, in order to avoid the appearance of grating lobes while scanning, a dense array configuration is commonly chosen. This results in expensive phased-array systems especially at mm-wave frequencies, where because of the shorter wavelength, the array element size and inter-element distance are small. To realize high angular resolution with such a solution, a complex antenna system is required [97].

Recently, radar imaging systems largely employ the concept of Multiple-Input-Multiple-Output (MIMO) radar formally introduced by E. Fishler et. al. in [44] and further elaborated in [15, 16, 66, 98, 99]. With the use of multiple transmit and receive channels in MIMO mode, a higher angular resolution can be achieved as compared to traditional phased-array radars [66]. A MIMO radar is different from a phased-array radar in the sense that each transmitter transmits an orthogonal waveform, either in time, frequency, or phase, instead of a coherent signal. Thus, each of the transmitted signals, after reflection from targets, is received by each receiver. This concept results in the formation of a virtual array that is larger in aperture and hence has potentially a higher angular resolution. Like a phased-array, a dense virtual-array configuration in MIMO radar is desirable for scanning without the appearance of grating lobes [19]. However, the MIMO radar concept is increasingly being used for single-chip mm-wave radar sensors either with antenna-on-chip or antenna-in-package; some examples of small-scale radar platforms are a 77 GHz module [54] and a single-chip 79 GHz FMCW radar sensor [12, 100]. To use these sensors in high-resolution imaging applications, the sensors are required to be placed in a cascaded (master/slave) system [101], where a dense configuration is physically not feasible because of size, thermal or cost limitations. In such cases, it is unavoidable to use a sparse virtual array configuration with desirable array patterns and to consider the aforementioned limitations. Also, a sparse configuration results in the reduction of mutual coupling between antenna elements, which is a critical performance indicator when it comes to these radar sensors [102].

In literature, sparse virtual arrays have been proposed and evaluated such as in [9, 103] and in [104] to design a sparse transmit and receive array. The design method

for these arrays is either based on traditional synthesis methods or by trial and error. More recently, a genetic algorithm was used to determine the positions of the transmit and receive array elements, by setting the ambiguity function of the virtual array as the fitness function [105, 106]. The limitation of genetic algorithms is that the fitness function is evaluated repeatedly and, as a result, for a large number of transmit and receive array elements the optimization problem would become highly computationally expensive to solve. Also, in [106] the issue of an unambiguous field-of-view (FoV) while scanning has been addressed, but the maximum achieved side lobe level is around -6 dB for the virtual array pattern, which is considered to be too high for many applications. Overall, a systematic approach is lacking to design sparse transmit and receive array configurations individually to obtain a desired virtual-array performance. The optimization of the transmit and receive array individually allows more design freedom in terms of practical limitations for physical arrays, such as the size of the array and distance between elements, while controlling the side lobe level for each array individually.

We propose two synthesis methods to determine the topology of sparse transmit and receive arrays, which are either synthesized independent of each other or one depends on the topology of the other. For the synthesis of each sparse transmit and receive array, we use the concept of antenna array sparsity, which is known as a technique to reduce the number of array elements while satisfying the array performance requirements [32, 33, 35, 40]. For its simplicity, efficiency, and ease of use, we use the iterative convex optimization procedure. The use of convex optimization for antenna array pattern synthesis was proposed in [32] and was subsequently used in [40, 77], to obtain maximally sparse arrays by using iterative weighted ℓ_1 -norm minimization. This method allows to design a sparse array with the optimal amplitude weights of the antenna array elements which are non-uniform. The non-uniform amplitude weights of array elements is a stringent practical limitation for almost all applications. This problem can be solved by combining this method with a second step of iterative convex optimization, but this time for the antenna array element positions, as proposed in [39]. This leads to a Two-step Synthesis Procedure (TSP) for antenna array sparsity, which is also formulated and explained. Moreover, a sparse antenna array configuration usually results in the appearance of grating lobes in the field-of-view while scanning and we solve this by constructing the antenna array topology using the TSP at the maximum scan angle determined by the system requirements. Using TSP at maximum scan angle for synthesis of transmit and receive array (either independently or jointly) allows to relax the formulation parameters (such as beamwidth and side lobe level) in each arrays synthesis procedure.

Finally, we use this TSP in two methods for the synthesis of a sparse virtual array topology. In the first method, both the sparse transmit and receive arrays are synthesized individually using the TSP and are used to obtain the sparse virtual array

topology. In the second method, the transmit array is synthesized using TSP while the sparse receive array is obtained using the method of least squares [107], to determine the desired virtual array topology. We show with specific test cases that by using a sparse configuration of the virtual array, an improved performance can be achieved as compared to the equivalent dense virtual array, while using the same number of transmit and receive array elements. For the sake of simplicity, both methods are presented for the case of linear arrays. However, both methods can be extended to the planar case for an imaging radar. We are focusing on the optimization of the virtual array performance for MIMO radar systems that ultimately translates into improved signal-to-noise ratio of the obtained information of the target and environment. This will lead to an improved imaging performance of the radar systems.

5.2 Conventional MIMO virtual array concept and its limitations

Consider a linear transmit array of N_t isotropic elements with element position vector \mathbf{d}_t and a receive array of N_r isotropic elements with element position vector \mathbf{d}_r . The array patterns of the transmit and receive arrays are given by following expressions.

$$\mathbf{A}\mathbf{F}_t(\theta) = \sum_{n=1}^{N_t} w_{t,n} e^{-jk_0 d_{t,n} (\sin \theta - \sin \theta_{\text{scan}})}, \quad (5.1)$$

$$\mathbf{A}\mathbf{F}_r(\theta) = \sum_{n=1}^{N_r} w_{r,n} e^{-jk_0 d_{r,n} (\sin \theta - \sin \theta_{\text{scan}})}, \quad (5.2)$$

where $k_0 = 2\pi/\lambda_0$, λ_0 being the free-space wavelength, $w_{t,n}$ and $w_{r,n}$ are the real-valued amplitude weights of the n th array element in the transmit and receive array, respectively, and θ_{scan} is the scan angle. For the sake of simplicity, and without the loss of generality, we assume that both the transmit and receive array have the same array orientation axis. According to the concept of MIMO radar arrays [66], if the transmitted signals from each transmit antenna are orthogonal, then each receive antenna receives N_t different reflected signals from a target. This results in the concept of the virtual array with number of elements N_v whose element positions are all the possible combinations of the transmit and receive antenna positions. Also, the array pattern of the virtual array is the Kronecker product of the array pattern of the transmit and receive array,

and is given by

$$\mathbf{A}\mathbf{F}_v(\theta) = \sum_{n_t=1}^{N_t} \sum_{n_r=1}^{N_r} w_{n_t} w_{n_r} e^{-jk_0 d_{v,n} (\sin \theta - \sin \theta_{scan})}, \quad (5.3)$$

where $d_{v,n}$ is the n th element of the vector \mathbf{d}_v that contains the virtual array element positions, which is given by the equation

$$\mathbf{d}_v = \text{vec}(\mathbf{d}_t \mathbf{J}_{1,N_r}^T + \mathbf{J}_{1,N_t} \mathbf{d}_r^T), \quad (5.4)$$

where $\mathbf{J}_{1,M}$ is a column vector of all ones of dimension M and $\text{vec}(\mathbf{C})$ is the operator for the vectorization of matrix \mathbf{C} . An illustration of the physical transmit and receive arrays and virtual array is shown in Fig. 5.1.

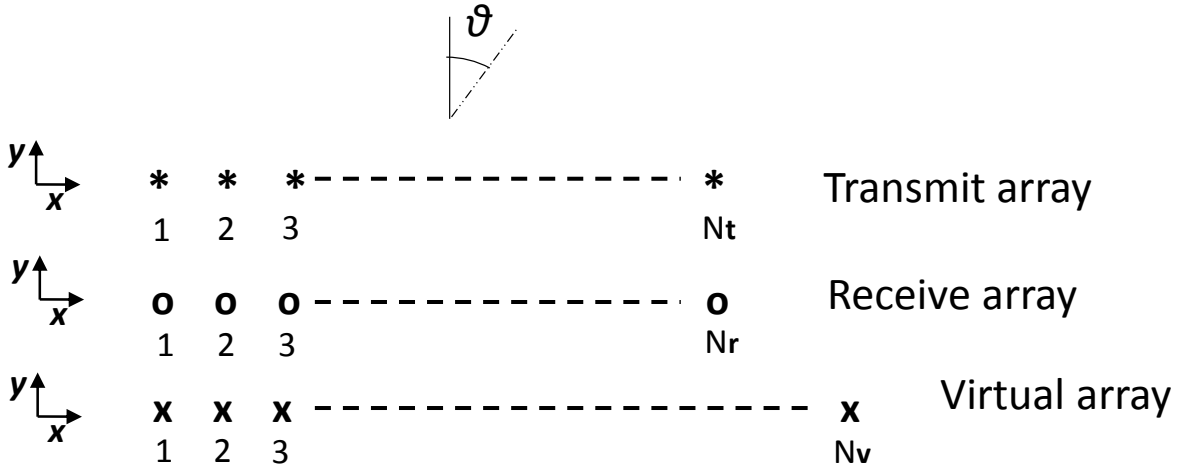


Figure 5.1: Illustration of transmit, receive and virtual array with reference system.

The definition of the MIMO virtual array suggests that its element positions and array pattern depend on the topology of the physical transmit and receive array. The virtual array is so called because it is not a physically real array but an equivalent array whose focused array beam pattern is obtained by receiving the target reflections of each transmitted signal, by each receiver, hence resulting in N_t times N_r reflections of the target which may or may not be unique. In case of linear arrays, the choice of inter-element distance and the mutual orientation of the axes of the arrays for both transmit and receive can allow for different configurations of the virtual array, see [46, 47, 51, 60]. We consider two cases where the transmit and receive array topologies result in a dense

configuration of the virtual array. The first case uses a dense transmit and a dense receive array while the second case uses a regular sparse transmit array and a dense receive array*. Although both cases result in a dense configuration of the virtual array, for a better use of terminology in the rest of the paper, we name the first case “dense virtual array” and second case “conventional virtual array”, since the latter is most commonly used in practical MIMO radar designs, such as in [51, 54].

5.2.1 CASE I: Dense virtual array

When the transmit and receive arrays both use a dense uniform inter-element distance of $d = \lambda_0/2$, the virtual array is also dense with a total number of elements $N_v = N_t N_r$. However, not all of the virtual elements have a unique element position. The number of non-redundant elements is given by $N_v = \lceil (N_t N_r - 1)/2 \rceil$ and therefore the length of the virtual array is given by $L_v = (\lceil (N_t N_r - 1)/2 \rceil - 1)d$. An example in case of a three-element transmit and four-element receive array is shown in Fig. 5.2, with corresponding element positions and array patterns.

5.2.2 CASE II: Conventional virtual array

As discussed in [97], when the receive array is dense with uniform inter-element distance d and the transmit array is regular sparse such that the inter-element distance is $N_r d$, the resulting virtual array will be dense with $N_v = N_t N_r$ elements. All of the virtual elements have unique element positions and therefore the length of the virtual array is given by $L_v = (N_t N_r - 1)d$. An example of a three-element transmit and four-element receive array is shown in Fig. 5.3 with corresponding element positions and array patterns.

5.2.3 Comparison between CASE I and CASE II

Table 5.1 summarizes the comparison of the two cases in terms of the number of elements and the length of the arrays, where L_t and L_r are the physical lengths of the transmit and receive arrays. By comparing the dense and conventional virtual array cases from

*The author uses the following definitions of dense, regular sparse and irregular sparse array in this chapter.

Dense array: when the inter-element distance is regular and less than or equal to $\lambda_0/2$.

Regular sparse array: when inter-element distance is regular and greater than $\lambda_0/2$.

Irregular sparse array: when inter-element distance is irregular and different for all elements.

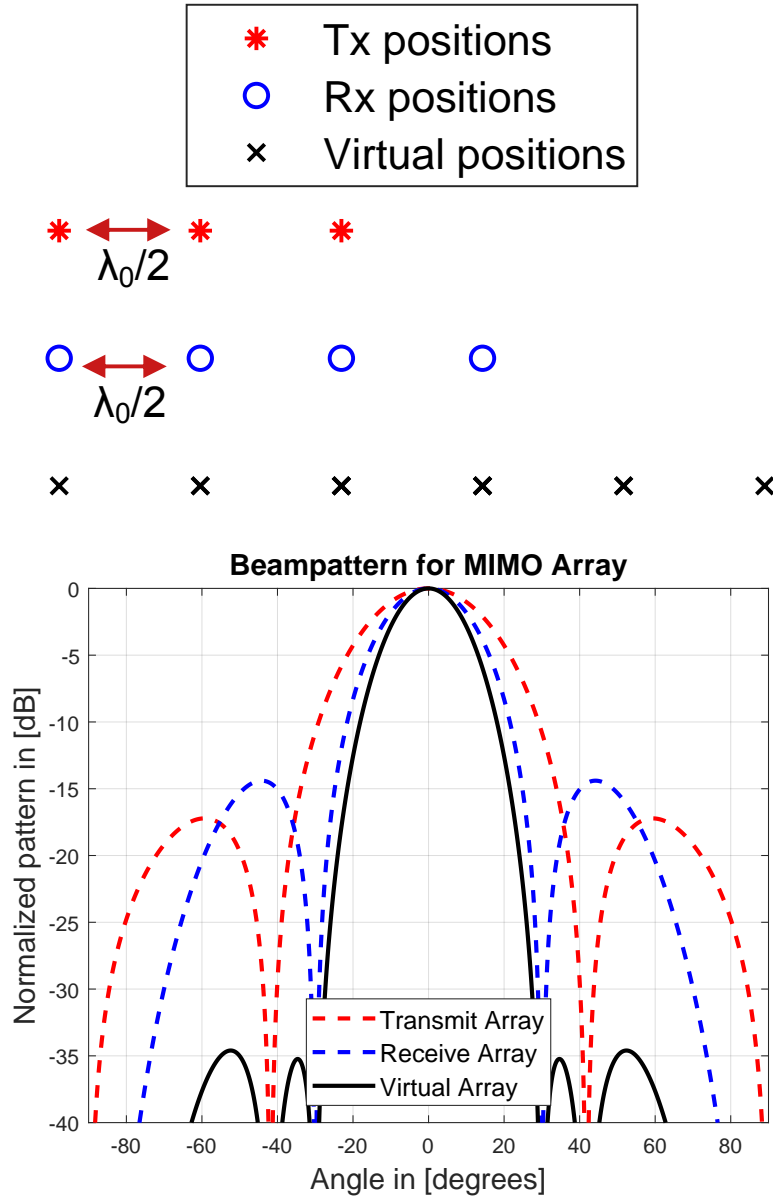


Figure 5.2: CASE I: Dense Virtual Array Configuration example of three-element transmit (Tx) and four-element receive (Rx) array.

Fig. 5.2, 5.3 and Table 5.1, a few important observations can be made. It can be seen that for the same number of transmit and receive elements, the beamwidth of the virtual array in CASE I is considerably wider than that of CASE II. However, the SLL of the virtual array in CASE I is more than 20 dB lower than that in CASE II. This is due to the fact that in CASE I, half of the virtual array element positions are redundant and overlap with the other elements, thus resulting in a virtual amplitude tapering. Thus, the dense virtual array design does not take full advantage of the MIMO concept in terms of beamwidth and the conventional virtual array suffers from a high SLL, which

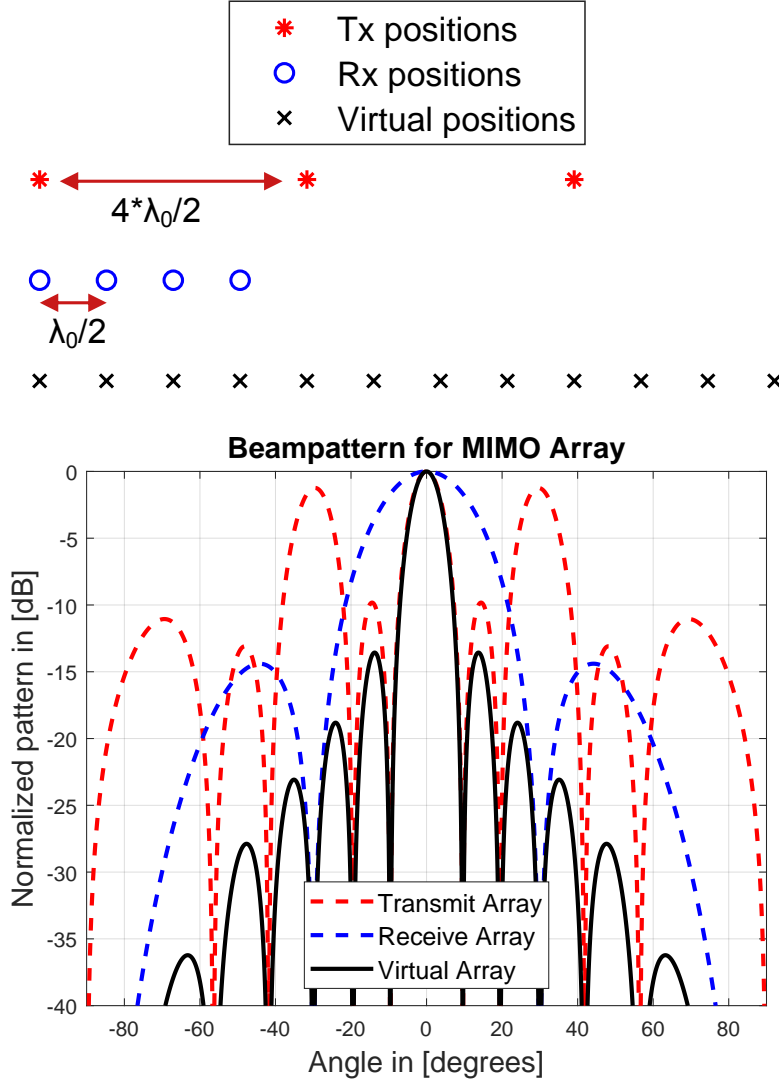


Figure 5.3: CASE II: Conventional Virtual Array Configuration example of three-element transmit (Tx) and four-element receive (Rx) array.

can lead to unwanted target detection. Moreover, in the conventional virtual array design, the physical length of the transmit array is N_r times larger than that of the transmit array in CASE I. Since transmit and receive arrays are the physical arrays in MIMO radars, CASE II leads to a large transmit array, which induces higher costs and more complications in design and realization, e.g. proper mechanical support. CASE II is therefore only practically viable when the number of transmit and receive channels is small, such as in single radar chips in [54, 100], but for a large number of channels, such as for cascaded radar chip designs in e.g. [101] and for antennas-on-chip MIMO radars in e.g. [104], it is not a suitable solution.

Therefore, a third case for the design of virtual arrays is proposed here in which

Table 5.1: CASE I and CASE II comparison

CASE	N_v^*	L_v	L_t	L_r
I	$\lceil \frac{N_t N_r - 1}{2} \rceil * *$	$(\lceil \frac{N_t N_r - 1}{2} \rceil - 1)d$	$(N_t - 1)d$	$(N_r - 1)d$
II	$N_t N_r$	$((N_t N_r) - 1)d$	$(N_t - 1)N_r d$	$(N_r - 1)d$

* Non-redundant

** $\lceil \rceil$ represents the ceiling operation, $N_t < N_r$ and N_r is odd.

both transmit and receive arrays are irregular sparse. This results in an irregular sparse virtual array configuration that can outperform both CASE I and CASE II and the best of both cases can be achieved, i.e narrow beamwidth and low SLL. Since it is well-known that a large sparse array, where the on-average inter-element distance is larger than $\lambda_0/2$, can result in the appearance of grating lobes in the field-of-view while scanning, this problem must be addressed in the design process. In the following section, we present optimization techniques that can be used to determine sparse configurations for both transmit and receive arrays, such that for the virtual array no grating lobes appear while scanning in the FoV.

5.3 Optimization techniques for virtual array synthesis

We propose two techniques for the synthesis of sparse transmit and receive arrays for MIMO radar. The synthesis result for such sparse arrays should provide a better performance of the corresponding sparse virtual array with scanning as compared to the dense and conventional virtual array cases explained in Section 5.2. In the first method, the sparse configurations of the transmit and receive arrays are synthesized independently from each other. In the second method the transmit array is synthesized depending on the obtained receive array configuration from the first method. Both methods use the Two-step Synthesis Procedure using (re-weighted) iterative convex optimization. The TSP will be formulated first, and subsequently each method is described in detail in this section.

5.3.1 Two-step Synthesis Procedure (TSP) formulation

The Two-step Synthesis Procedure for antenna array sparsity via convex optimization with constraints on beamwidth, side lobe level, and minimum element spacing is developed and described here. The goal is to achieve a narrower beamwidth and lower SLL as compared to a dense array. The synthesis procedure follows two steps; the first step is an iterative ℓ_1 -norm minimization via convex optimization for antenna sparsity proposed in [40] and the second step is an iterative algorithm for minimizing the SLL proposed in [39], with a constraint on the minimum element spacing. This TSP is then used to determine the sparse configuration of the transmit and receive array of a MIMO radar with desired beamwidth or SLL. Note that the objective functions and the constraints for the optimization are constructed for one dimension only i.e. along with the direction of the axis of the array (the x -direction in Fig. 5.1). Here, the procedure is illustrated in more detail only for the transmit array. However, a similar procedure can be applied to synthesize the corresponding receive array.

Consider a dense seed array, as a starting point, with the number of elements N large enough to meet the beamwidth specification. A dense array implies a spacing of $\lambda_0/2$ or less, where λ_0 is the free-space wavelength at the maximum frequency of operation. This spacing ensures the absence of grating lobes within the FOV even when scanning [20]. The first step is a re-weighted ℓ_1 -norm minimization solved via convex optimization for antenna array sparsity and returns N_t elements with optimal weights and a side lobe level below a pre-set threshold, i.e. SLL_{\min} . Since the use of non-uniform weights for the transmit array elements is undesirable in most applications, the optimal weights of the N_t elements are reset to one. This results in an increase in the SLL of the sparse array that is then used as an input to the second step to further reduce the SLL by repositioning the array elements. The first step is illustrated below:

$$\begin{aligned}
 \text{STEP I : } & \min_{\mathbf{w}_i} \|\mathbf{Z}_i \mathbf{w}_i\|_{\ell_1} \\
 & \text{subject to} \\
 & \text{AF}(\theta_{\text{scan}}) = 1 \\
 & \text{AF}(\theta_s) \leq \text{SLL}_{\min}, \theta_s \notin [\theta_{\text{scan}} \pm \theta_{\text{FN}}]
 \end{aligned} \tag{5.5}$$

where $\mathbf{Z}_i = 1/|\mathbf{w}_{i-1}| + e$ is a diagonal matrix updated on the i -th iteration, e is a small positive number and determines the efficiency of the algorithm, and \mathbf{w}_i is the vector that contains the amplitude weights of the N array elements (see (5.1)). Further, θ_s

represents the side lobe region, and θ_{FN} is the angle corresponding to the first null in the radiation pattern. In practice, θ_s is represented by a set of discrete samples with a spacing of 1° . After each iteration, the solution vector \mathbf{w}_i contains varying amplitudes and only the non-negligible weight amplitudes can be selected, thus resulting in a sparse transmit array of size N_t and element positions collected in the vector \mathbf{d}_t . The number of iterations for this step is usually very small, see [40].

In the second step this sparse array is used and the non-uniform weights of all N_t elements are set equal to one. The goal is now to adjust the antenna positions with small displacements \mathbf{d}' , using a second iterative procedure, while maintaining a minimum distance d_{\min} between the elements of the array. This procedure uses a first-order Taylor-series approximation of the antenna array factor to linearize it with respect to the antenna position displacements \mathbf{d}' , see [39] for more details. The second step is illustrated below:

$$\text{STEP II : } \min_{\mathbf{d}'} \max_{\theta_s} (|\text{AF}_t(\theta_s)(1 + jk\mathbf{d}' \sin \theta_s)|)$$

subject to

$$\text{AF}_t(\theta_{\text{scan}}) = 1 \tag{5.6}$$

$$\mathbf{d}' = \epsilon, \quad \epsilon \ll \lambda_0/(2\pi)$$

$$|d_{t,n+1} + d'_{n+1}| - |d_{t,n} + d'_n| \geq d_{\min}$$

where $n = 1, \dots, N_t - 1$. \mathbf{d}' and \mathbf{d}_t are both vectors of size N_t . \mathbf{d}' must be smaller than $\lambda_0/2\pi$ for the first-order Taylor series approximation to hold [39]. Note that the value of d_{\min} is a design choice and depends on the size of the physical antenna element. For an example of the performance of the TSP used to synthesize a broadside array, the reader is referred to Section II of [108].

5.3.2 Method I: TSP with maximum scanning

The outcome of the TSP is a sparse array with N_t elements and positions \mathbf{d}_t and its beamwidth equivalent to that of a larger array of N elements. This procedure can synthesize a sparse array for an arbitrary scan angle. It is a well-known fact that if the sparsity of the array is large, i.e. the average array element distance is larger than $\lambda_0/2$, grating lobes appear in the FoV when scanning away from broadside [19]. Therefore,

to overcome this problem, we propose here that in (5.5) and (5.6) by choosing scan angle $\theta_{\text{scan}} = \pm\theta_{\text{max}}$, where θ_{max} is the maximum scan angle in the FoV, the grating lobes do not appear in the FoV while scanning. However, it should be noted that the sparsity achieved for a specific scan range is usually lower than what can be achieved at broadside.

Furthermore, the above stated TSP can also be used to determine the sparse receive array for a particular maximum scan angle with N_r elements. Thus, in this Method I, the sparse transmit and receive arrays are designed individually using the TSP at the maximum required scan angle of the MIMO radar and the virtual array positions can be obtained from (5.4). Since the virtual array pattern is the product of the transmit and receive array pattern, while designing the sparse transmit and receive arrays, a compromise between the SLL of one array (say the transmit array) and the beamwidth of the other array (say the receive array) can be made in order to achieve the maximum possible performance of the virtual array. A flow chart for Method I is illustrated in Fig. 5.4. A numerical example to show the performance of this method and to validate these claims is presented in Section 5.4.1 and the performance is compared with an equivalent dense virtual array.

5.3.3 Method II: Virtual array synthesis using the methods of least squares

In Section 5.3.2, the TSP has been used to determine the sparse array configurations of both transmit and receive arrays of a MIMO radar individually, which means that the element positions of each array are independently selected from each other. However, (5.4) suggests that the element positions of the receive array can be determined from the element positions of the transmit array or vice versa. Therefore, we propose here a second method to determine the virtual array positions using the method of least squares (MLS), where the transmit and receive array element positions are determined from each other. In this method, first a sparse transmit array configuration is determined using the TSP at the maximum scan angle, as explained in Section 5.3.2. These transmit array element positions are then used to determine the receive array element positions using (5.4) and via convex optimization of a least squares formulation to minimize the difference between the realized and desired virtual array element positions, which is formulated as follows.

Let \mathbf{d}'_v be a vector that contains the element positions of a desired virtual array. The values of \mathbf{d}'_v can be user defined, determined from (5.4), and based on the required performance of the MIMO radar system and the practical limitation of transmit and receive arrays such as maximum length and minimum possible distance between

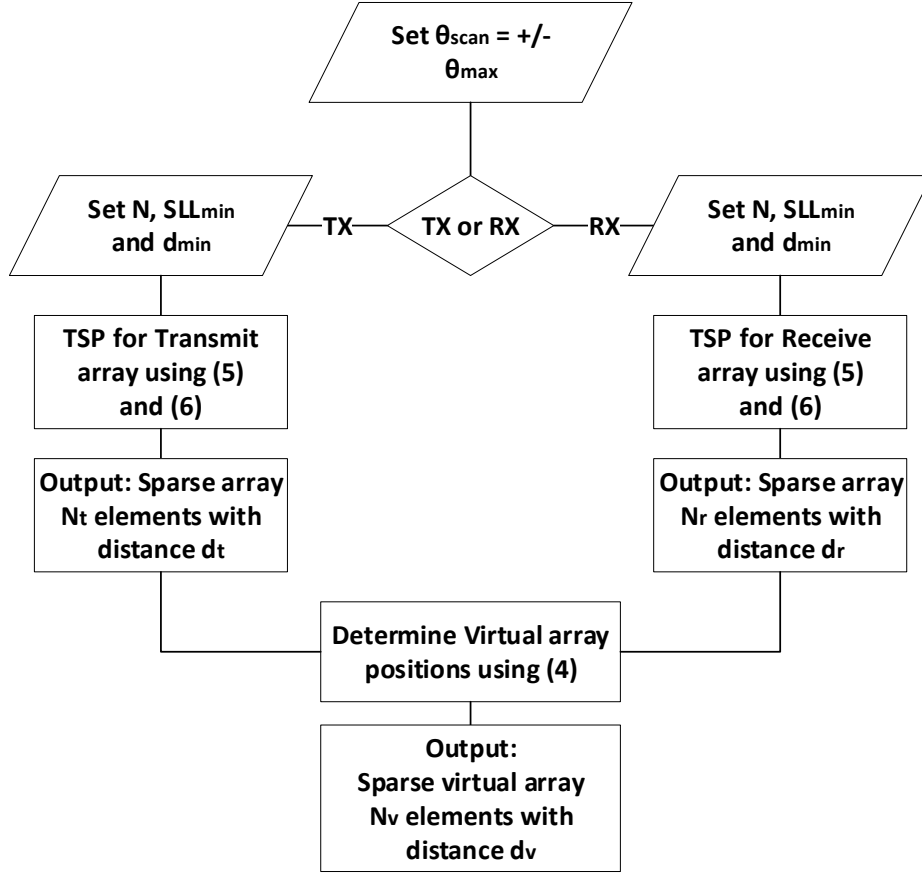


Figure 5.4: Flow chart for Method I.

elements. Also, let \mathbf{d}_v contain the realized virtual array element positions, depending on the transmit array element positions \mathbf{d}_t from the TSP and the receive array element positions \mathbf{d}_r , which are the optimization variables. The objective of this optimization is to minimize the ℓ_2 -norm of the difference between the realized \mathbf{d}_v and desired \mathbf{d}'_v virtual array positions, with \mathbf{d}_r being the vector consisting of optimization variables with length N_r . Constraints can be placed on \mathbf{d}_r , such as the required size of the array and minimum distance between the elements. The optimization procedure along with the constraints is illustrated as follows:

$$\begin{aligned}
& \min_{\mathbf{d}_r} \quad \|\mathbf{d}_v - \mathbf{d}'_v\|_{\ell_2} \\
& \text{subject to} \\
& \text{AF}_v(\theta_{\text{scan}}) = 1 \\
& \max(\mathbf{d}_r) \leq L \\
& \min(\mathbf{d}_r) \geq -L \\
& \min(d_r(n+1) - d_r(n)) \geq d_{\min}
\end{aligned} \tag{5.7}$$

where $n = 1, \dots, N_r$ and $L = L_r/2$ is the required length of the receive array, which depends on the physical limitation of the MIMO system.

The vector \mathbf{d}'_v is user defined and to determine how to select the values for this vector \mathbf{d}'_v , the relationship between the distance vector \mathbf{d}_v , the length L_v and the number N_v of the virtual array is illustrated in Fig. 5.5. The solid line shows that, for a conventional array design (CASE II), there is a unique virtual element position for each virtual array element, which results in a large array aperture and consequently in narrow beamwidth. However, in the dense array design (CASE I), almost half of the array elements have redundant element positions, as shown by the dashed line, thus resulting in a smaller aperture and wider beamwidth, as compared to the conventional array design. Although the conventional array design seems like the optimal option for narrow beamwidth, for a large number of transmit and receive array elements it might not be a practically viable solution, as explained in Section 5.2. Therefore, an array designer can choose any set of desired virtual array positions \mathbf{d}'_v that lies in between the dashed and solid lines of CASE I and CASE II in Fig. 5.5.

A flow chart for Method II is illustrated in Fig. 5.6. A numerical example to illustrate the performance of our proposed method is presented in Section 5.4.2.

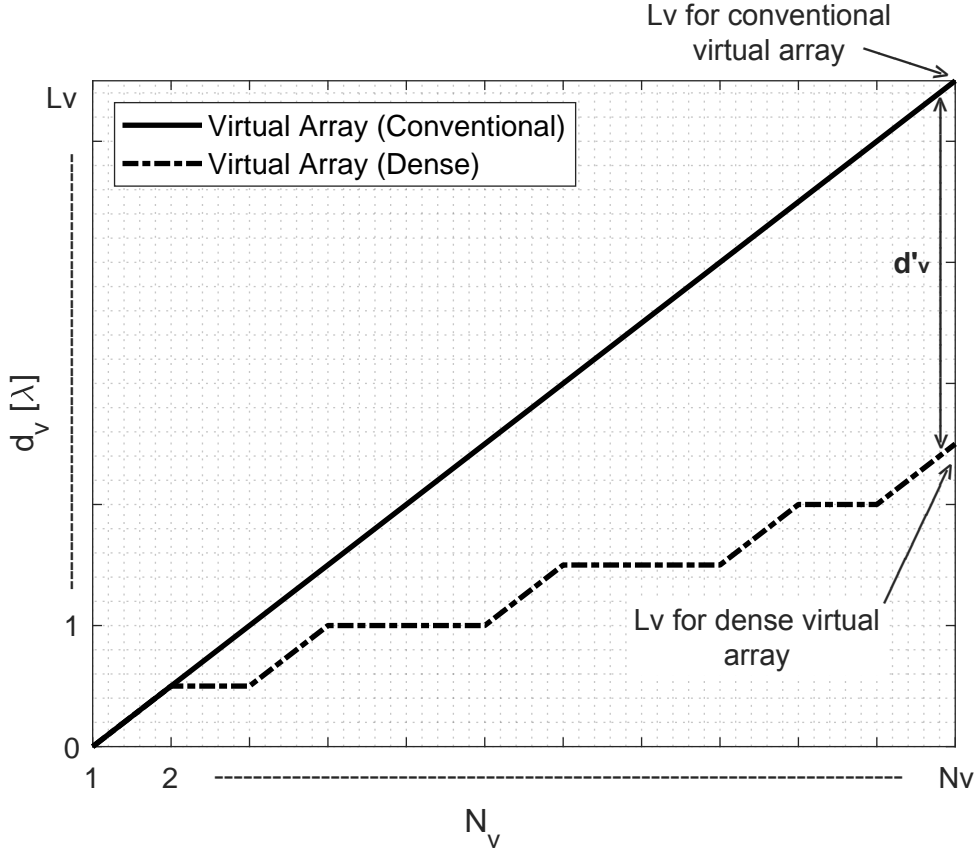


Figure 5.5: The relationship between the distance vector \mathbf{d}_v , the length L_v and the number N_v of the virtual array for both conventional (solid line) and dense (dashed line) virtual array design.

5.4 Numerical examples

Now, we investigate several numerical examples to demonstrate the performance of the methods explained in Section 5.3 and discuss these results in detail. Also, for each example, a comparison is made with the corresponding dense array to highlight the improvement that can be achieved with sparse configurations. Each antenna element is assumed to have a cosine element pattern and only far-field radiation patterns are calculated. Furthermore, to solve the optimization routines in both methods, CVX in Matlab has been used, which is a package to specify and solve convex problems [109, 110].

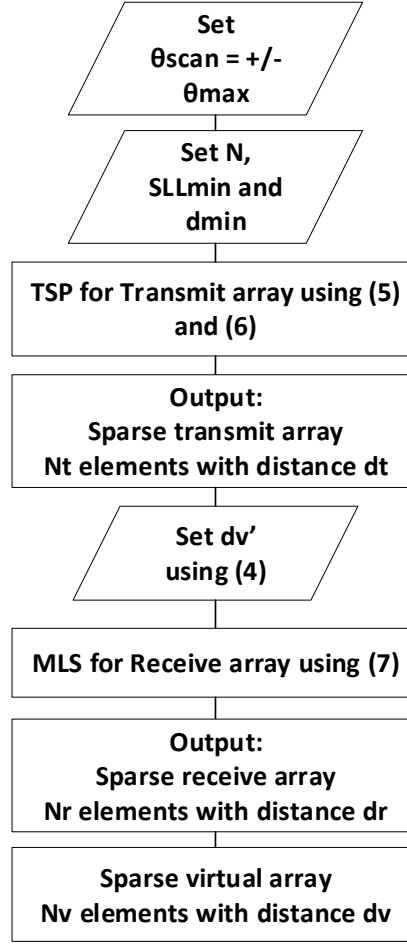


Figure 5.6: Flow chart for Method II.

5.4.1 Method I: TSP with maximum scanning

In order to evaluate the performance of the method formulated in Section 5.3.2, we start with a linear seed array of $N = 40$ elements with element spacing of $0.5\lambda_0$. In (5.5), the SLL_{\min} is set to be -20 dB and in (5.6), the minimum element distance d_{\min} is set to be $0.45\lambda_0$. These two steps are executed separately for two scan angles, first at broadside, i.e. $\theta_{\text{scan}} = 0^\circ$, and at the maximum scan angle $\theta_{\text{scan}} = 40^\circ$. The element positions that come out of the TSP for these two scan angles are shown in Fig. 5.7 and the corresponding normalized radiation patterns for each configuration are shown in Fig. 5.9.

It can be seen from Fig. 5.7 that for each scan angle the outcome of the TSP is different, both in terms of the number of elements and in terms of the element positions. For the broadside direction, the number of elements is reduced to half of that of the

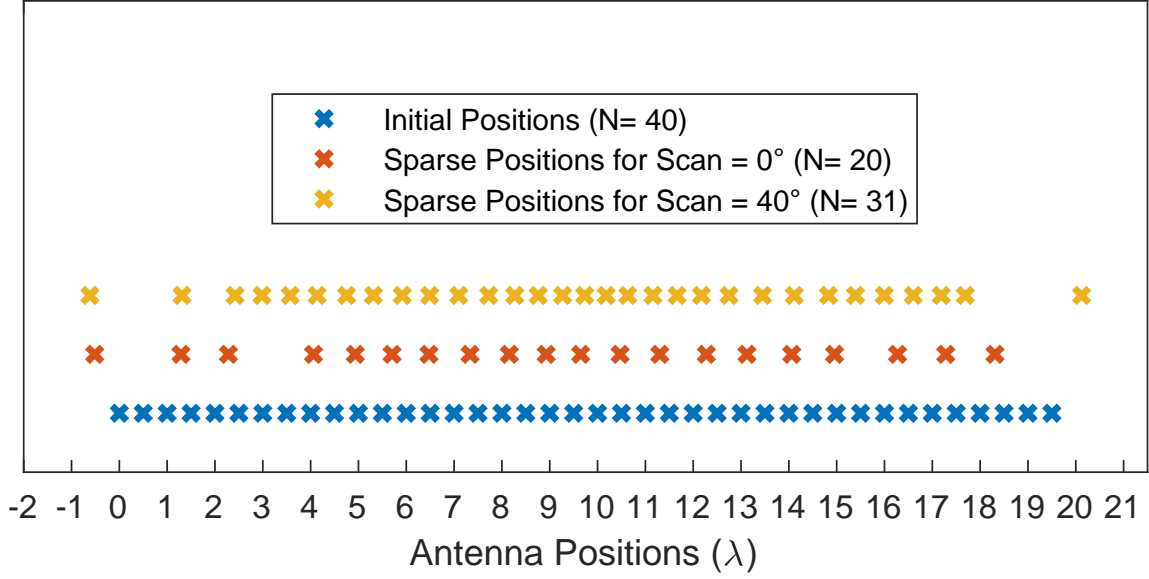


Figure 5.7: Optimized receive positions for $\theta_{\text{scan}} = 0^\circ$ and for $\theta_{\text{scan}} = 40^\circ$ with $SLL_{\text{min}} = -20$ dB obtained via Method I.

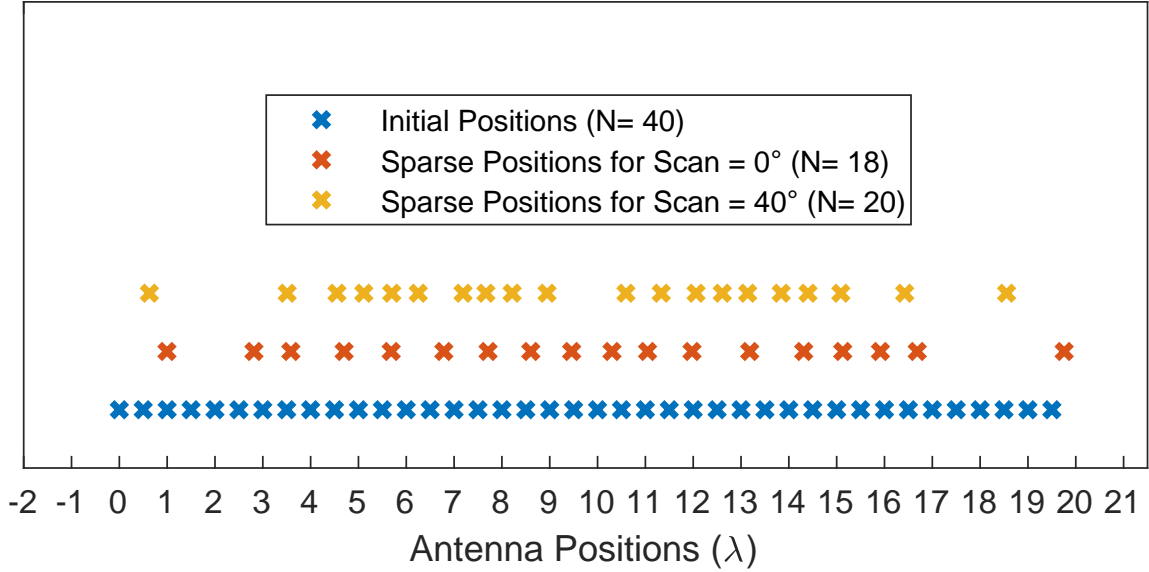


Figure 5.8: Optimized transmit positions for $\theta_{\text{scan}} = 0^\circ$ and for $\theta_{\text{scan}} = 40^\circ$ with $SLL_{\text{min}} = -15$ dB, obtained via Method I.

original array, and the array element positions are sparse, see the red crosses in Fig. 5.7. Moreover, the scanning behavior of this sparse configuration is shown in Fig. 5.9 (top), which indicates that scanning up to the maximum scan angle results in the appearance of grating lobes in the FoV. However, by determining the sparse configuration using the TSP at maximum scan angle, as proposed in Section 5.3, this issue can be resolved.

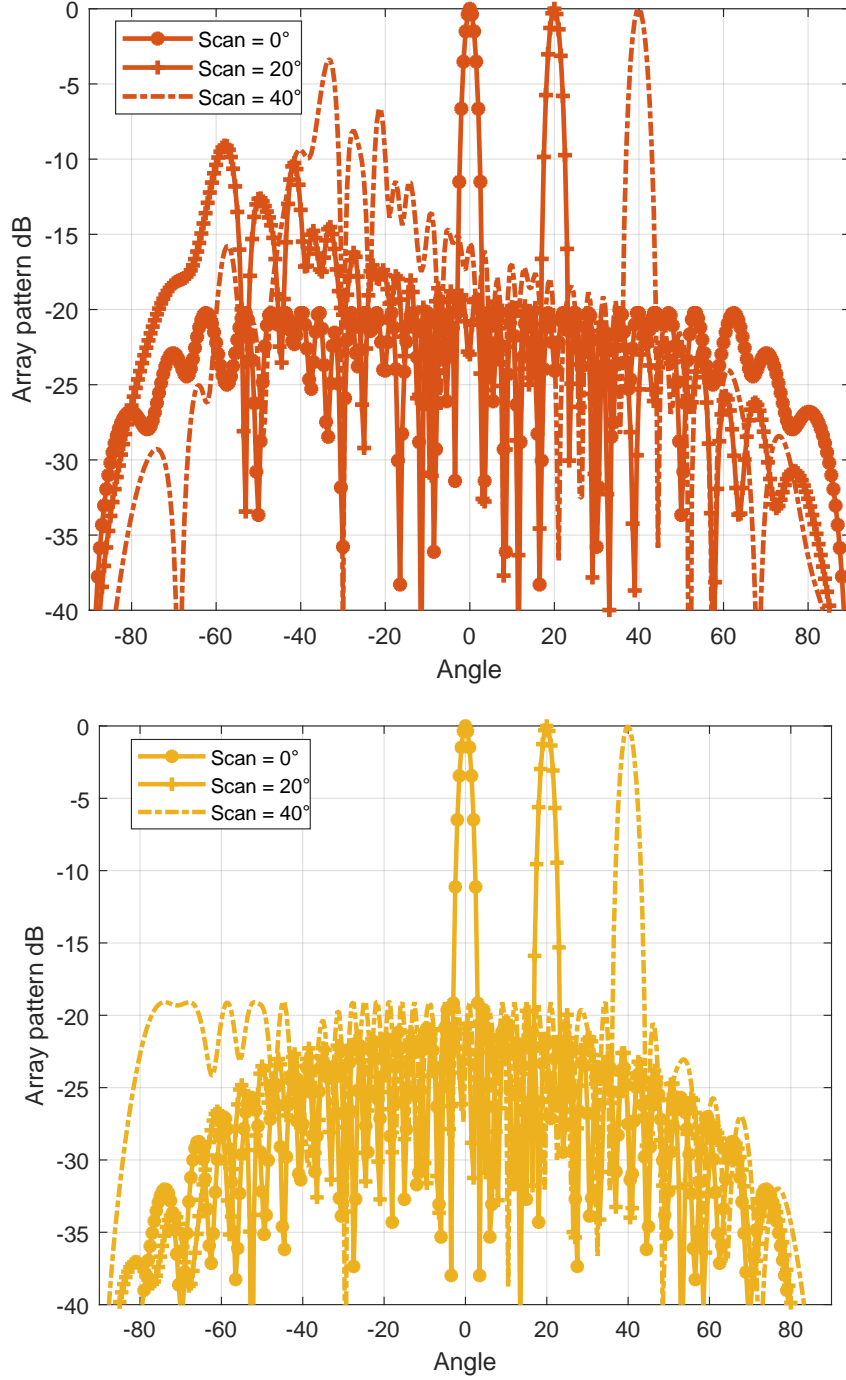


Figure 5.9: Array patterns at three different scan angles for two configurations of Fig. 5.7 for $\theta_{\text{scan}} = 0^\circ$ (top) corresponding to red crosses and for $\theta_{\text{scan}} = 40^\circ$ (bottom) corresponding to yellow crosses.

For a maximum scan angle of 40° , the number of elements is reduced by one-fourth of the original array, see the yellow crosses in Fig. 5.7. The scanning behavior of this configuration, in Fig. 5.9 (bottom), shows that no grating lobes appear in the entire

FoV while scanning. Note that this array configuration is asymmetric but since the difference is small, no grating lobes will appear in the radiation pattern at scan angle -40° . This configuration can be used either for the transmit or receive array, but for the purpose of illustration we will use this configuration as the receive array with $N_r = 31$ for a MIMO radar array design.

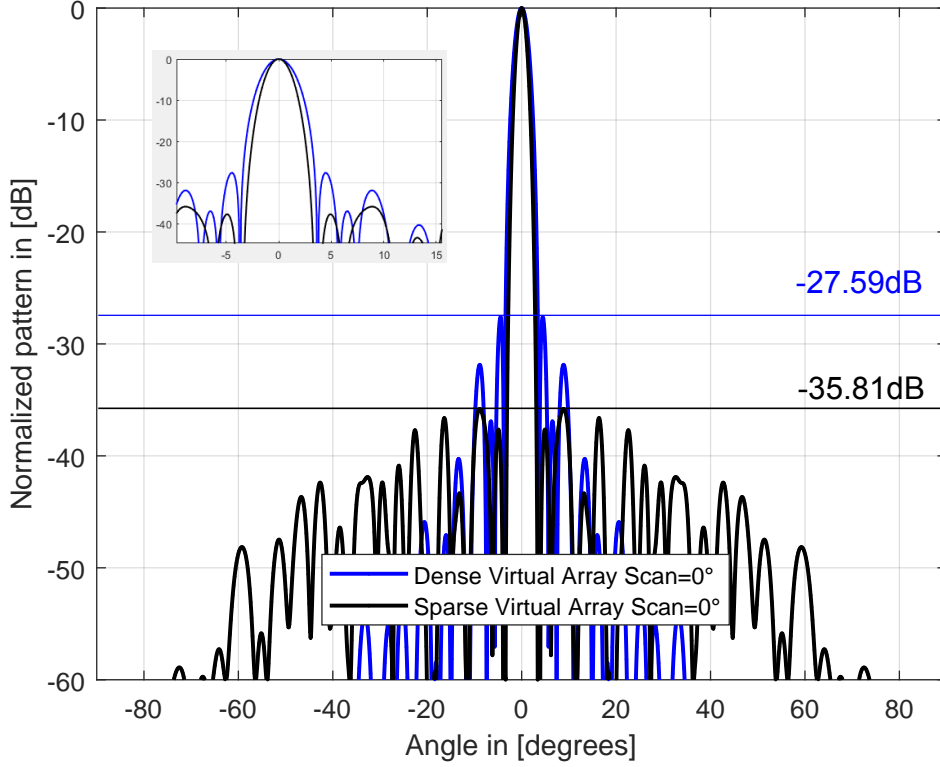


Figure 5.10: MIMO virtual array patterns for $\theta_{\text{scan}} = 0^\circ$ for the sparse configuration and for the equivalent dense array, obtained via Method I. Inset: close-up of the main beam at broadside, showing an improvement in beamwidth.

Now, for the transmit array of a MIMO radar, we use the same procedure to obtain a sparse configuration from the TSP at $\theta_{\text{scan}} = 40^\circ$, with $SLL_{\text{min}} = -15$ dB and $d_{\text{min}} = 0.45\lambda_0$, which results in $N_t = 20$ for the element positions shown in Fig. 5.8. Subsequently, we determine the virtual array element positions using (5.4). The virtual array thus has $20 \times 31 = 620$ elements with irregular positions and the corresponding virtual array radiation pattern is shown in Fig. 5.10 for broadside. For comparison, the radiation pattern of the equivalent dense virtual array, with transmit and receive array elements with half-wavelength spacing and uniform amplitude, is also shown. The sparse configuration exhibits approximately a 1.2° improvement in beamwidth (i.e. 20%) and a 7 dB improvement in SLL, as compared to the equivalent dense array (array with the same number of elements but with half-wavelength spacing).

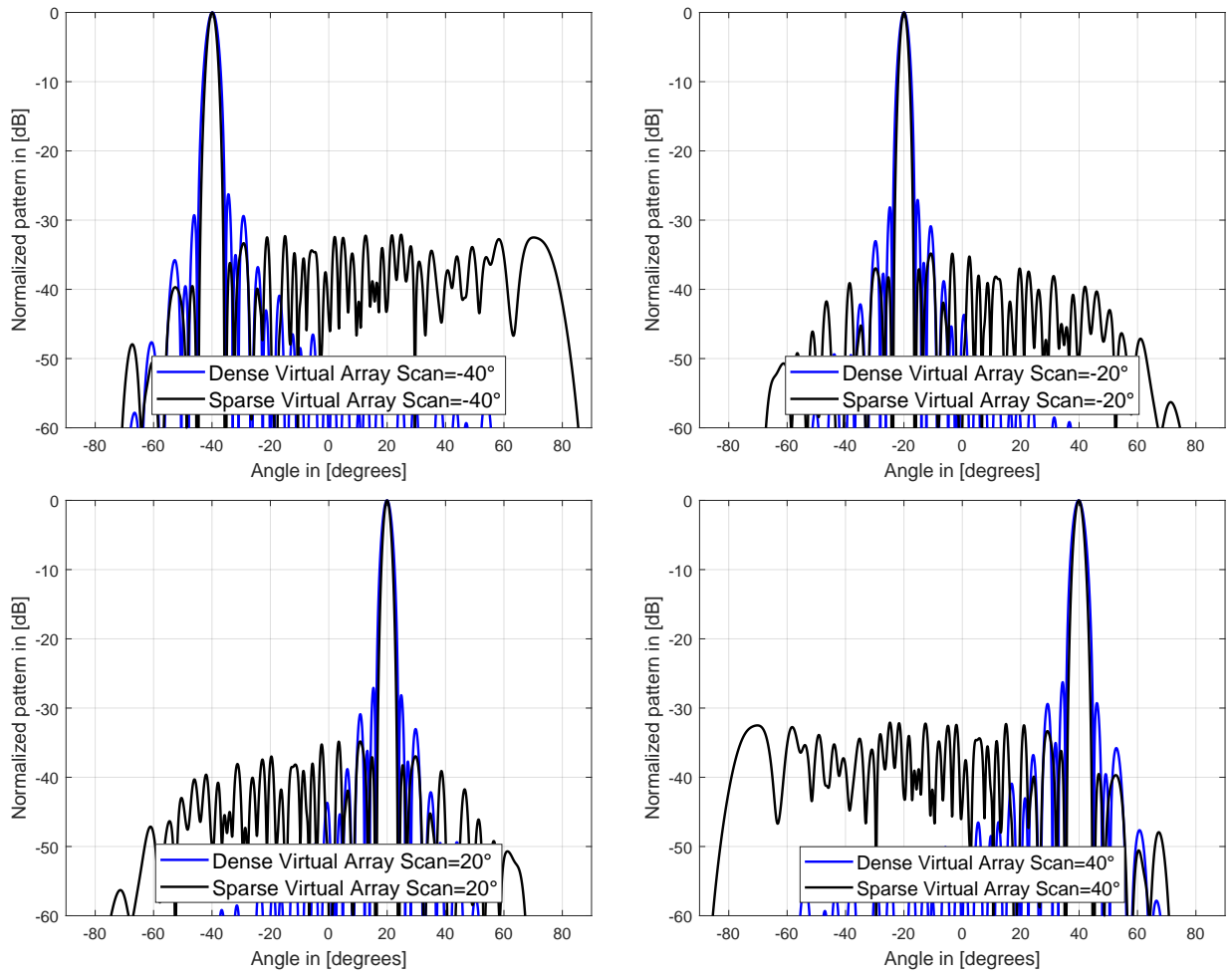


Figure 5.11: MIMO virtual array patterns at scan angles -40° , -20° , 20° and 40° for sparse configurations and the equivalent dense configuration.

Moreover, the scan behavior of the virtual array is shown in Fig. 5.11 for four different scan angles, i.e. $\theta_{\text{scan}} = -40^\circ, -20^\circ, 20^\circ, \text{ and } 40^\circ$. This figure shows that grating lobes do not appear in the scan range and that the maximum side lobe level is well below -30 dB. Thus, with this synthesis procedure an improvement in beamwidth and SLL can be achieved for a MIMO radar array with a sparse configuration for both the transmit and the receive array, especially for scanning up to the maximum scan angle. It is important to mention here that for some radar applications a SLL higher than -30 dB is acceptable. In such cases, the SLL threshold for the transmit and/or receive array can be relaxed, which ultimately results in either more sparsity or more improvement in beamwidth of the virtual array.

5.4.2 Method II: Virtual array synthesis using the method of least squares

Now, we use the receive array with $N_r = 31$ elements from the TSP as shown in Fig. 5.7 and determine the transmit array element positions \mathbf{d}_t with number of elements $N_t = 20$ using the optimization formulation formulated in Section 5.3.3. In (5.7), the maximum length of the array is set to be $\pm L = \pm 10\lambda_0$ and $d_{\min} = 0.5\lambda_0$. The optimized transmit, receive, and virtual array element positions are shown in Fig. 5.12 and the corresponding array patterns are shown in Fig. 5.13. In this example, the desired virtual array element position vector \mathbf{d}'_v is obtained by using (5.4) for $d_t(n) = 2n\lambda_0/2$ with $n = -N_t/2, -(N_t - 1)/2, \dots, N_t/2$ and $d_r(n) = n\lambda_0/2$ with $n = 0, 1, \dots, N_r$. The desired and realized virtual array positions related to the number of virtual array elements are shown in Fig. 5.14.

It can be seen that the synthesized virtual array length is large as compared to the dense virtual array and thus results in a narrow beamwidth. Also, note that the synthesized transmit array in Fig. 5.12 is nearly symmetric across positive and negative x-axis, but it is inconsequential because the array pattern is determined by the relative positions of the elements. The comparison of the dense, conventional, and sparse virtual array for broadside scan is shown in Fig. 5.15. In comparison to the equivalent dense virtual array (blue line), the synthesized virtual array (black line) has a 3° improvement in beamwidth (i.e 41%) and a 7 dB improvement in maximum SLL (indicated by the blue and black horizontal lines). However, in comparison to the conventional array (red line), the synthesized virtual array has a much lower side lobe level (indicated by the red and black horizontal lines). Thus, it is shown that with our sparse configuration synthesis of the virtual array the best of CASES I and II can be obtained.

For the four scan angles $\theta_{\text{scan}} = -40^\circ, -20^\circ, 20^\circ, \text{ and } 40^\circ$, the virtual array patterns are shown in Fig. 5.16. It is shown that no grating lobes appear while scanning and

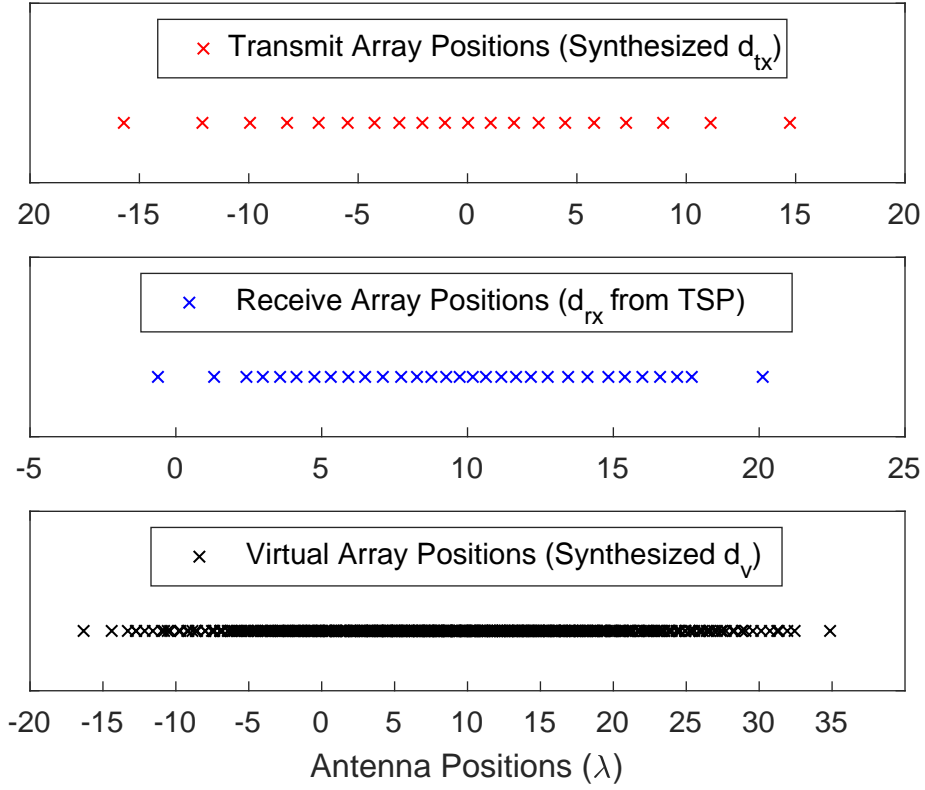


Figure 5.12: Transmit array element positions synthesized using Method II, with receive array element positions from the TSP (from Fig. 5.7) and virtual array element positions using (5.4).

the maximum SLL remains below -20 dB for the maximum scan angle of $\theta_{\text{scan}} = 40^\circ$. Also, the side lobes around the main beam are lower as compared to the larger angles, but the maximum value does not exceed -20 dB, which is acceptable for most radar applications.

It is useful to mention here that this virtual array synthesis procedure can be used to further increase the system resolution by selecting different desired virtual array positions \mathbf{d}'_v with a larger slope in Fig. 5.5. Also, the value of L_r can be increased or decreased based on the physical design requirements.

In comparison to the Method I, the SLL performance of this method is slightly deteriorated especially at higher scan angles. However, the beamwidth in case of Method II is improved by 1.8° . This is because of the fact that the transmit array in Method II is a larger sparse array as compared to the transmit array of Method I. Hence the advantage of Method II is that it allows to improve the beamwidth and be as close as possible to CASE II of MIMO virtual arrays.

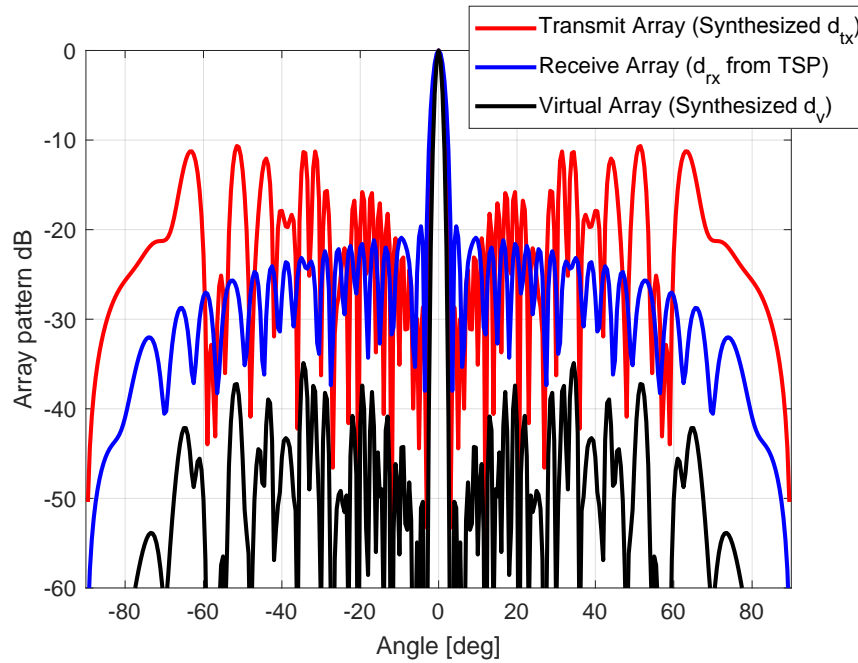


Figure 5.13: Transmit, receive, and virtual array patterns at broadside for the optimized sparse configurations in Fig. 5.12.

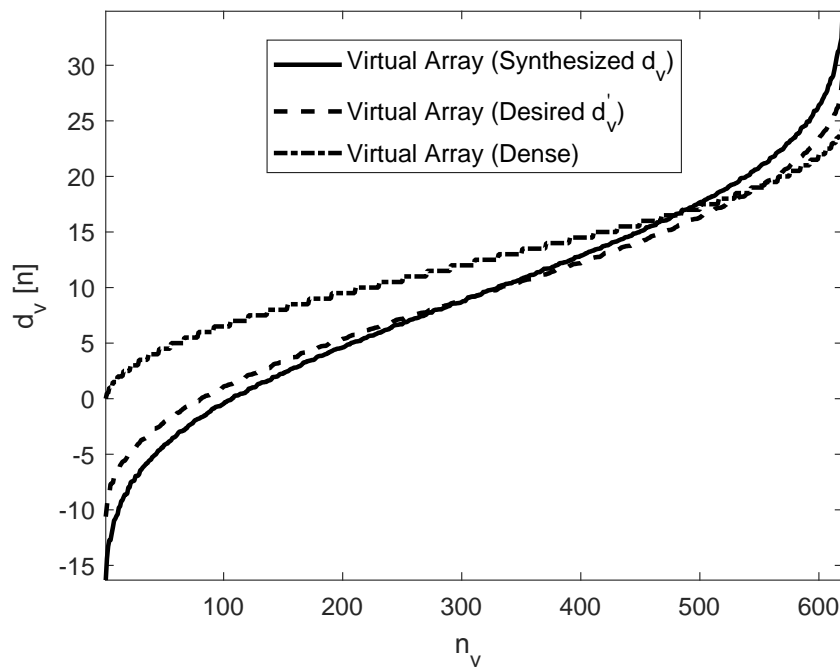


Figure 5.14: Position versus number of elements: desired, synthesized (realized), and dense comparison. Note that the y -axis represents the total length of the virtual array.

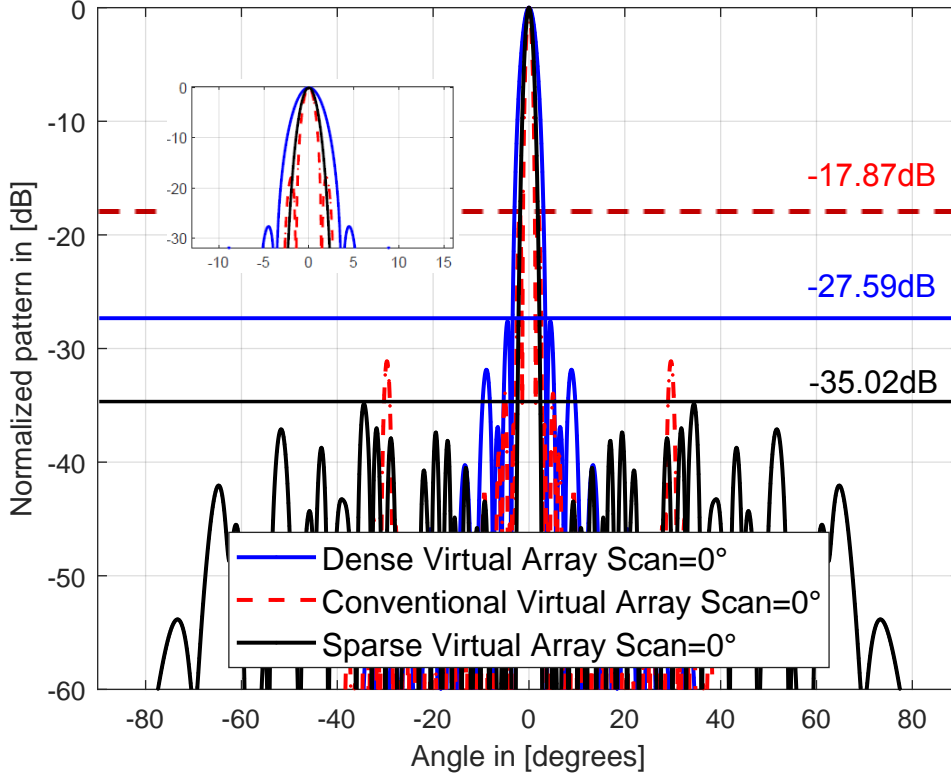


Figure 5.15: MIMO virtual array patterns at broadside for the sparse configurations and the equivalent dense and conventional configuration. The margins for maximum side lobe are shown for each plot.

5.5 Validation using full-wave solver

The two numerical examples of the two proposed methods, presented in Section 5.4, have been implemented in a full-wave solver (CST Microwave studio). For this purpose, a single-layer patch antenna has been used at 64 GHz, which has been matched in the range of 62-64 GHz, and the transmit and receive arrays of these patch antennas with the configurations obtained from the two proposed methods (Figs. 5.7 and 5.8 and Fig. 5.12) have been implemented in CST. Assuming that the separation between the transmit and receive physical arrays is sufficiently large, such that the coupling between the transmit and receive arrays is negligible, the transmit and receive arrays are simulated individually [102]. The virtual array patterns are obtained for transmit and receive arrays synthesized with Method I and are shown in Fig. 5.17 for three scan angles. In addition, the virtual array patterns are obtained for transmit and receive arrays synthesized with Method II and are shown in Fig. 5.18 for three scan angles. It can be seen that in comparison to Fig. 5.11 and Fig. 5.16, the virtual array performance is in good agreement with the results of the synthesis models. However, in particular at the maximum scan angle 40° , the side lobe levels are 3-4 dB higher because of the

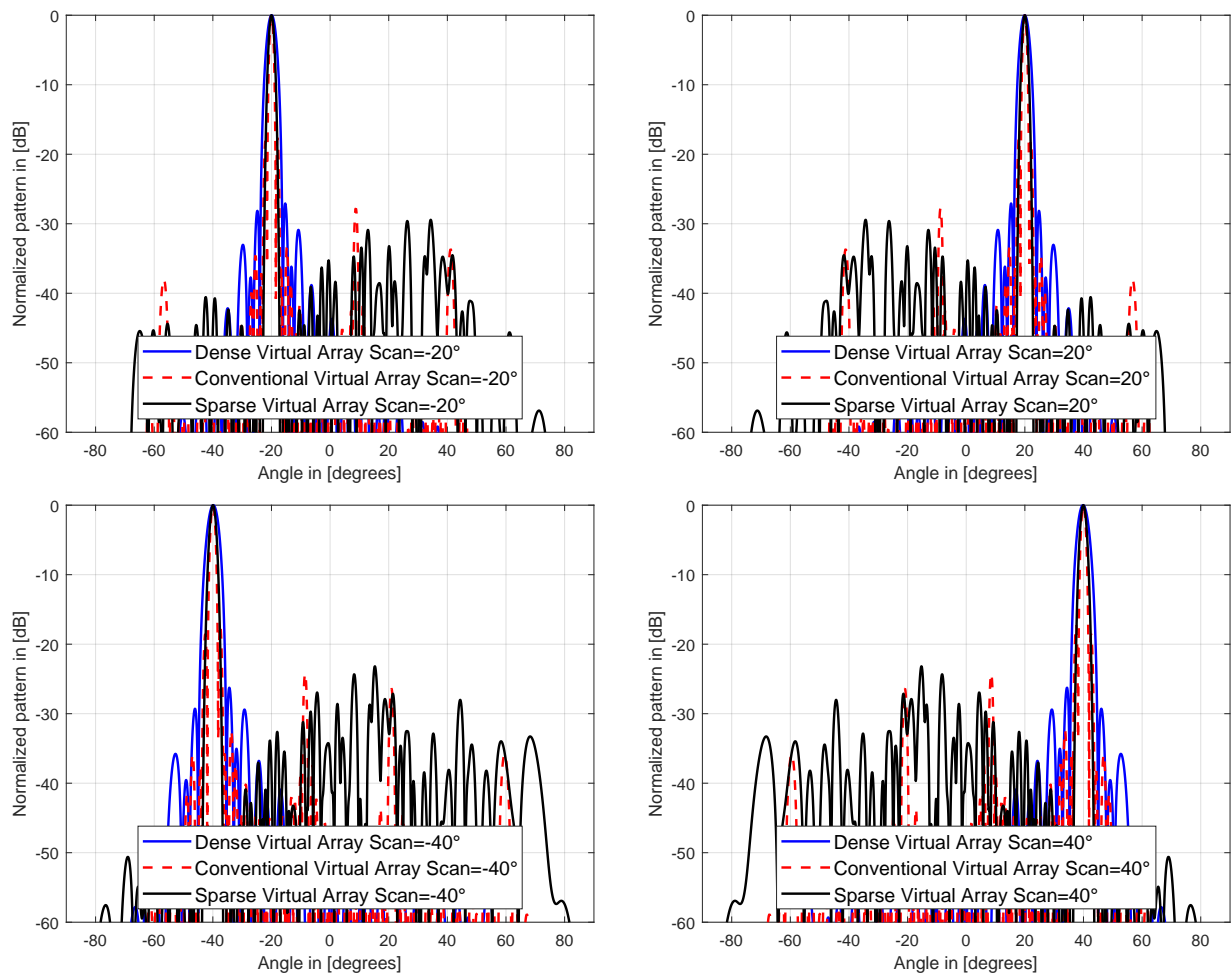


Figure 5.16: MIMO virtual array patterns at scan angles -40° , -20° , 20° and 40° for sparse configurations and the equivalent dense and conventional configuration.

mutual coupling between the array elements of the TX array and/or RX array. For the purpose of clarity, a vertical line at maximum side lobe level at 40° obtained from only Matlab synthesis models is added in each graph. The positions used for the transmit and receive arrays for wavelength at 64 GHz are given in Table 5.2.

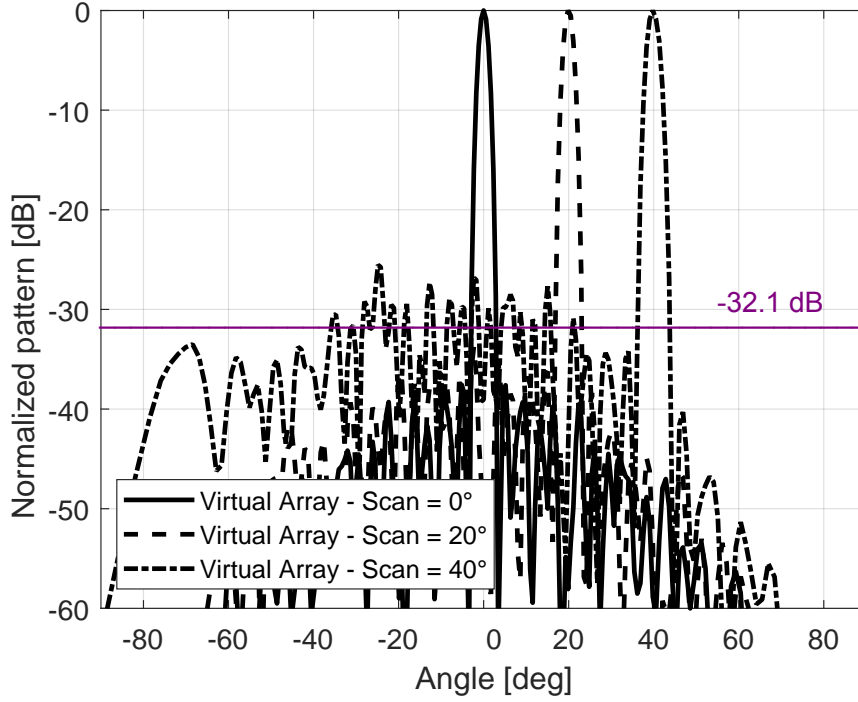


Figure 5.17: Full-wave simulation results of MIMO virtual array patterns at 0° , 20° and 40° for the sparse configurations of Method I.

While considering scanning in an array system, another parameter of importance is the scan loss. When the main beam is scanned to a larger angle, the peak gain of the array is reduced because of the element patterns [19]. In Fig. 5.19, the peak gain over the scan angles for the transmit array and receive array synthesized for both methods are shown. At the maximum scan angle the gain of the main lobe reduces by maximum 3 dB. Note that the transmit array from Method I and Method II will have a different gain even though they have the same number of elements, because the gain of the array also depends on the inter-element distance.

Table 5.2: Transmit and receive positions for Method I and II in millimeter (mm). Dimensions of patch antenna are 1.19mm x 1.52mm and dimensions of ground plane are 2.05mm x 2.20mm.

#	Transmit for Method I (mm)	Transmit for Method II (mm)	Receive for Method I/II (mm)
1	2.95	-73.84	-2.89
2	16.50	-56.96	6.16
3	21.39	-46.73	11.37
4	24.03	-38.77	14.02
5	26.77	-31.98	16.80
6	29.38	-25.75	19.44
7	33.78	-19.98	22.33
8	36.03	-14.64	24.97
9	38.60	-9.70	27.80
10	42.04	-4.84	30.50
11	49.79	0.12	33.36
12	53.26	4.99	36.31
13	56.68	9.99	38.86
14	59.26	15.29	41.17
15	61.76	20.98	43.56
16	65.05	27.20	45.73
17	67.68	34.07	47.85
18	70.91	42.03	49.97
19	77.19	52.24	52.44
20	87.20	69.28	54.82
21			57.21
22			59.93
23			63.21
24			66.33
25			69.70
26			72.35
27			75.18
28			78.03
29			80.78
30			83.14
31			94.57

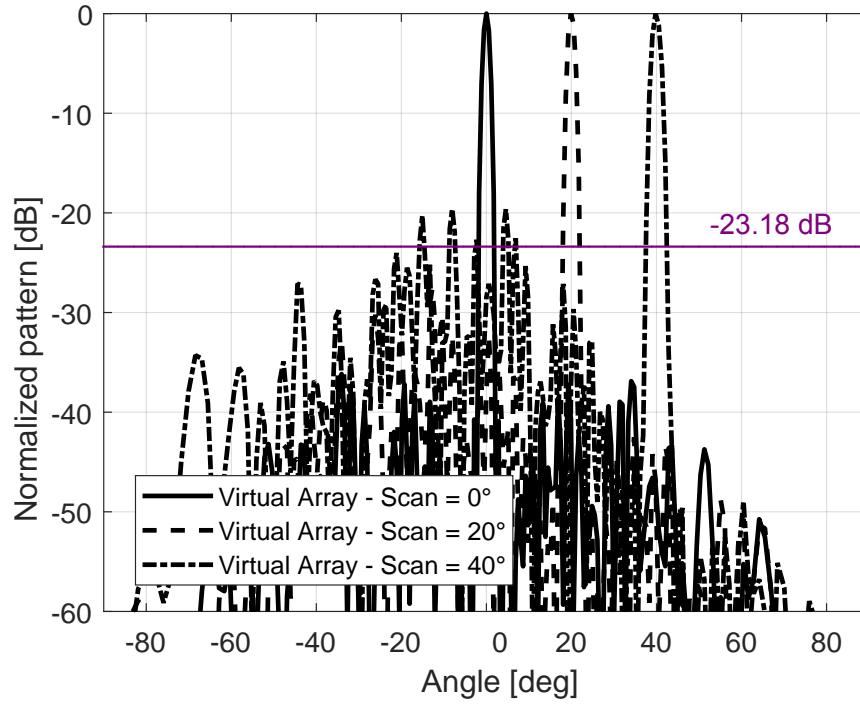


Figure 5.18: Full-wave simulation results of MIMO virtual array patterns at 0° , 20° and 40° for the sparse configurations of Method II.

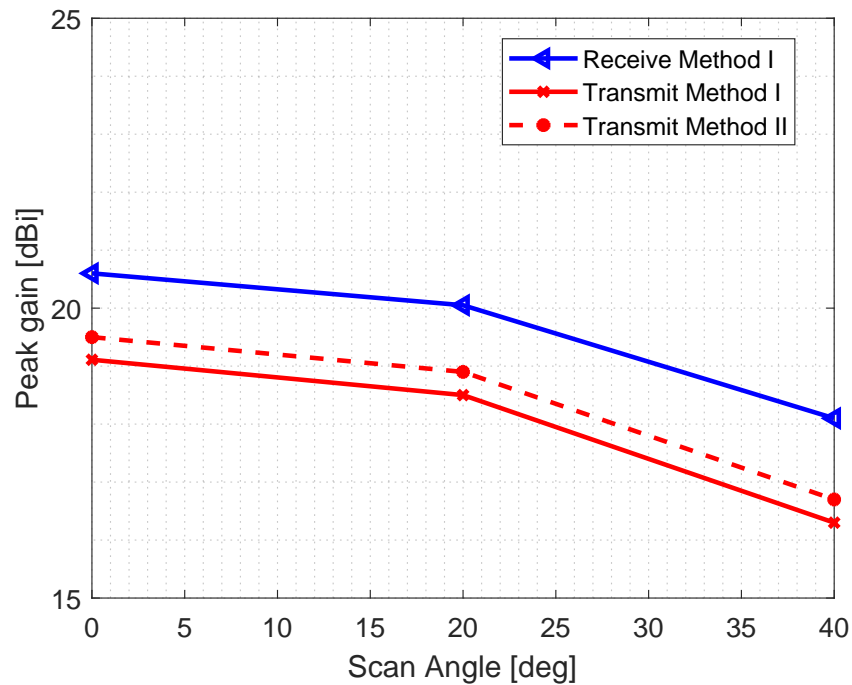


Figure 5.19: Peak Gain versus the scan angle for receive array of Method I and transmit array of Method I and II.

5.5.1 Mutual coupling inclusion in optimization

Although the full-wave simulation validated the two proposed methods for the claim of scanning without appearance of grating lobes in the FOV, it has however raised an issue of mutual coupling between the physical array elements which ultimately increased the side lobe level of the focused virtual array pattern. Therefore it is important to include the effects of mutual coupling while synthesising the array. In the case of MIMO radars and virtual arrays, the physical arrays are the transmit and receive arrays, and the mutual coupling between their elements can be accounted for by considering the Embedded Element Pattern (EEP) of each antenna element, which is the element pattern of a single element which is embedded into a large/infinite array.. These EEPs deviate from the cosine antenna patterns that we assumed in Section 5.4 for the numerical examples of the two methods. In order to include the effects of mutual coupling, instead of using a simple cosine pattern in the synthesis of the transmit and receive arrays, the EEPs of all the elements obtained from the CST simulations are used in STEP II of Eq. 5.6. This allows to further adjust the positions of the array elements while taking into account the mutual coupling and keeping the minimum distance.

As an illustration, we take the transmit and receive arrays of the numerical example of Method I in Section 5.4 and the EEPs from the CST simulations. We then perform STEP II of TSP procedure with the simulated EEPs instead of ideal cosine patterns and obtain a new configuration for both transmit and receive arrays. The virtual array patterns after including the mutual coupling are shown in Fig. 5.20, for maximum scan angle 40° . It can be seen that by taking into account the mutual coupling between the array elements while synthesising the transmit and receive arrays in Matlab, the simulated virtual array pattern from CST is more closely related to the synthesized pattern from Matlab.

5.6 Discussion on strengths and limitations

The methods presented in preceding sections can be used for a wide variety of applications because the preset parameters and formulations of the optimization problems can be adjusted according to the design requirements and physical limitations induced by the application. Therefore, an array designer has the freedom to make several adjustments that still fit the framework of the methods proposed such that desirable results can be achieved. Furthermore, by choosing λ_0 to be the wavelength at the maximum frequency of the required band of operation and by selecting θ_{\max} to be the maximum scan angle in the required FoV, we guarantee that no grating lobes appear in the FoV even for the entire frequency band of operation. The reason for this is that, in (5.5) and

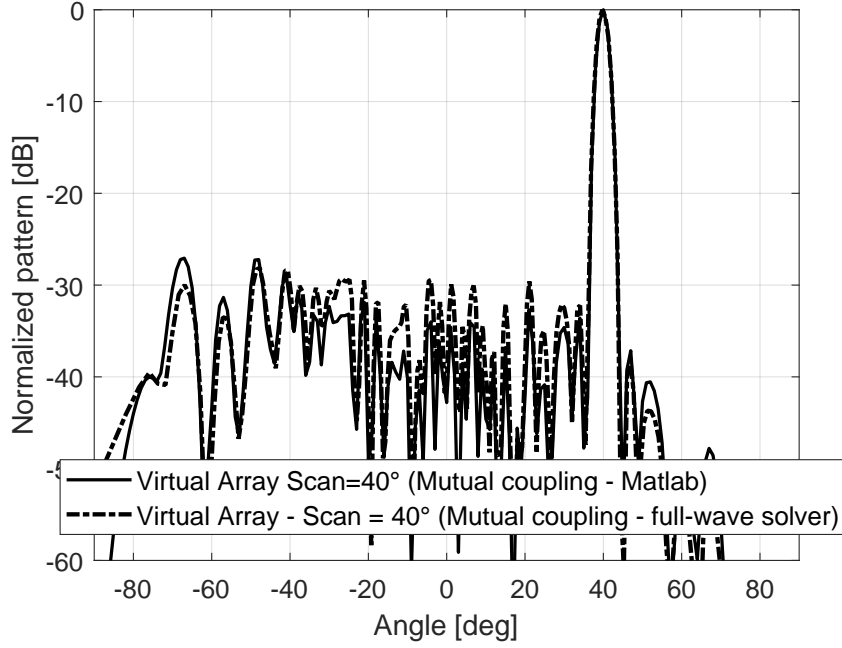


Figure 5.20: MIMO virtual array patterns at 40° for the sparse configurations of Method I after including the mutual coupling.

(5.6), the constraints on SLL and minimum distance do not allow the average element-spacing of the sparse array to exceed the critical value at which it will result in the appearance of grating lobes in the FoV at the maximum frequency of operation [97]. Thus, for any frequency below the maximum it will not result in the appearance of grating lobes. Therefore, the synthesized sparse array is broadband, which was verified by means of simulations. However, the physical effects of bandwidth on the performance of the array, such as distortions in element patterns and variation in element input impedance due to mutual coupling, can be incorporated in the design by co-simulation with a full-wave solver, as presented in [77].

It is worthwhile to mention a few general limitations of the realization of sparse transmit and receive arrays in MIMO radars. Firstly, the feeding of antenna elements in a sparse array can be a challenging task because the feed lines from RF channels to the antenna are not of equal length for every element in the array, which can result in a complex design for the feed network, especially for a large array. This is relevant, in particular, in time division multiplexing (TDM) mode in MIMO radars, since the reception in this mode is simultaneous and requires equal length of the feed lines [104]. Secondly, the phase and amplitude errors caused by the manufacturing tolerances on the element positions and electronics can result in higher SLL and an increase in beamwidth, which should be addressed while realizing the sparse arrays. Last, in target-detection radar imaging systems, the use of the Fast-Fourier Transform (FFT) is desirable for the evaluation of the angle of arrival, which assumes a regular spatial sampling in the

antenna arrays, i.e. a regular inter-element distance. Thus, the FFT is not suitable for irregular sparse arrays. Several non-uniform FFT algorithms have been proposed in literature, e.g. [111, 112], and this problem has been efficiently solved especially for the case of MIMO radars in [12].

5.7 Conclusion and future work

Two methods for the synthesis of sparse virtual array have been proposed, formulated and illustrated with numerical examples. Both methods determine the topology of the sparse transmit and receive array, which results in a sparse virtual array design. In the first method, both transmit and receive array element positions are independently determined using a Two-step Synthesis Procedure for the antenna array sparsity, which also has been formulated and explained. In the second method, the sparse transmit array element positions are determined using the TSP, while the receive array positions are determined using the method of least squares and depend on the transmit array element positions.

It has been shown with the help of numerical examples that while synthesising a sparse array via the TSP, if the element positions are determined with the main beam at the maximum scan angle, no grating lobes appear while scanning over the whole FoV. Further, it has been shown that a sparse virtual array can achieve a better performance in terms of beamwidth and side lobe level, as compared to the equivalent dense virtual array. An improvement of a maximum of 3° in beamwidth and a maximum of 7 dB side lobe level is reported in the examples. Furthermore, in the presented formulations of the synthesis methods, physical limitations on the maximum size of the arrays and minimum element spacing can be included, which allows for these methods to be used in wide variety of applications.

In the future, it is valuable to include the gain of the array into consideration for the synthesis of sparse arrays for MIMO radar, since the gain of a linear array also depends on the distance between the array elements and it strongly affects the signal-to-noise ratio of these kinds of systems.

Virtual array pattern measurements using a VNA

For the experimental validation of a synthesized MIMO array, the radiation patterns, the side lobe level and the beamwidth of the virtual array under scanning conditions needs to be characterized. A method is proposed to evaluate only the antenna part of a MIMO radar without the need to design and construct a complete radar platform. Consequently, a measurement strategy for the characterization of the radiation pattern performance of the virtual array is developed, by using only a two-port VNA and emulating the TDM MIMO mode of the MIMO radar. For the transmit and receive array, an open-ended waveguide antenna (OWA) array is designed where each individual array element is selected separately using a sliding plate for the transition from coaxial to rectangular waveguide. With the help of measurements, the virtual array pattern is reconstructed with a beamwidth and side lobe level that are comparable to those obtained from simulations.

6.1 Introduction

MIMO radars in the mm-wave regime have received a lot of attention from the research community in the past decade. These radar platforms have become well established in recent times and are now easily available off-the-shelf for research and educational purposes, for example [54, 63, 100]. These sensor platforms form a complete set-up with RF electronics hardware, antenna array, signal processing unit, software and detection algorithms and are able to provide precise radar measurements such as range, velocity and direction of arrival of the target in the radar FOV. However, for an antenna engineer, the angle estimation measurement is of particular interest because it allows to characterize the performance of the virtual array, which is based on the configuration of the physical transmit and receive arrays. To improve the performance of the radar platform, an antenna designer is required to design a configuration for the transmit and receive arrays that is different from the one that is standard or conventional and is already available via commercial radar platforms, for example the configurations designed with the synthesis of sparse virtual arrays from Chapter 5.

For the experimental validation of such a synthesized array, the radiation pattern, the side lobe level and the beamwidth of the virtual array under scanning conditions needs to be characterized. For such a characterization, a MIMO radar platform with the synthesized sparse transmit and receive arrays should be designed that can perform the complete MIMO radar functionality. The need to design for the complete radar platform including the RF electronics, baseband electronics, signal processing unit and firmware etc., similar to the system discussed in Chapter 3, is a heavy burden to validate the intended virtual array performance [113]. It requires a great deal of integration of sub-components and the virtual array angular measurements are obtained by processing the signals received in the baseband frequency range. This makes the problem a signal processing one and it becomes much more complex to separate the performance of the antenna array from the performance of the other system components. The development of an entire radar platform seems to be an overwhelming task for an antenna engineer who only requires the validation of the configuration of the designed transmit and receive arrays by characterizing the radiation pattern of the virtual array [114].

Furthermore, an important characterization parameter for array design validation is the measure of the embedded element patterns of individual elements at mm-wave frequencies and the mutual coupling analysis of the antennas embedded in the array as determined from the S-parameters. Both these parameters cannot be directly measured when the array elements are integrated with the RF front end and signal processing unit of the radar platform. An alternate approach is to obtain these parameters using a VNA that connects directly to the array elements. This has been presented in literature and is used in [115] for the case of a linear array of Vivaldi antennas. However, the use

of a VNA to emulate MIMO radar functionality, particularly at mm-wave frequencies, has potential challenges, such as phase stability of cables due to movement and the implementation of TDM functionality for MIMO radars with a two-port VNA.

Therefore, there is a clear need to develop a method for the evaluation of only the antenna part of a MIMO radar without the design and construction of a complete radar platform. Consequently, a measurement strategy for the characterization of the radiation pattern performance of the virtual array is developed by using only a two-port VNA and by emulating the TDM MIMO mode of a MIMO radar. The antenna designer then only needs the transmit and receive physical arrays and a two-port VNA to determine the sidelobe level and beamwidth of the virtual array.

6.2 Measurement strategy

For a MIMO radar, the physical arrays are the transmit and receive arrays. Assume that the transmit and receive arrays are colocated and can be individually fed by a feeding port. With a two-port VNA, one port is attached to an element of the transmit array and the second port is attached to an element of the receive array. With a sequence of measurements that emulates a TDM MIMO mode, a virtual array pattern can be recreated by determining the angle of arrival of the target signal from the measured S_{21} parameter. The measurement procedure is explained in detail below.

6.2.1 Emulating TDM MIMO mode using a two-port VNA

As explained in Chapter 2, the TDM MIMO mode is one of the possible modes in which a MIMO radar can operate. In this mode, the orthogonality between the transmit channels can be achieved in the time domain, which means that the transmit elements transmit signals sequentially. If there are N_t transmit elements and N_r receive elements, then in a TDM MIMO mode, the first transmitter transmits while all the receivers ($n_r = 1, \dots, N_r$) receive the reflected signal from the target simultaneously. After that, the second transmitter transmits and all the receivers simultaneously receive the reflections of the second transmitted signal. This process is repeated, until the last transmitter ($n_t = N_t$) transmits the signal and the reflections are received by all the receivers. In this way, a total of $N_t \times N_r$ reflected signals are received and these are processed to determine the virtual array pattern.

To achieve the above mentioned TDM MIMO mode, radar platforms have very sophisticated electronics, integrated with the antenna elements, that can perform the

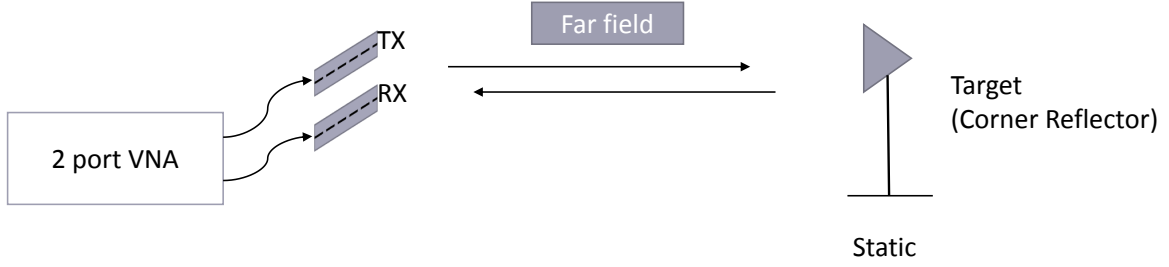


Figure 6.1: Illustration of measurement set-up for the emulation of the TDM MIMO mode with a two-port VNA.

switching between the transmitters and simultaneously handle the reception from the receivers. However, for the validation of the performance of the configuration of physical transmit and receive array and characterization of the virtual array, this TDM MIMO mode can be emulated with only a two-port VNA, which is mostly available in the lab. An impression of the measurement set-up is shown in Fig. 6.1 and the procedure is explained below with the help of Fig. 6.2 and Fig. 6.3.

For setting up the measurement, Port 1 of the VNA is first attached to the first transmit element (T1) and Port 2 of the VNA is attached to the first receive element (R1) of the colocated TX/RX array, as shown in Fig. 6.1 and in the top picture of Fig. 6.2. A corner reflector as a target is placed at a distance that is larger than the minimum far-field distance of the TX/RX array. The S-parameter matrix of the two-port network is then measured with the VNA for the combination T1 and R1, for the range of frequencies of interest. The parameter of interest here is S_{21}^{T1R1} , that is used to determine the virtual array pattern and is given by the equation:

$$|S_{21}^{T1R1}(\theta)|^2 = G_{T1}(\theta)G_{R1}(\theta)\sigma_{tgt}(\theta) \left(\frac{\lambda_0^2}{4\pi^3 R^4} \right), \quad (6.1)$$

where σ_{tgt} is the RCS of the target, G_{T1} and G_{R1} are the gain of the transmit element and receive element, respectively, λ_0 is the free-space wavelength, and R is the distance between the target and the TX/RX array. Note that the S_{21} parameter is angle θ dependent and when the target is placed at a distance in the far field, the angle of incidence from the transmit array and the angle of reflection from the receive array are the same [116]. Thus, the position of the target determines the scan angle of the virtual array pattern. Also, equation (6.1) assumes that the signal reflected from the target is much stronger than the signal received via other paths such as reflections from the surroundings, coupling of the transmit and receive antennas and the noise present in

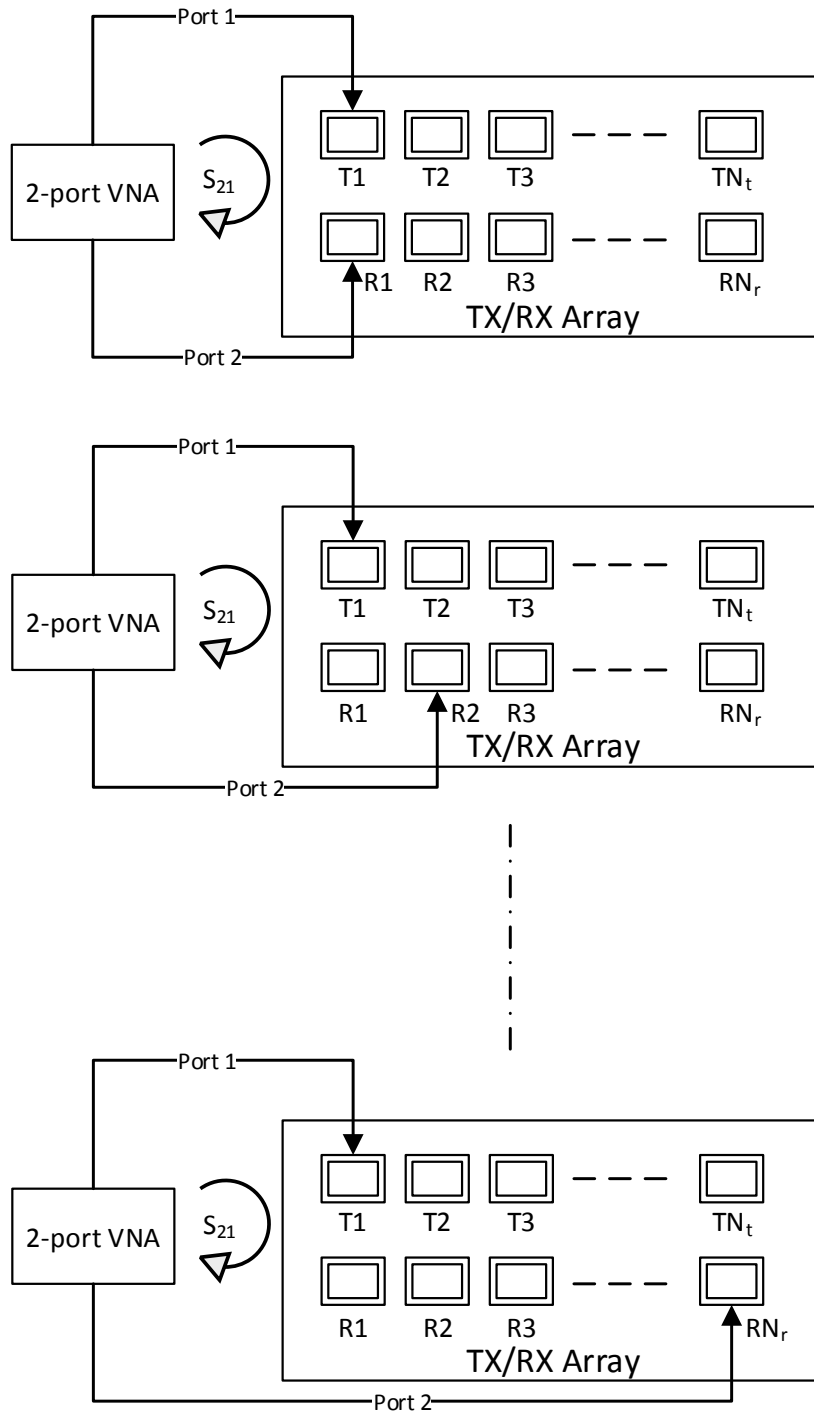


Figure 6.2: The sequence of measurements for the combination T1 and R1- RN_t with a two-port VNA. The top figure shows the setting for combination T1 and R1, the middle shows the combination T1 and R2, and bottom shows the combination of the T1 and RN_r .

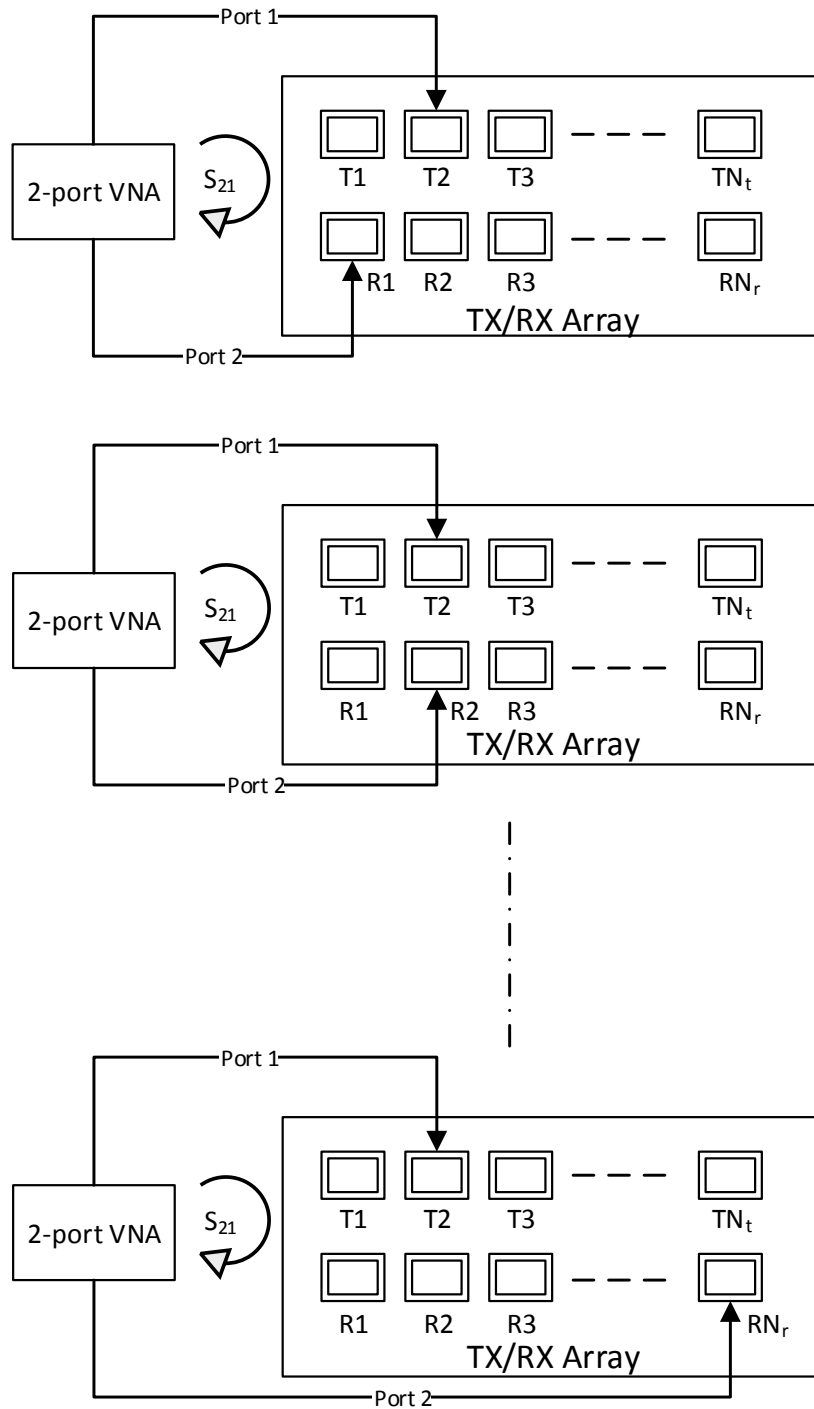


Figure 6.3: The sequence of measurements for the combination $T2$ and $R1$ - RN_t with a two-port VNA. The top figure shows the setting for combination $T2$ and $R1$, the middle shows the combination $T1$ and $R2$, and bottom shows the combination of the $T2$ and RN_r .

the measurement system [18].

In the next step, Port 2 of the VNA is moved manually to the second receiver element (R2), while Port 1 is still attached to transmit element (T1), as shown in the middle of Fig. 6.2. The S_{21}^{T1R2} parameter is measured for this combination of T1 and R2. This procedure is repeated for all the receiver elements (1 to N_r) while transmit element T1 remains connected to Port 1 of the VNA, see also the bottom picture in Fig. 6.2. These sets of measurements allow to measure N_r S_{21} parameters for all the combinations from T1R1 to T1R N_r . Note that as long as the environment remains static, the movement of Port 2 from receiver element R1 to R N_r is equivalent to the simultaneous reception of the reflected signal by all the receivers in TDM MIMO mode.

Next, Port 1 of the VNA is manually moved from transmit element T1 to transmit element T2 and the whole procedure explained above is repeated, which is also depicted in Fig. 6.3. With this set of measurements, another N_r measurements of the S_{21} parameter are obtained, but now for the combination T2R1 to T2R N_r . When this procedure is repeated for all the transmit elements (1 to N_t), then $N_t \times N_r$ S_{21} parameters have been measured. These S_{21} parameter complex values are given by

$$S_{21}^{T_{n_t}R_{n_r}} = |S_{21}^{T_{n_t}R_{n_r}}| e^{jk_0 d_{v,n} \sin \theta_{tgt}}, \quad (6.2)$$

which can then be used to determine the virtual array pattern of the TX/RX array by using the following equation (cf. (5.3)):

$$\mathbf{A}\mathbf{F}_v(\theta) = \sum_{n_t=1}^{N_t} \sum_{n_r=1}^{N_r} |S_{21}^{T_{n_t}R_{n_r}}| e^{-jk_0 d_{v,n} (\sin \theta - \sin \theta_{tgt})}, \quad (6.3)$$

where $d_{v,n}$ is the n -th element of the position vector \mathbf{d}_v given by Equation (5.3) and θ_{tgt} is the angular position of the target. Using this procedure and equation, the characterization of the virtual array pattern for any collocated configuration of the transmit and receive arrays in a MIMO radar can be performed, for example for the sparse configurations designed in Chapter 5.

6.2.2 Measurement and calibration challenges

The procedure, explained in Section. 6.2.1, emulates the TDM MIMO mode of the MIMO radar but with the condition that the whole measurement environment remains static. However, because of the movement of the ports of the VNA from one transmit or receive position to another, the environment can not be perfectly static. The movement

of the ports means movement of the cables attached to the ports of the VNA and alignment errors after the movement. This will result in uncertainty in the measurements and gives rise to calibration challenges.

Therefore, it is important to take into consideration how to minimize the effect of these movements and remove the effect caused by the movements. The full two-port calibration of the VNA including the cables is performed before starting the sequence of measurements, which establishes a reference plane of the calibration at the end of the cables. However, when a port of the VNA needs to be moved, the cables are also moved, which means that amplitude and phase errors induced by this cable movement will not be included in the calibrated VNA anymore. Therefore, re-establishing the reference plane of the calibrated VNA is required after each movement. For this purpose, after the full two-port calibration of the VNA, a one-port calibration needs to be applied to the port involved in the movement. To solve these challenges, two solutions are proposed in this section and later on in Sections 6.3 and 6.5, these solutions are experimentally validate using the developed test structures.

In the first solution, an effort is made to minimize the movement of the cables and thus reduce the errors introduced by the movement. Two points are considered in this effort. First, it is made sure that the cables used for the measurements are both low-loss and phase-stable such that the induced amplitude and phase errors are negligible. This aspect is critical at mm-wave frequencies because it has been shown in literature that the stability of coaxial cables is a critical factor in phase stability [117, 118]. Second, while designing the TX/RX array for validation, sliding plates and alignment pins are introduced to minimize the movement of cables as much as possible. This is further explained in Section 6.3.

For the second solution, the reference plane of the calibration that is established after the two-port calibration at the start of the measurement procedure is re-established after each movement of the port with the help of a one-port calibration of the moved port. This is achieved by representing the measurement set-up, shown in Fig. 6.4, by a cascade of scattering matrices (S-matrices) associated with the various sections of the set-up. The cascaded S-parameter representation of the set-up in Fig 6.4, is shown in Fig. 6.5.

The signal path in Fig. 6.4 can be divided into five sections: cable 1 (from the VNA to the transmit element), forward free-space (from the transmit element to the corner reflector), reflections from the corner reflector, backward free-space (from the corner reflector to the receive element) and cable 2 (from the receive element to the VNA). With the calibrated VNA, the S-matrix of the entire cascade is measured, which is represented here by \mathbf{S}_{total} . This S-matrix can then be modeled as the cascade of the S-matrices for each of the sections stated above and this is illustrated in Fig. 6.5. According to the measurement strategy, Port 2 of the VNA is connected to the first

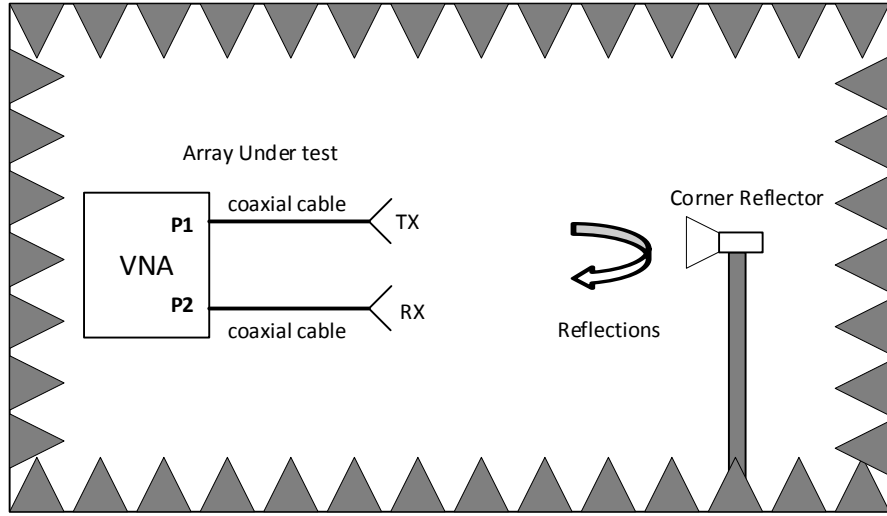


Figure 6.4: Measurement set-up for obtaining the virtual array pattern with a two-port VNA.

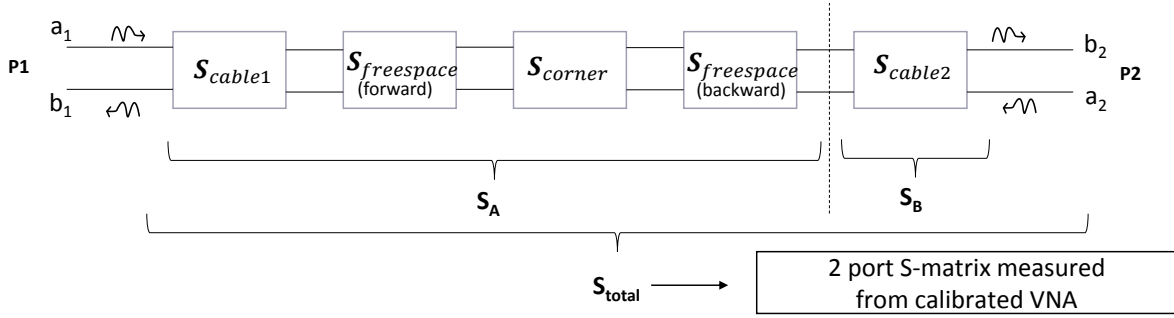


Figure 6.5: The cascaded S-parameter representation of the measurement set-up of Fig. 6.4.

receiver element and is then moved to the second receiver element, as in Fig. 6.4. This means that cable 2 is moved and potential errors are then induced in the measurement. To compensate for these errors, the cascade that forms \mathbf{S}_{total} is constructed by means of the Redheffer star product (\star) of two matrices, \mathbf{S}_A and \mathbf{S}_B , represented by the following equation [119]:

$$\mathbf{S}_{total} = \mathbf{S}_A \star \mathbf{S}_B, \quad (6.4)$$

or

$$\begin{bmatrix} S_{11} & S_{12} \\ S_{21} & S_{22} \end{bmatrix}_{total} = \begin{bmatrix} S_{11}^A & S_{12}^A \\ S_{21}^A & S_{22}^A \end{bmatrix} \star \begin{bmatrix} S_{11}^B & S_{12}^B \\ S_{21}^B & S_{22}^B \end{bmatrix}. \quad (6.5)$$

As shown in Fig. 6.5, the matrix \mathbf{S}_A includes the sections of cable 1, forward free-space, corner reflector reflections, and backward free-space, which are not affected by the movement of cable 2. However, \mathbf{S}_B is represented by \mathbf{S}_{cable2} , which *is* affected by movement and this needs to be compensated for in the measured data. Note that in (6.5) the matrix \mathbf{S}_A corresponds to a static environment, in agreement with the condition put in Section 6.2.1. Therefore, if matrix \mathbf{S}_A is calculated and used in (6.3) to determine the virtual array pattern, then the errors induced by the movement of cables should be removed, as detailed below.

Note that in (6.5), the matrix \mathbf{S}_B needs to be known in order to determine matrix \mathbf{S}_A . Therefore, \mathbf{S}_B is measured using a one-port calibration technique, by measuring for three different loads; short, open, and load, attached to the end of cable 2 using the following set of equations [120, 121]:

$$\begin{aligned} S_{11}^B &= \Gamma_{in}^L, \\ S_{22}^B &= 1 - 2 \left(\frac{\Gamma_{in}^L - \Gamma_{in}^S}{\Gamma_{in}^O - \Gamma_{in}^S} \right), \\ S_{12}^B S_{21}^B &= (\Gamma_{in}^L - \Gamma_{in}^S)(1 + S_{22}), \end{aligned} \quad (6.6)$$

where Γ_{in}^S , Γ_{in}^O and Γ_{in}^L represent the measured reflection coefficients at Port 2 of the VNA, while cable 2 is terminated by a short, an open, and a load, respectively. Note that here a perfect short, open, and load are assumed. In (6.4), \mathbf{S}_A can now be determined

from the measured values of \mathbf{S}_{total} and \mathbf{S}_B . The simplified equations for \mathbf{S}_A are [119]

$$\begin{aligned} S_{11}^A &= S_{11} - \left(\frac{S_{12}S_{21}S_{11}^B}{S_{12}^B S_{21}^B} \right) \left(1 - \left(\frac{(S_{22}^B - S_{22})S_{11}^B}{A} \right) \right), \\ S_{12}^A &= \left(\frac{S_{12}}{S_{12}^B} \right) \left(1 - \left(\frac{(S_{22}^B - S_{22})S_{11}^B}{A} \right) \right), \\ S_{21}^A &= \left(\frac{S_{21}}{S_{21}^B} \right) \left(1 - \left(\frac{(S_{22}^B - S_{22})S_{11}^B}{A} \right) \right), \\ S_{22}^A &= \left(\frac{(S_{22}^B - S_{22})}{A} \right), \end{aligned} \tag{6.7}$$

where $A = S_{11}^B S_{22}^B - S_{22} S_{11}^B - S_{12}^B S_{21}^B$. S_{21}^A is then calculated for each combination of transmit and receive element, and (6.3) is then used to determine the virtual array pattern, which is then free from the errors induced by the movement of the cables. Note that the S-parameters for the matrix \mathbf{S}_{total} are the ones measured by the VNA after the two-port calibration.

6.3 Design of a test case with 3 transmit and 4 receive physical element arrays

In order to validate the strategy of measuring the virtual array pattern proposed in Section 6.2, physical transmit and receive arrays were designed and manufactured. A test case with 3 transmit and 4 receive elements is chosen for this purpose, particularly because of it being a standard commercial configuration that is used for a wide range of radar platforms, such as used in [54, 122, 123]. Moreover, the sparse regular configuration for the transmit array and the dense regular configuration for the receive array allows to design for a well known radiation pattern of the virtual array.

For this case study, an OWA is selected as a single element of each of the arrays [124]. For the reason of commercial and technological relevance, the mm-wave frequency band at 60 GHz is selected. The frequency range of interest is 62 GHz to 64 GHz. The waveguide standard used for the OWA is WR15, which has dimensions 3.7592 mm by 1.8796 mm. The wavelength at the highest frequency of 64 GHz is 4.69 mm, which means that for a $\lambda_0/2 = 2.345$ mm arrangement of the antenna elements for the dense receive array, the placement along the E-plane of the waveguides (with largest dimension, i.e. 3.7592 mm) is not possible. Therefore, an H-plane alignment of the OWAs is chosen for the design of both transmit and receive array. For the sake of simplicity, a linear array is adopted for both transmit and receive arrays, but the same procedure can be

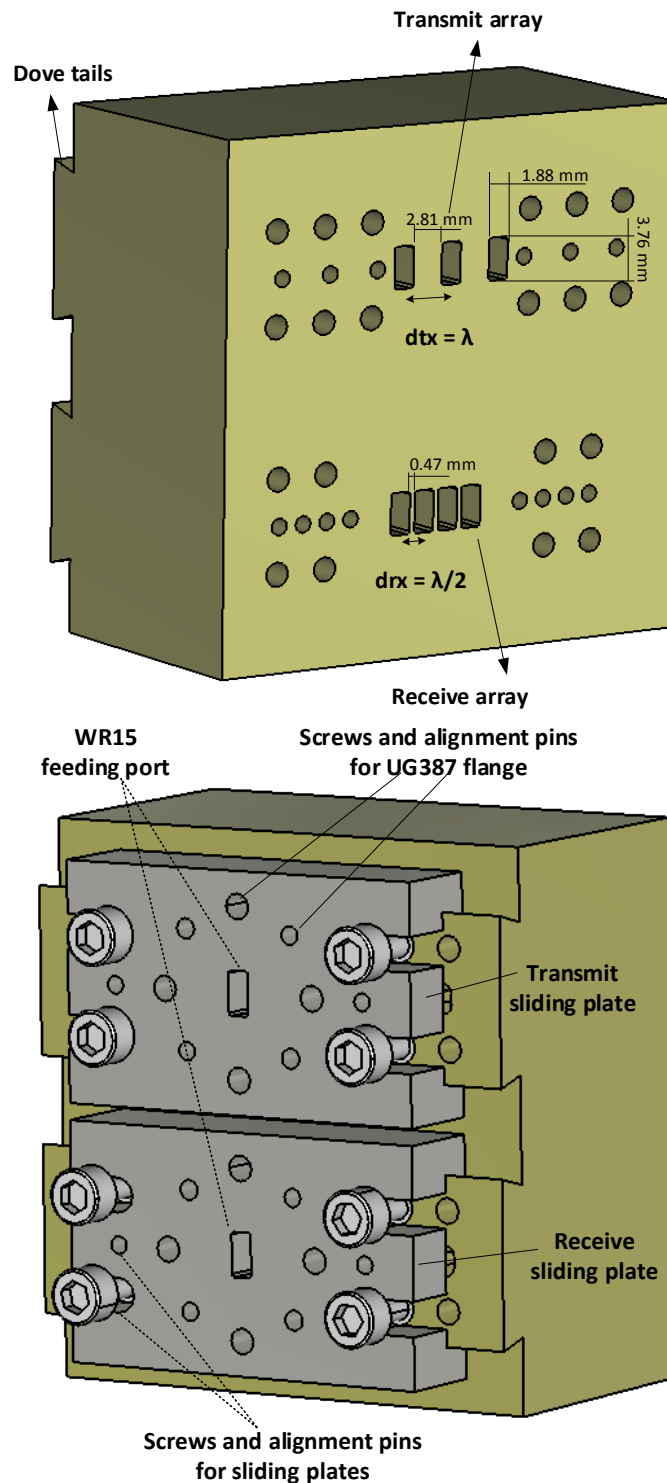


Figure 6.6: Design of the 3 transmit and 4 receive OWA arrays with sliding plates for feeding through a WR15 coaxial-to-rectangular waveguide transition. Top: front side with screw holes for termination with Short, Open and Load plates. Bottom: back side with sliding plates and dove tails, for transmit and receive feeding.

extended to planar arrays. The design for the transmit and receive OWA arrays is shown in Fig. 6.6. The arrays are designed in a metal block with the openings of WR15 standard waveguide slots from the front to the back of the metal block. At the back side, there are dovetail-shaped protrusions to feed the arrays. The front side is the radiation aperture of the OWAs.

In Section 6.2.2, the challenges to create a static environment have been addressed and the first solution proposed is to minimize the effect of movement. Here in the design process, for the purpose of smooth movement, an inventive concept to feed the array is introduced. To feed an OWA element in the array, an off-the-shelf WR15 waveguide to coaxial cable transition is used [125]. A sliding plate as an adapter is designed and is used between the WR15 transition and the back side of the metal block containing the TX/RX arrays. This sliding plate gets attached to the dovetail protrusion of the TX/RX array on one side and to the flange of the WR15 transition on the other side. The purpose of this sliding plate is twofold. First, it allows the feeding of the transmit and receive elements to be smooth and sturdy, as explained in Section 6.2. It interlocks with the dovetail on the back side of the metal block and with the help of screws and alignment pins one transmit or receive element is selected and the measurement can take place. When moving to the next element, the screws and alignment pins can simply be removed and the sliding plate is slid along the axis of the array until the next element, and screws and alignment pins are placed again. This method helps in the efficient and fluid movement of the WR15 transition and attached cables. There is no need to completely remove the WR15 transition for shifting from one element to other. In this way an effort is made to keep the environment as static as possible.

Second, when using an off-the-shelf coaxial to rectangular waveguide transition for feeding, the configuration of OWAs for a $\lambda_0/2$ spacing is not possible because the size of the standard flange for WR15 is 20 mm by 20 mm, which means that two OWA elements should have a minimum center-to-center distance of 20 mm. Therefore, the sliding plate acts as an adapter that allows to design any configuration of the transmit and receive array with the minimum distance of $\lambda_0/2$.

The second solution proposed is to compensate for the movement effects in, as discussed in Section 6.2.2, by performing a one-port calibration after every movement for the element selection. For this purpose, holes for screws and alignment pins at the front side of the metal block are placed, so that after moving the cables through the sliding plates at the back, the short, open and load termination for the WR15 OWA can be attached to the front side of the array and the one-port calibration can be performed.

Next to this, it is important to point out here is that the transmit and receive configuration used in this design is sparse regular for the transmit array with element spacing $dtx = \lambda_{64GHz} = 4.69$ mm and dense regular for the receive array with element

spacing $drx = \lambda_0/2 = 2.35$ mm. This configuration is chosen because of its well-known virtual array pattern with a maximum SLL lower than -15 dB and high isolation (< -40 dB) between the ports.

The configuration of Fig. 6.6 was simulated in CST Microwave Studio 2020 and the simulations are performed for the 12 combinations of the 3 transmit and 4 receive elements. The simulations were performed with two ports at a time to mimic the measurement procedure of Section 6.2.1. The S-parameter simulations (S_{11} , S_{21} , S_{12} and S_{22}) for all the combinations is shown in Fig. 6.7. Note that Port 1 is always attached to the transmitter and therefore S_{11} is the reflection coefficient of the transmitter and Port 2 is attached to the receiver, so S_{22} is the reflection coefficient of the receiver. S_{21} and S_{12} are the isolation between the transmitter and receiver. It can be seen that for each combination the reflection coefficient of both the transmitter and the receiver is lower than -13 dB and the isolation is below -61 dB. Note that since it is a reciprocal system, so $S_{21} = S_{12}$. This can also be observed in the right side of Fig. 6.7, where the blue and red lines are identical.

The embedded element patterns (EEP) of the transmit and receive elements for all the combinations are shown in Fig. 6.8. The EEPs for both transmit and receive OWA are smooth and show that the position of the port (middle or edge) and the size of the metal block does not introduce any ripples in the normalized patterns. Moreover, the virtual array pattern obtained from these simulation for three different frequencies, i.e. 62 GHz, 63 GHz, and 64 GHz, is shown in Fig. 6.9. The experimental validation of the simulated model is presented in the next section, in Sections 6.4 and 6.5.

6.4 Manufacturing and measurement set-up

The brass metal block containing the TX and RX arrays was manufactured by means of 3D milling and the WR15 slots were drilled through the metal block with rotary cutters. The pictures of manufactured prototype are shown in Fig. 6.10 for the back and front of the metal block and for the sliding plates. The measurement set-up in an anechoic environment is shown in Fig. 6.11. A corner reflector is placed at 47 cm distance from the array block, which is more than the minimum far-field distance of 42 cm for the TX/RX array. For the stability of the environment and the alignment of the corner reflector and the arrays, an optical table is used at the bottom and both the corner reflector and array holder are firmly attached to the table. Note that this is crucial because the environment needs to be static and identical throughout the entire measurement sequence. Also, in the experiments, the optical table needs to be covered with proper absorbers to avoid unwanted reflections.

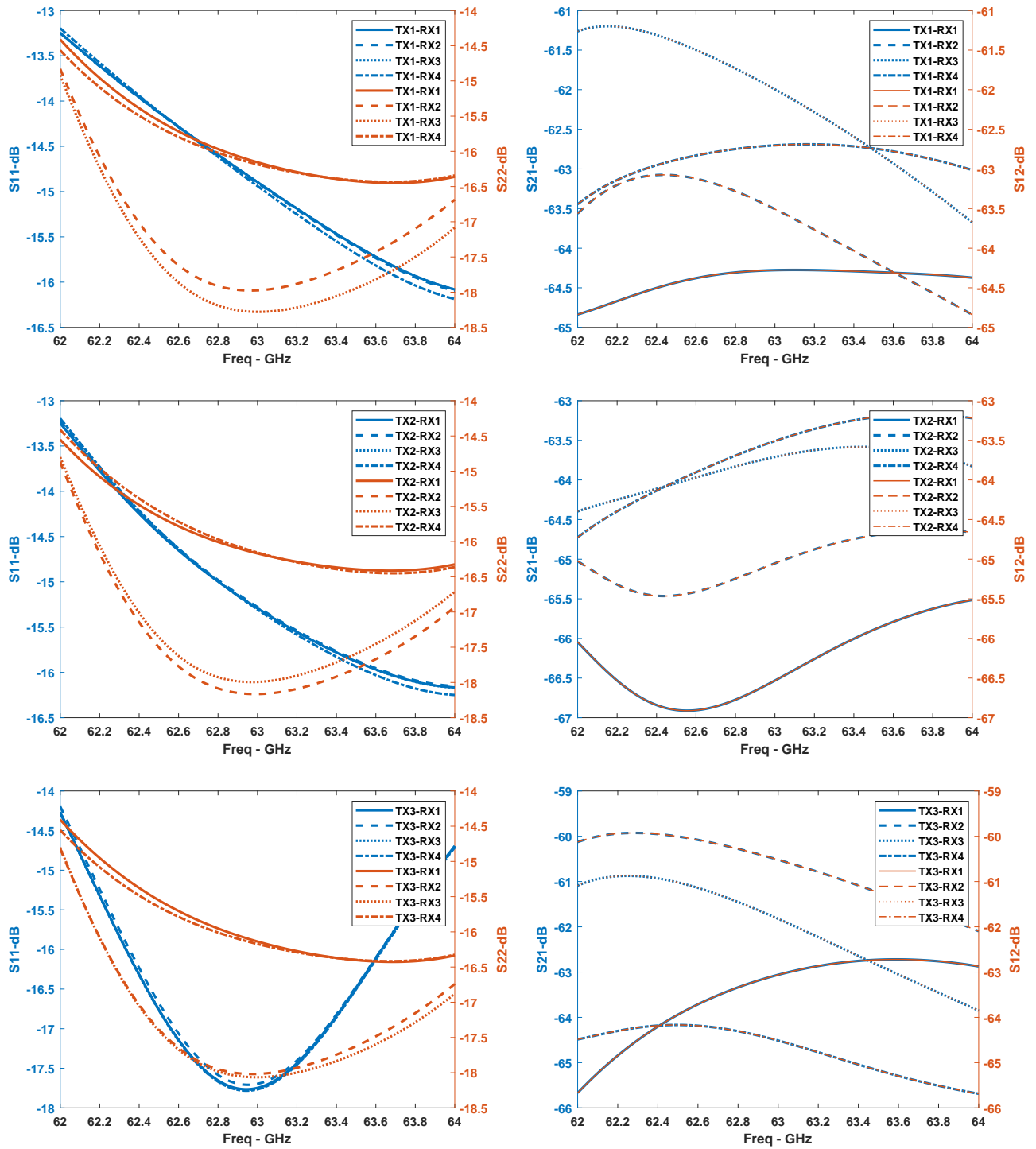


Figure 6.7: S-parameter values for all combination of transmit and receive elements.

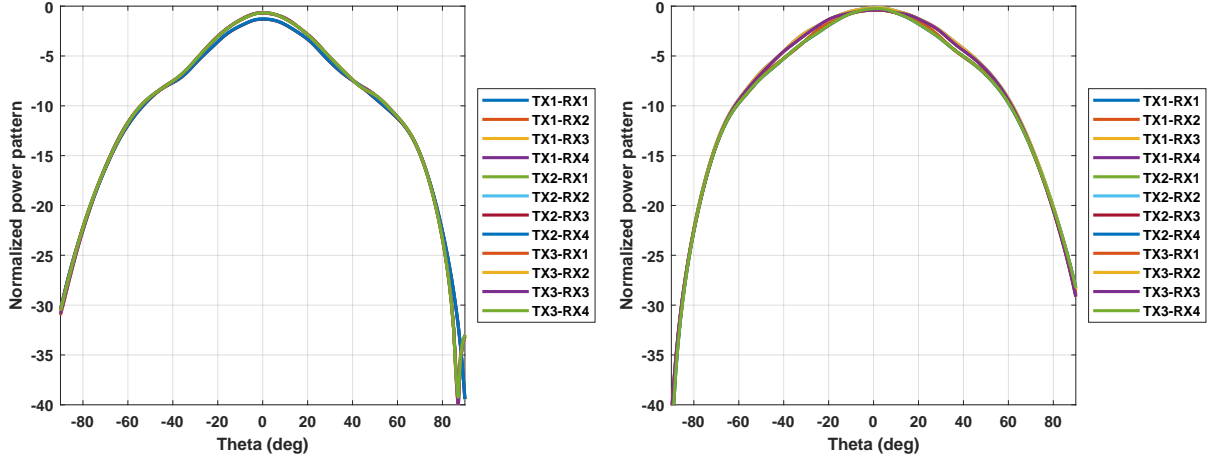


Figure 6.8: EEPs for all combinations of transmit and receive elements (legend states the combinations sets). Left: Port 1 for TX; Right: Port 2 for RX.

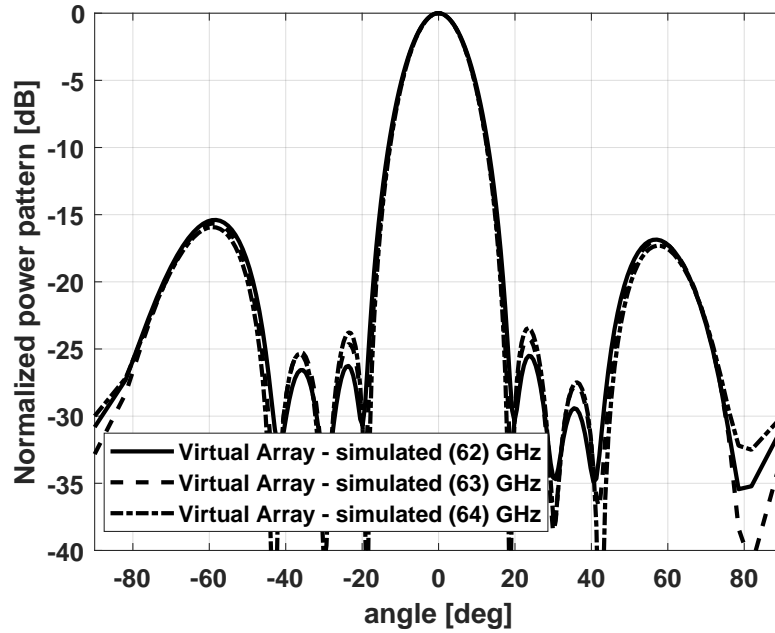


Figure 6.9: Virtual array pattern simulation for frequencies; 62 GHz, 63 GHz and 64 GHz of the TX/RX array shown in Fig. 6.6

The VNA used for these measurements is a PNA E83613 from Agilent Technologies. Port 1 of the VNA is attached to the transmit sliding plate through a coaxial cable and WR15 coaxial-to-rectangular waveguide transition. For the coaxial cable, a 1.85 mm phase-stable cable from Gore phase flex [126] is used and the WR15 transition is from Quinstar (QWA MN:15R18X) [125]. For the two-port calibration at the start of the measurement, a TC-CK-185 1.85 mm calibration kit [127] by Maury Microwave is used.

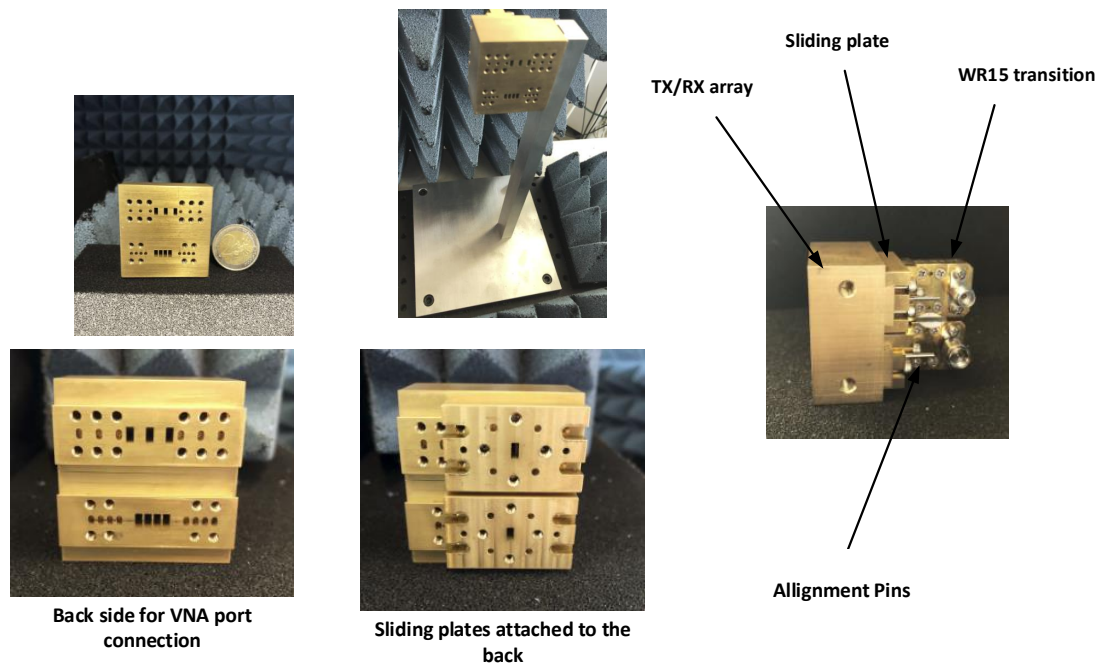


Figure 6.10: Manufactured TX/RX array. Top left: Brass metal block with TX/RX array. Top middle: with holder. Bottom left: Back side. Bottom middle: Back side with plates. Right: Side view.

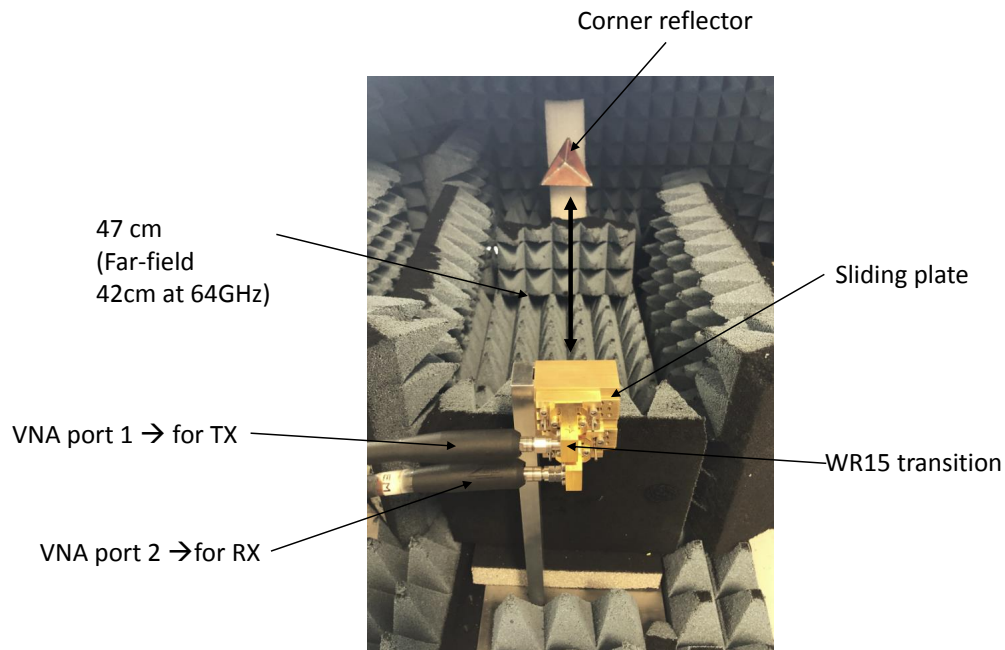


Figure 6.11: Measurement setup in an anechoic environment with the TX/RX array, WR15 transitions, and corner reflector.

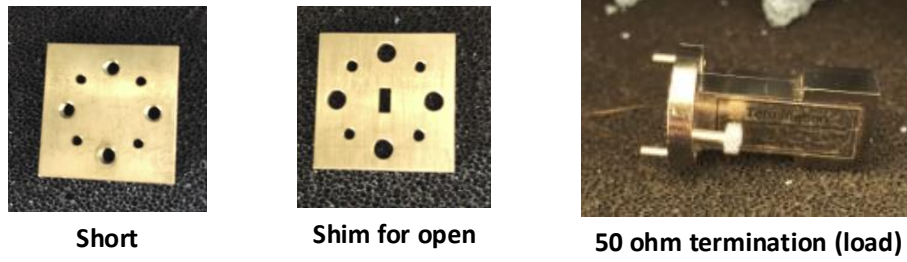


Figure 6.12: A custom-made set of calibration standards: short, shim for open and a 50 Ohm termination for load for the one-port calibration measurements at the front of the TX/RX array.

For the front calibration, applied after the movement of a cable, a set of custom-made calibration standards for WR15 waveguides is used that is shown in Fig. 6.12.

6.5 Measurement results

The corner reflector is first placed at 47 cm distance and at an angle of 0 degrees in front of the TX/RX array. The measurements for the 12 TX/RX combinations are performed as explained in Section 6.2.1. The S-parameters for each combination are measured. The measured reflection and transmission coefficients of the pair T1R1, when there is a corner reflector present in the measurement environment and when there is no corner reflector, are shown in Fig. 6.13. It can be seen that the reflection coefficients for both cases is similar and is below -10 dB for the range of frequencies of interest (62 GHz - 64 GHz). Note that this reflection coefficient is different from the one in the simulations (c.f. Fig. 6.7) because it also includes the WR15 transitions, which have a more narrow bandwidth.

From the transmission coefficients on the right in Fig. 6.13, it can be seen that without the corner reflector the S_{21} indicates that the isolation between the transmit and receive port is below -60 dB, as expected from the simulations. However, in the presence of the corner reflector, the S_{21} is increased by approximately 10 to 15 dB, which indicates the strong signal reflected from the target.

The measured S_{21} parameter for each combination is then used in Equation (6.3) and the reconstructed virtual array pattern is plotted in Fig. 6.14 for several frequencies. In this measurements result, the two-port calibration is performed up to the end of the coaxial cable. It can be seen that the side lobe level, as compared to the simulation, is approximately 6 dB higher and there are slight pointing error in the main beam. The cause of the high side lobe levels and pointing errors can be attributed to amplitude

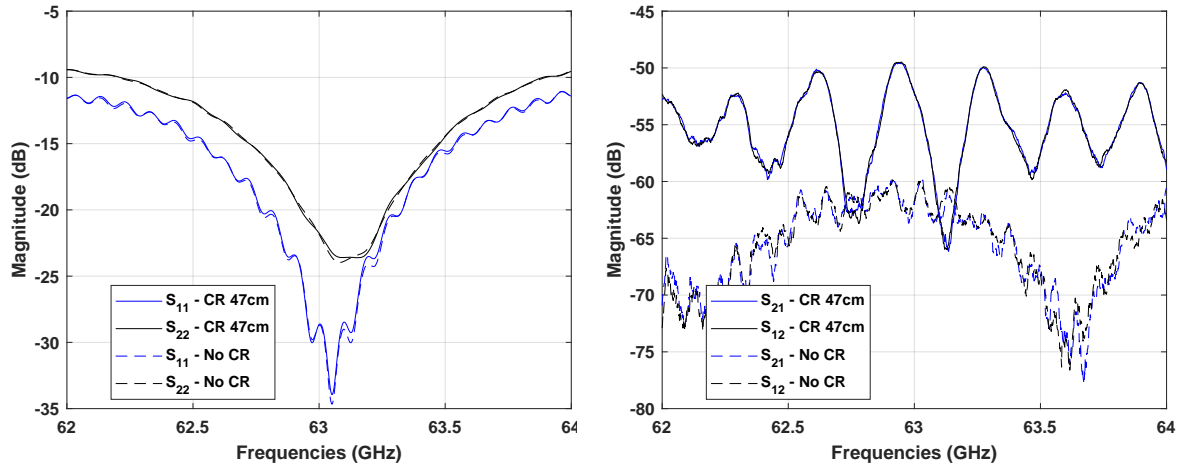


Figure 6.13: The reflection coefficient (left) and transmission coefficient (right) for the combination of T1R1 with and without the corner reflector (CR).

and phase errors, whose main source can be due to the movement of the cables and sliding plate for selecting the transmit and receive element combinations. Note that the second calibration is not applied here yet.

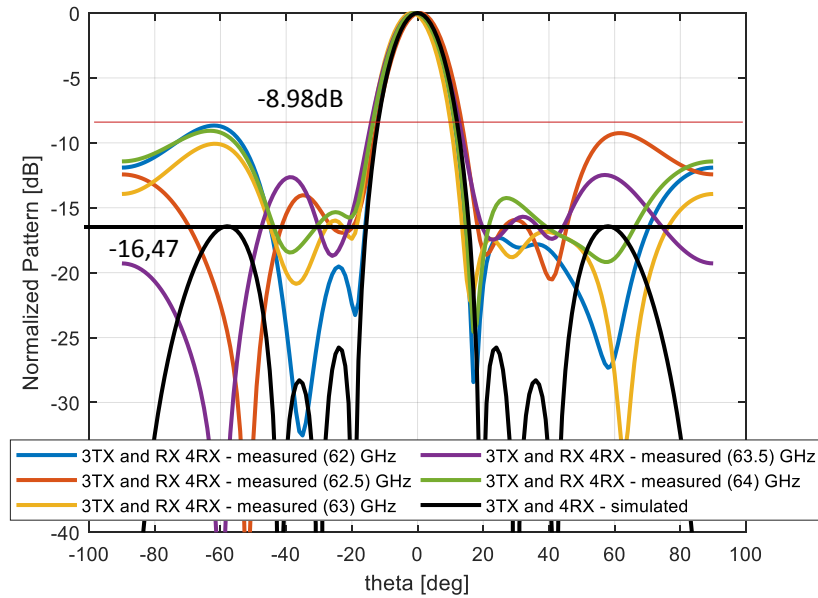


Figure 6.14: Reconstructed virtual array pattern for several frequencies with the two-port calibration at the coaxial end of the VNA.

To identify the issue of high side lobe levels, the amplitude and phase of all the 12 combinations of transmit and receive elements are analysed. The measured amplitude and phase of the S_{21} parameters are shown in Fig. 6.15. This figure suggest that the noise

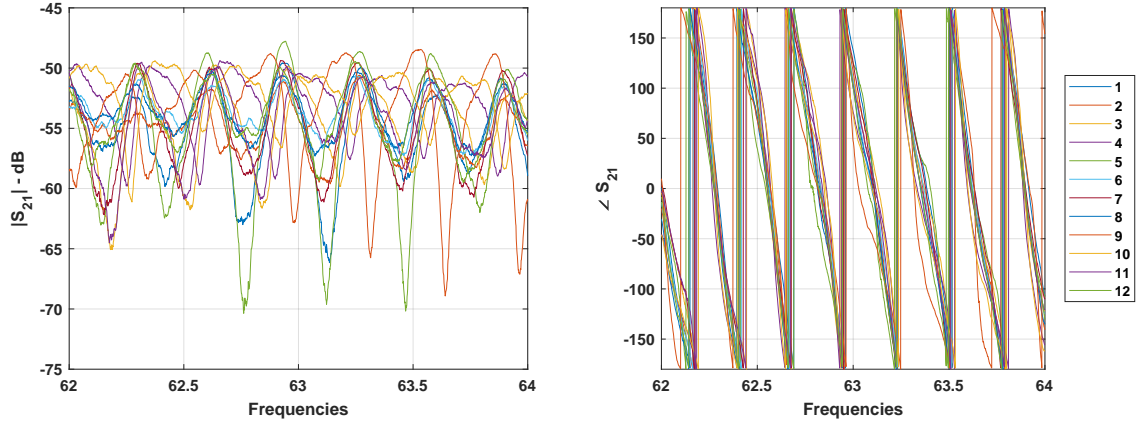


Figure 6.15: Amplitude and phase of the S_{21} parameter for the 12 combinations of the transmit and receive pairs, with each a different color as given in the legend on the right.

level in the measured data is significant, which results in amplitude and phase errors among all the combinations of transmit and receive pairs. Therefore, to improve the noise floor level in a VNA measurement, averaging over multiple repeated measurements is performed. In our case, the VNA measured data is averaged over 1000 measurements with IF bandwidth of the VNA equal to 40 kHz and the resulting virtual array pattern is shown in Fig. 6.16. It can be seen that the reconstructed virtual array pattern is now similar to that from the simulation and the highest sidelobe level is approximately below -15 dB for 62 GHz and 63 GHz.

To further compensate for the movement errors, the second solution presented in Section 6.2.2 is then applied, i.e. applying 1-port calibrations after moving a cable. The calibration standards from Fig. 6.12 are used to measure Γ_{in}^S , Γ_{in}^O and Γ_{in}^L and these are used to calculate the S-matrix \mathbf{S}_B using Equation (6.6). Subsequently, the S-matrix \mathbf{S}_A is calculated from Equation (6.7). This S-matrix is then used to determine the virtual array pattern and the result is shown in Fig. 6.17. It can be seen that the compensation for the movement leads to only a very slight improvement in side lobe level for angles in the range $\pm 60^\circ$ in the reconstructed virtual array pattern, which indicates that the use of the sliding plate has proved to be quite effective in maintaining the movement errors in measurements reasonably low.

6.5.1 Scanning

In connection with the MIMO radar virtual array performance characterization, scanning of the target for angles other than broadside is of prime interest. The procedure of emulating TDM MIMO mode for a target at a different scan angle than broadside can

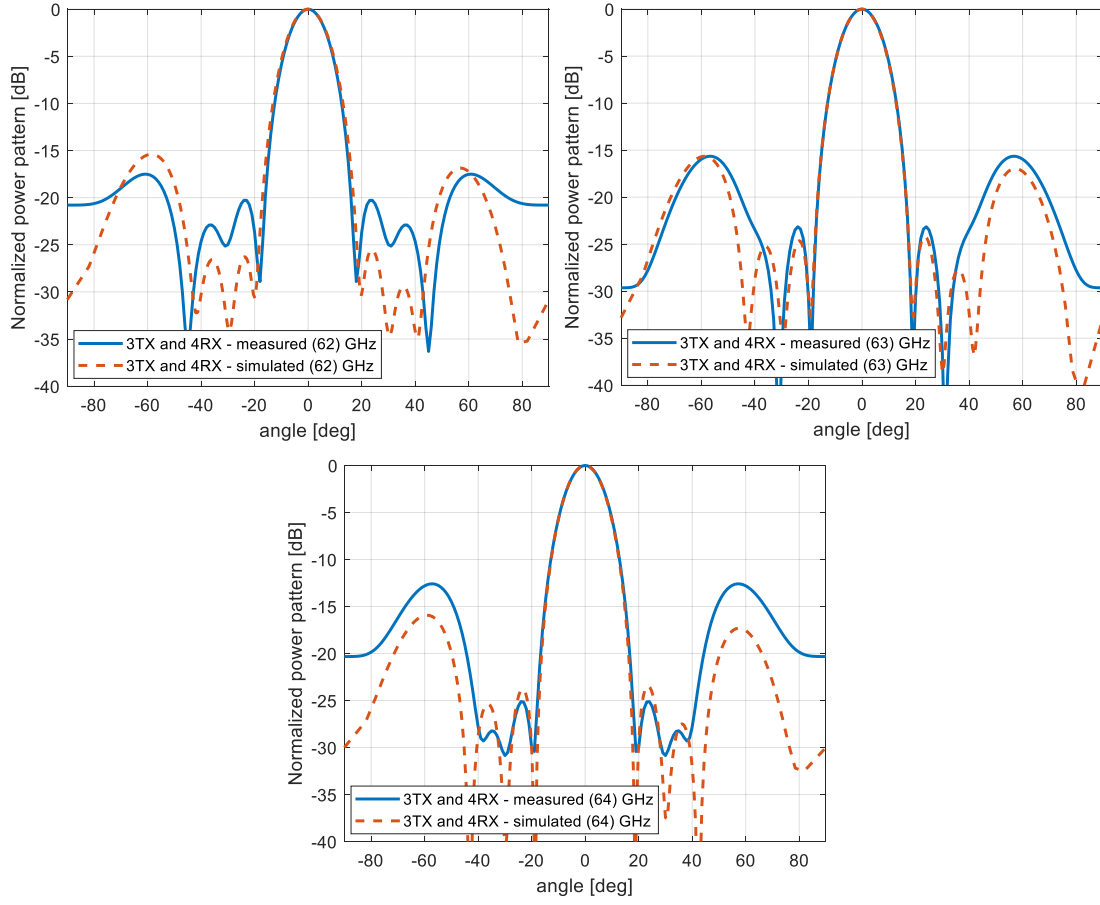


Figure 6.16: Reconstructed virtual array pattern for several frequencies with the two-port calibration at the coaxial end of the VNA using averaging.

be used to recreate the virtual array pattern for a certain scan angle. As explained in Section 6.4, an optical table has been used for stable attachment of the corner reflector and the TX/RX array, and thus the corner reflector is shifted perpendicular to the TX/RX array and the virtual array pattern is measured to determine the angle.

First, the corner reflector is placed at a distance of 50 cm in front of the TX/RX array and is then shifted 75 mm to the right, perpendicular to the broadside direction of the array, as shown in Fig. 6.18 (right). This gives a calculated angle for the target of $\theta_{tgt} = 8.53^\circ$. The reconstructed virtual array pattern by using the proposed measurement strategy is shown in Fig. 6.18 (left). It can be seen that the target angle is correctly determined from the virtual array pattern at approximately 9° .

For further validation, the corner reflector is placed at a distance of 50 cm in front of the TX/RX array and then shifted 141 mm to the right, perpendicular to the broadside direction, as shown in Fig. 6.19 (right). This gives a calculated angle for the target of $\theta_{tgt} = 15.75^\circ$. The reconstructed virtual array pattern by using the proposed measure-

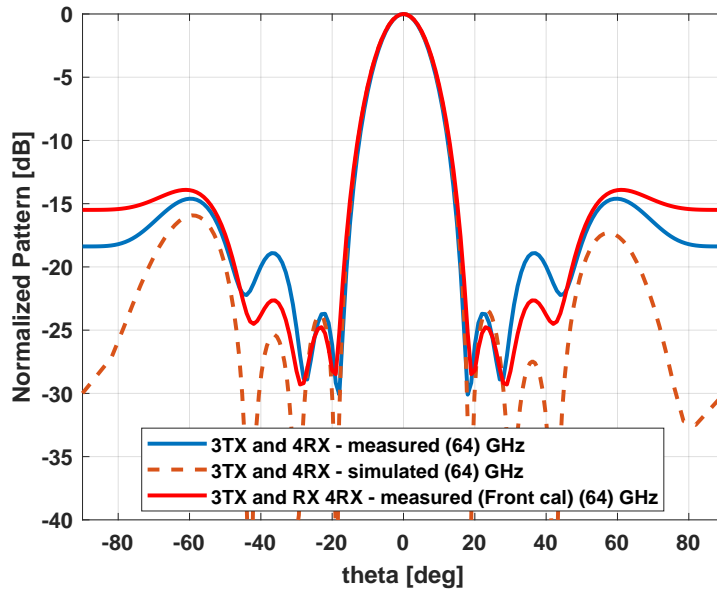


Figure 6.17: Reconstructed virtual array pattern for 63.5 GHz with the two-port calibration at the coaxial end (in blue) and with front 1-port calibration (in red).

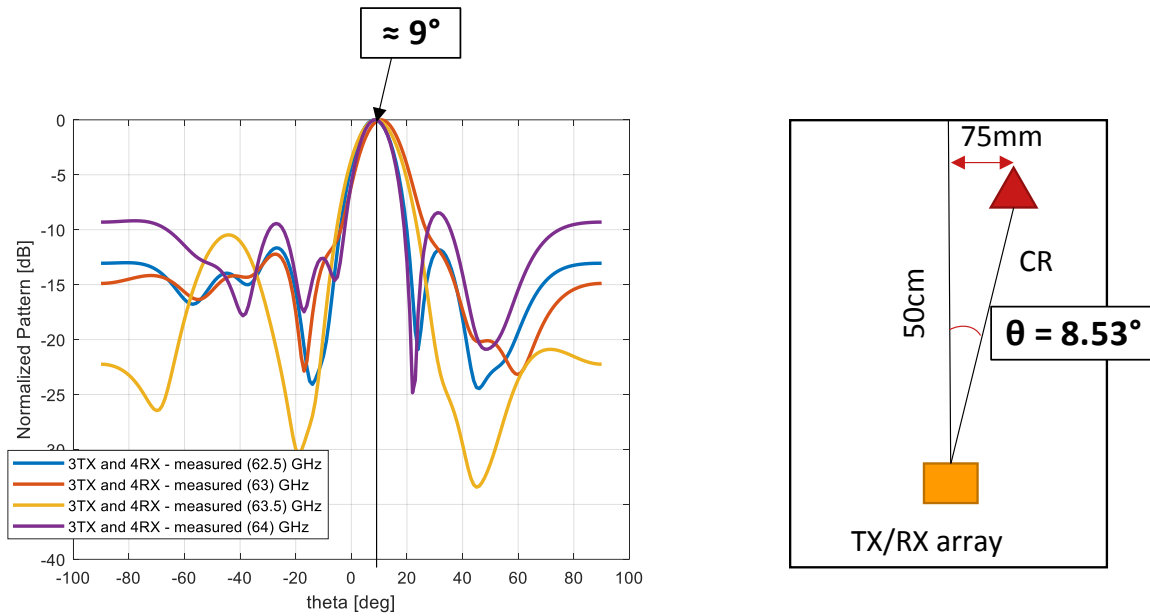


Figure 6.18: The reconstructed virtual array patterns (left) for the target at an angle determined by the scenario on the right.

ment strategy is shown in Fig. 6.19 (left). It can be seen that the target angle is again

correctly determined from the virtual array pattern at approximately 16° .

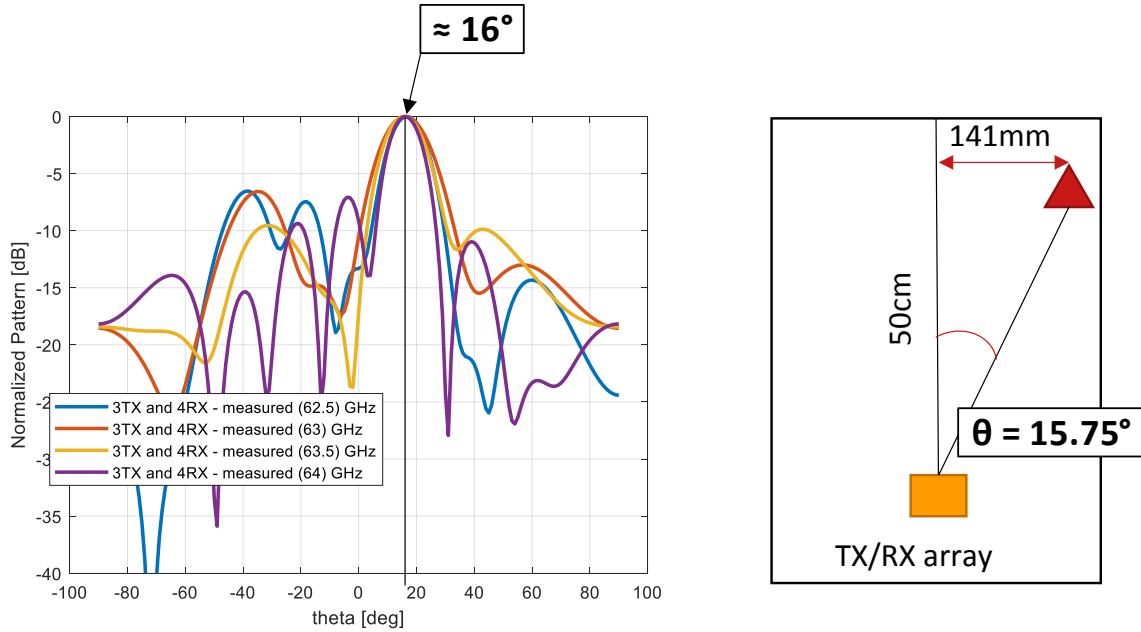


Figure 6.19: The reconstructed virtual array patterns (left) for the target at an angle determined by the scenario on the right.

Hence, the measurement results validate the measurement strategy of emulating the TDM MIMO mode for the virtual array pattern characterization of a MIMO radar by using only a two-port VNA. It is important to discuss the measurement time for this strategy. After calibrating the two-port VNA, the measurement of S-parameters for 12 combination takes approximately 15 minutes. This measurement time reflects a quite efficient procedure and is mainly achieved by means of the use of sliding plates, as they allow a smooth movement. The measurement time can be further decreased by automating the movement process instead of the manual movement used here.

6.6 Conclusion

For the characterization of the radiation pattern, the side lobe level and the beamwidth of the synthesized virtual array for a MIMO radar, under scanning conditions, a measurement strategy using only a two-port VNA and emulating the TDM MIMO mode of the MIMO radar has been formulated and verified experimentally. A test case of 3 transmit and 4 receive array elements has been used for validation purposes. For the transmit and receive array, an OWA array has been designed where each individual

element is selected separately by using a sliding plate for the transition from coaxial to rectangular waveguide. These sliding plates provide a smooth manual transition between the array elements and reduce the errors induced by the movements of the cables.

It has been shown with the help of measurements that the proposed measurement strategy allows to recreate the virtual array pattern and the measured results are in good agreement with the simulated virtual array patterns. Further, a method is also proposed to compensate for the movement errors with the help of calibration at the front side of the transmit and receive array. The measurement results showed that the front calibration results in a slight improvement in determining the side lobe level of the radiation pattern. Furthermore, the measurement strategy has been verified under scanning conditions by placing the target at different angles and recreating the scanned virtual array pattern. In summary, the proposed method of virtual array pattern measurements is an efficient method that can be used for any synthesized transmit and receive array configuration for a collocated MIMO radar.

CHAPTER SEVEN

Improved 3D imaging MIMO radar

For imaging radars, higher angular resolution is essential, yet it requires a larger number of antenna elements in enlarged regular arrays. By using antenna-array sparsity, improved imaging performance can be achieved without the increase of antenna elements and the corresponding cost. For imaging radars, the MIMO radar technique is used which improves the angular resolution of the radar by an order of magnitude. For a planar virtual array, different transmit and receive array configurations can be considered. A comparison of these configurations and their pros and cons are discussed in this chapter. Further, a virtual-array sparsity method is applied to and validated with a model of a 3D MIMO mm-wave imaging radar. Through simulations, it is shown that with a sparse transmit and receive array, an improvement in beamwidth and side lobe level in the virtual array patterns for MIMO radars can be achieved.

7.1 Introduction

High-end imaging in industrial applications is slowly progressing towards the use of full 3D radar imaging systems. The advantage of radar over other conventional imaging systems is considerably high, for example as compared to LIDAR, they are less expensive and can be used in adverse weather conditions [128] and, as compared to camera, they can maintain privacy [14]. In the field of imaging radars, mm-wave frequency ranges, such the as 57-64 GHz and 77-81 GHz bands, are used more often because of their ability to provide higher range resolutions. However, these frequencies can be a challenge for imaging systems when it comes to angular resolution [128].

For a 3D imaging radar, the three dimensions are range, azimuth and elevation and for the latter two, a planar array of antennas is required [129]. It is well known that the angular resolution of a planar array depends on the size of the array aperture [19] and thus for mm-wave frequencies, this means a large number of antennas are required. In case of a phased-array radar, it means that a large planar transmit and receive array is required that can scan in both azimuth and elevation directions. However, with a MIMO radar, with linear transmit and receive arrays, a planar virtual array can be achieved and thus a higher angular resolution can be achieved as compared to an equivalent phased-array radar. Some cases of such a configuration are listed in this chapter.

Furthermore, we will discuss planar transmit and receive arrays for MIMO radars and it is shown that instead of using a dense/dense configuration for the transmit/receive planar arrays, a sparse/dense and a sparse/sparse configuration for transmit/receive arrays results in higher angular resolution and lower side lobe levels in the virtual array patterns. For the sparse/sparse configuration, method II developed in Chapter 5 is applied and the improvement in angular resolution is shown.

7.2 Planar virtual array configurations for MIMO radars

Since the principle of operation of MIMO radars is based on the idea that the transmit signals are orthogonal and, as a consequence, this results in the virtual array concept, as explained in Chapter 2 and Chapter 5. As a result, the opportunity arises of exploiting the transmit and receive configuration to achieve the best possible configuration of the virtual array. This has been the focus of work in Chapter 5, but here the same concepts are applied for the case of a planar virtual array. The two categories of transmit and receive arrays that result in planar virtual array configurations are explained below.

7.2.1 Linear transmit and receive array with orthogonal axis

Unlike phased-array radars, a planar virtual array configuration for MIMO radars can be achieved with a linear transmit and linear receive array. However, the two arrays are required to be either placed along orthogonal axes or are non-colinear. This is possible because of the inherent property of MIMO radars, as explained in Section 5.2, which states that the virtual array element positions are all the possible combinations of the positions of the transmit and receive array elements. Therefore, if the transmit and receive arrays are oriented along orthogonal axes, then the resulting virtual array is a planar array. This scenario gives rise to three cases of transmit and receive array orthogonal configurations, namely L, X and T configuration as shown in Fig. 7.1.

In Fig. 7.1, the three orthogonal transmit and receive array configurations are shown on the left-hand side and their corresponding virtual array configurations are shown on the right-hand side. For each case, there are 10 transmit array elements and 10 receive array elements and thus according to equation (5.4), 100 virtual array elements are obtained. It can be seen that L and T configuration results in a planar virtual array with the same aperture size thus, for the virtual array pattern is the same and is shown in Fig. 7.2 (left), in $u - v$ space. The virtual array pattern for the X configuration is shown in Fig. 7.2 (right). Thus, it shows that for a total of 20 physical elements, the MIMO radar can achieve an angular resolution corresponding to that of 100 elements. This is the most promising aspect of MIMO radars as compared to phased-array radars.

7.2.2 Planar transmit and receive array

In order to achieve a planar configuration for a virtual array in MIMO radars, it is also possible to have traditional planar transmit and receive array configurations, similar to phased-array radar. The three cases of such a placement are individually discussed and then compared in this section. Note that these three cases are the same as the three cases explained in Section 5.2, but for the planar case instead of the linear case.

Dense/dense transmit/receive configurations

In this case, both the transmit and receive array are dense with $\lambda_0/2$ spacing in the x and y directions. The corresponding virtual array is also dense, but with redundant elements. In Fig. 7.3, the dense configuration of a 4×4 transmit and 4×4 receive arrays (both 16 elements each) and corresponding virtual array configuration of 16×16 (256) elements are shown. Not all the virtual array elements are shown in the figure because of the redundancy in the element positions. The corresponding virtual array

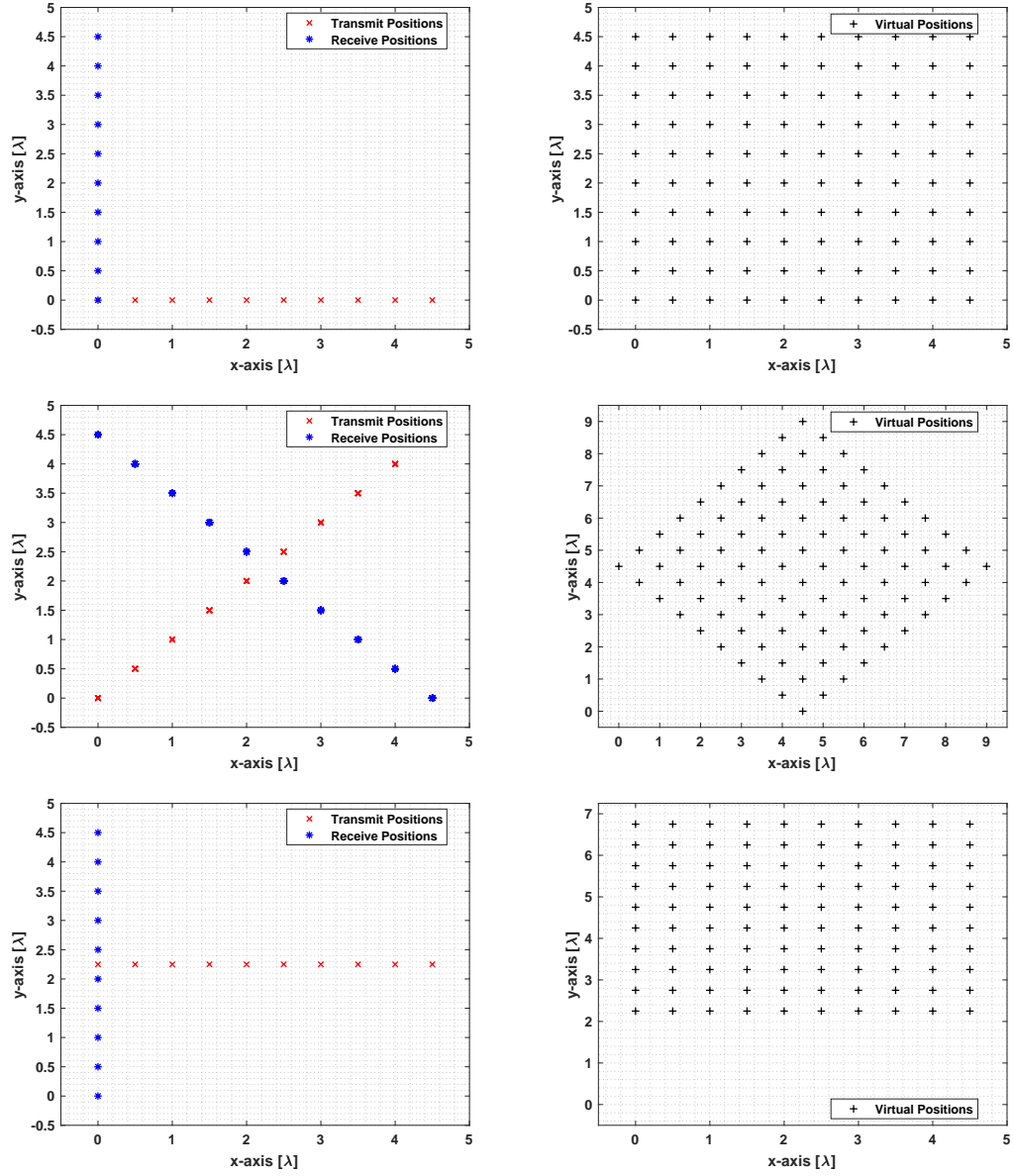


Figure 7.1: L, X, and T configurations for transmit and receive array (left) and the corresponding virtual array configurations on the right.

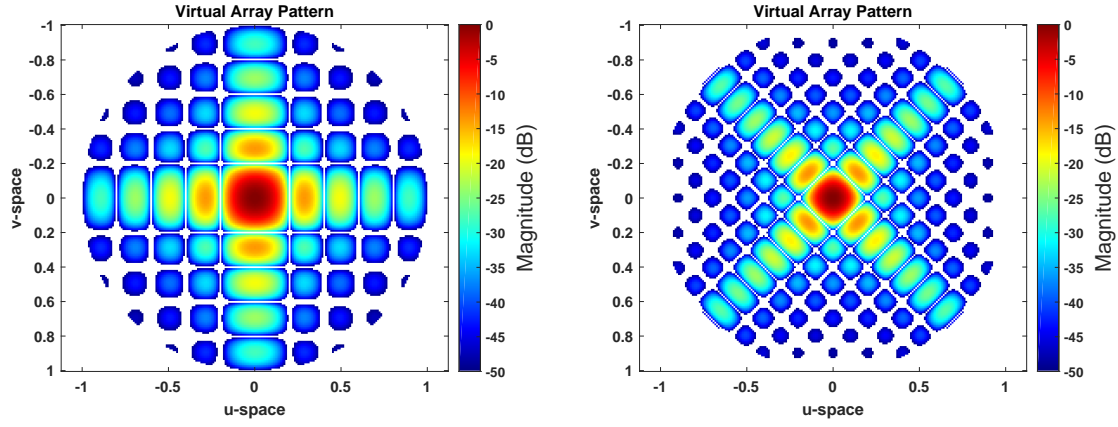


Figure 7.2: 2D virtual array pattern for L and T configurations (left) and X configuration (right) from Fig. 7.1

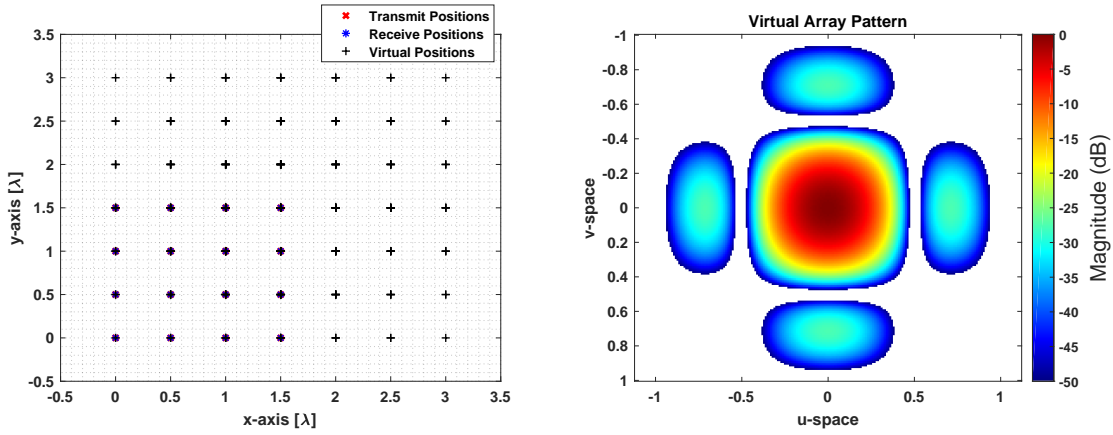


Figure 7.3: Dense/dense transmit/receive configurations (left) and corresponding virtual array configuration and 2D virtual array pattern (right).

pattern is also shown in Fig. 7.3 (right) and it can be seen that even though the number of physical elements is more than that in Fig. 7.1, the angular resolution is much lower than the one in Fig. 7.2. Therefore, this case is certainly not the optimal one for MIMO radars since it does not take advantage of the full potential of the virtual array in terms of angular resolution.

Sparse/dense transmit/receive configurations

This case is equivalent to the conventional case as in Section 5.2. The transmit array is sparse, while the receive array is dense with $\lambda_0/2$ spacing in x and y directions. The corresponding virtual array is now dense without redundant elements. In Fig. 7.4, the sparse configuration of the 4×4 transmit and dense configuration of the 4×4 receive

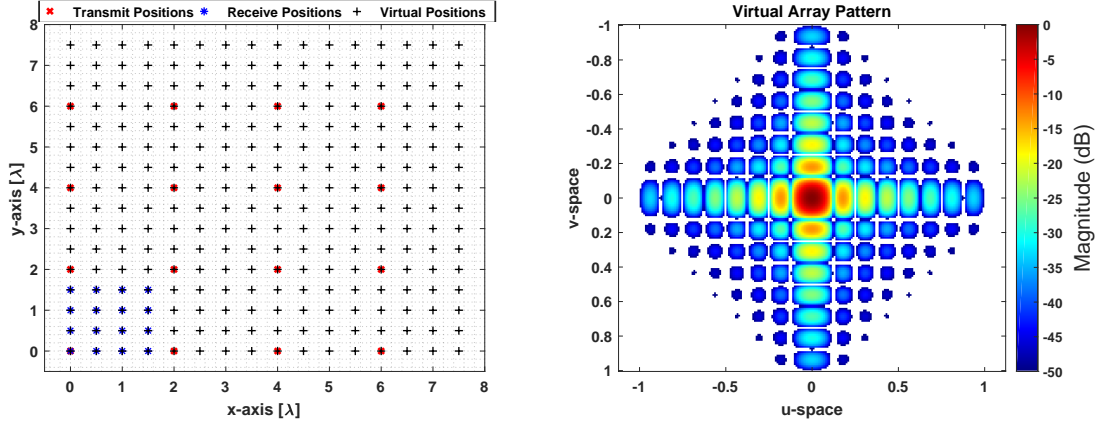


Figure 7.4: Sparse/dense transmit/receive configurations and corresponding virtual array configuration (left) and 2D virtual array pattern (right).

array (both 16 elements each) and corresponding virtual array configuration of 16×16 (256) elements is shown. In this case, the virtual array elements are all shown in the figure because each element now has a unique position. The corresponding virtual array pattern is also shown in Fig. 7.4 (right) and it can be seen that the angular resolution is considerably higher than in the previous case of dense/dense transmit and receive configuration. Thus, this case is certainly a more suitable one for MIMO radars since it takes advantage of the virtual array concept.

It is now important to mention a drawback of this case and that is that it needs a larger physical space for implementation in imaging radars. Note that in Fig. 7.4, since the transmit array is sparse and also a physical array, the resulting size of the array is larger than that of a dense array, which means a $6\lambda_0 \times 6\lambda_0$ physical size of the array is required. This is a concern because of two reasons. One is that most of the imaging radar applications are space limited and, secondly, an implementation of such an array with RF ICs implies long transmission paths from IC to radar antennas, which results in significant transmission losses.

Sparse/sparse transmit/receive configurations

The third case that can be considered is a compromise between the previous two cases and it is the case where both transmit and receive array are sparse. To show this, the virtual array synthesis method explained in Section 5.3.3 is used but now for the planar case. Note that the linear array formulation in Chapter 5 is extended to planar array by extending the array factor to include the phase terms in the ϕ direction in addition to the θ direction, see [20]. The transmit array is obtained from the TSP method and the sparse planar configuration of the 14 transmit elements is shown in Fig. 7.5. The

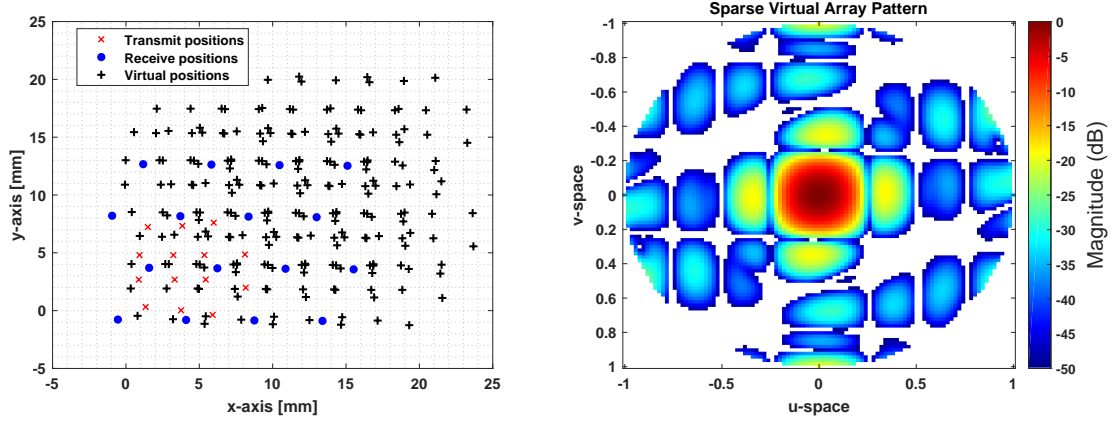


Figure 7.5: Sparse/sparse transmit/receive configurations and corresponding sparse virtual array configuration (left) and 2D virtual array pattern (right).

Table 7.1: Comparison of beamwidth, side lobe level and system size of the virtual array for the three investigated cases for transmit/receive configurations.

Case	Beamwidth (u, v)	SLL	System size
Dense/Dense TX/RX	$\pm 0.16, \pm 0.16$	-27dB	$3\lambda_0/2 \times 3\lambda_0/2$
Sparse/Dense TX/RX	$\pm 0.05, \pm 0.05$	-13.43dB	$7.5\lambda_0/2 \times 7.5\lambda_0/2$
Sparse/Sparse TX/RX	$\pm 0.1, \pm 0.1$	-18.72dB	$5\lambda_0/2 \times 5\lambda_0/2$

sparse receive array of 16 elements is obtained from the method of least squares and is also shown in Fig. 7.5 along with the corresponding sparse virtual configuration and 2D virtual array pattern (right).

From the comparison between Fig. 7.5, Fig. 7.3 and Fig. 7.4, it can be seen that the beamwidth and side lobe level of the sparse virtual array pattern is a compromise between the first two cases. The comparison of beamwidth, side lobe level and system size of the virtual array for the three cases is shown in Table 7.1. Thus, the sparse topology advantage is three-fold. The size of the physical system can be maintained at an acceptable level while a smaller beamwidth and lower side lobe level can be achieved in two dimensions.

7.3 Discussion on the pros and cons

After having discussed the two categories of transmit and receive array configurations that result in a planar virtual array configuration, the pros and cons of the two categories are discussed here. First, the category where transmit and receive arrays are linear has an advantage of taking full benefit of the MIMO radar concept and even though the

physical arrays are linear, the virtual array results in a planar configuration and the system has 2D patterns. Another advantage is the implementation, since the feed network of a linear array has fewer challenges as compared to a feed network of a planar array. The drawback of this category is that high side lobe levels occur and for a large number of transmit and receive elements, the linear topology can lead to a large system.

Second, the category where both transmit and receive arrays are planar has an advantage of a confined system, since a large number of elements can be more closely placed in the 2D plane. However, as explained earlier, this can be a drawback in case of conventional array design, but it can be improved with the help of a sparse array configuration. The drawback of this category is in terms of implementation of these arrays since planar arrays require a more complex feeding system. Also, the effects of mutual coupling between the elements are stronger in the planar case, because each element has more neighbors.

7.4 Conclusion

For 3D radar imaging systems, planar arrays are needed to perform a complete three dimensional image of the environment. In case of MIMO radars, there are two categories of transmit and receive array configurations, which can achieve a planar virtual array configuration. In the first category both transmit and receive arrays are linear and are oriented along orthogonal axis or non-collinear. Three configurations of this category are explained and compared. In the second category both transmit and receive arrays are planar and the resulting virtual array configuration is also planar. Three cases of dense/dense, sparse/dense and sparse/sparse transmit/receive configurations have been presented and the virtual array patterns have been compared. Through simulations, it is shown that with a sparse transmit and sparse receive array, an improvement in beamwidth and side lobe level in the virtual array patterns for MIMO radars can be achieved.

CHAPTER EIGHT

Conclusion and recommendations

8.1 Conclusions

The mobile world of tomorrow holds the vision of self-driving cars to provide safely and comfort to its customer. This will only be possible with the advancement of radar imaging technology, which is finding its new potential in the mm-wave frequency regime. The MIMO radar concept that was put forward in the early 2000s is now becoming main stream for many of these radar imaging platforms. This thesis focused on the challenges encountered by researchers around the two main aspects of MIMO radar imaging systems, one is the design and implementation of a MIMO radar demonstrator at these mm-wave frequencies and the other the improvement in the angular resolution of these imaging systems through the concept of sparse array topologies.

First, the design and evaluation of a complete FMCW-MIMO radar demonstrator was presented, which consisted of a linear array of 13 single-chip radars, each with one transmitter and two receivers. The system architecture of the platform with explanation of the functionality of the MIMO radar in TDM mode was presented. It was shown that the non-regular MIMO arrays can be used to achieve the resolution of a sparse SIMO array and the dynamic range of a dense array. The experimental evaluation of the designed platform brought up two main issues; one is that in a TDM scenario the SNR of the received signal is lower than 20 dB for the radar chips that are silent and thus the phase errors at the target locations are significantly high. Second, it was shown that there is no synchronization between the radar chips when fully configured. Therefore, accurate phase-synchronisation of the transmitted signals is a

stringent requirement for such systems to work.

From the analysis of the sparse array configuration of the designed MIMO radar platform in Chapter 3, it became interesting to further explore the option of sparse array synthesis, as it showed potential of better performance as compared to a dense array. In this work, the idea of sparse array design was explored first in radio astronomy and subsequently applied in MIMO radar imaging systems. In case of radio astronomy, the case study of connected Vivaldi aperture arrays was selected and two concepts of regular and irregular on-grid sparse array configuration were proposed, with the aim to reduce the number of active elements while achieving the required system performance. It was shown that the regular sparse array configuration can be used to achieve higher sensitivity at lower frequencies if the impact of grating lobes can be mitigated. Also, actual termination of the inactive antenna elements in case of sparse configurations was addressed and it was concluded from the results that three termination options, i.e $50\ \Omega$, $0\ \Omega$ for short and $\infty\ \Omega$ for open, do not have a significant effect on the active reflection coefficient and antenna noise temperature. In short, for radio-astronomical observations where the option of digitizing at element level is the most suitable option, yet is not cost effective in case of a dense array arrangement, sparse array configurations are a viable option for connected aperture arrays.

In case of MIMO radar imaging systems, two methods for the synthesis of sparse virtual arrays have been proposed, formulated and illustrated with numerical examples. Both methods use a Two-step Synthesis Procedure (TSP) for antenna array sparsity and determine the topology of the sparse transmit and receive array, which results in a sparse virtual array design. The first method determines the transmit and receive array positions independently for the two arrays, while the second method determines the sparse receive array positions depending on the transmit array element positions. With the help of these numerical methods, it was shown that if the arrays are synthesized with the main beam at the maximum scan angle, no grating lobes appear while scanning over the whole FOV. Further, it was shown that a sparse virtual array can achieve a better performance in terms of beamwidth and side lobe level, as compared to the equivalent dense virtual array. An improvement of a maximum of 3° in beamwidth and a maximum of 7 dB side lobe level is reported in the examples. Furthermore, in the presented formulations of the synthesis methods, physical limitations on the maximum size of the arrays and minimum element spacing can be included, which allows for these methods to be used in a wide variety of applications.

In the next part of this thesis, the challenge of characterizing the virtual array pattern without the need to design of a complete radar platform was addressed. For this purpose, a measurement strategy using only a two-port VNA and emulating the TDM MIMO mode of a MIMO radar has been formulated. It has validated experimentally,

for the characterization of the radiation pattern, the side lobe level and the beamwidth of the synthesized virtual array for a MIMO radar, under scanning conditions. It has been shown with the help of a test case consisting of three transmit and four receive OWAs, that the proposed measurement strategy allows to recreate the virtual array pattern and the measured results are in good agreement with the simulated virtual array patterns.

Finally, for a planar virtual array, different transmit and receive array configurations were considered. Three cases of dense/dense, sparse/dense and sparse/sparse transmit/receive configurations were presented and the virtual array patterns were compared. Through simulations, it was shown that with a sparse transmit and sparse receive array, an improvement in beamwidth and side lobe level in the virtual array patterns for MIMO radars can be achieved.

8.2 Recommendations

Based on the conclusions of this thesis, a few recommendations can be made. Regarding the design of the 60 GHz demonstrator, it is recommended to evaluate the integration effects of the RF components involved in the system architecture. Even though a radar chip that has a complete RF front end and antenna on-chip can work well as a stand-alone device, putting it in close proximity to other radar chips and baseband components such as a DDS and ADCs, its performance can deteriorate. For example, in case of the TDM MIMO mode evaluation of the board it was observed that when the transmitter of the radar chip was silent, the received signal at the receiver of the same chip was relative more noisy as compared to the one whose transmitter was on. This suggests that during the design of such chips the noise figure of the receivers must be improved for the case when there is no transmit and receive correlation. Also, in case of the transmit signal output, it has been observed that PLL control for a stable output signal is a crucial aspect of integration.

Furthermore, when synthesising sparse virtual arrays, following the methods of Chapter 5, it is advised to include the gain of the array into the constraints while synthesizing sparse arrays for MIMO radar, as the gain of an array also depends on the distance between the array elements and it strongly affects the signal-to-noise ratio of these kinds of systems. Also, the co-design strategy for sparse arrays that includes the mutual coupling between antenna elements is a technical challenge that needs to be further researched.

On a broader level, the design of a next generation mm-wave MIMO radar for autonomous driving needs to include a 4D imaging radar, i.e. including velocity, with a

sparse topology of both transmit and receive arrays using the methods proposed in this thesis. Also, it requires technologically advanced RF and base-band integrated circuits that are optimized for MIMO radar functionality and careful integration of these circuits with the antenna part.

APPENDIX A

Transmit phase synchronization analysis

The extended experimental results regarding the phase synchronization of the MIMO radar prototype designed and presented in Chapter 3 are listed and explained in detail. In Section 3.5.2, we showed that the phase error at the received signal could be very high because of low SNR at the silent chips, which results in high phase errors when using range profiles. Therefore, determining the phase synchronization at baseband among all the chips is not possible. For further evaluation of the demonstrator, we perform over the air measurements with a spectrum analyzer and a standard horn antenna, to determine the phase synchronization of the transmitted signal.

The idea here is to determine the synchronization of the phases of the transmitted signals from each radar chip using over-the-air measurements in the anechoic chamber. This is possible with this demonstrator because the whole front-end is configurable. When all the chips are active and transmitting and all the DDSs are set to phase 0, then by measuring the radiation pattern of the transmit array, a directive pattern should be obtained with the maximum at broad side (remember that here we are only talking about transmission at a single frequency). This is true only in the case the transmitted signals from each chip have the same phase and do not vary over time.

In the following experiments, we first measure the absolute transmit output power from all the chips individually and then measure the radiation pattern of the array over an angular range of $\pm 90^\circ$. For this purpose, the measurement setup is used in the anechoic chamber of the Antenna lab of Eindhoven University of Technology. The over-the-air measurement setup is shown in Fig. A.1. The test antenna used for measuring

the transmit output power is a standard horn antenna at 60 GHz with 20 dBi gain and the spectrum analyzer is from Keysight technologies, model number N9030A with M1970V extender. The demonstrator has been placed on a scanner that can rotate over 360° . Both the demonstrator and the spectrum analyzers were controlled using Matlab.

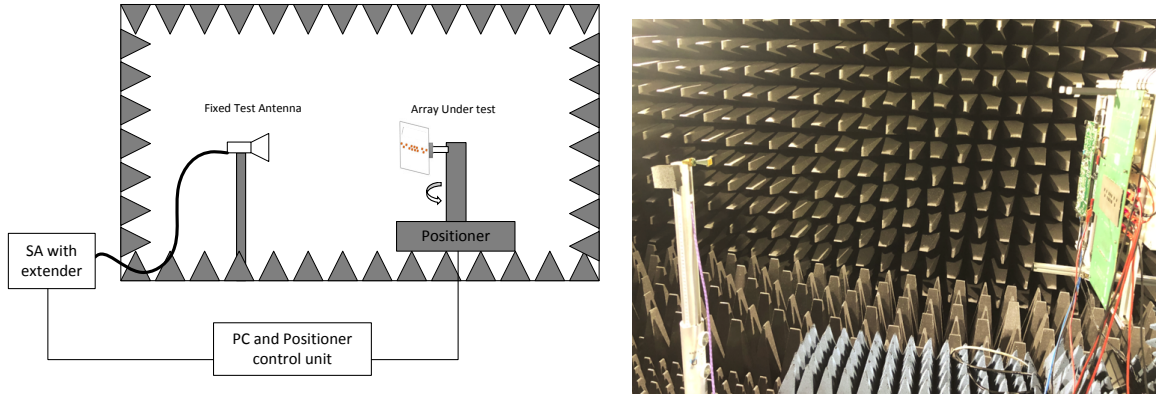


Figure A.1: Left: Impression of the measurement setup for the transmit phase error of the demonstrator in anechoic chamber. Right: over the air measurement setup for the transmit phase error of the demonstrator in an anechoic chamber.

We first take the middle three chips, i.e. 0, 2 and 8 from Fig. 3.4, and measure the radiated transmit power at a distance of 1 m using the measurement setup explained above. The three chips are configured in such a way that at first the DDS of each chip is turned off and next the DDS of each chip is turned on. When the DDS is off, it means that the radar chip is running freely (the VCO of radar chip is free running) and there is no signal to the PLL to lock it. Thus the radar chip transmits a single tone at around 56 GHz, which is the lowest possible frequency for the lowest voltage of the VCO. When the DDS is on, it is set to one single frequency, such as 24 MHz with phase 0, which is applied as a reference clock to the PLL and then the PLL is locked in the radar chip and the output frequency of the transmitted signal is 57.6 GHz. The measured transmit output power levels using the spectrum analyzer for the three chips is shown in Fig. A.2.

In Fig. A.2, on the top left, the graph shows the transmit power level of chip 0, when the DDS is not configured, which means that there is no reference signal at the input of the on-chip crystal oscillator. It can be seen that the transmitted signal is at 56.85 GHz, as expected. On the top right, the graph shows the power level of chip 0 with DDS configured (at 24 MHz), thus the output frequency is 57.6 GHz. It can be seen that the PLL is locked to the DDS and gives the output sinusoidal signal at the single frequency of 57.6 GHz. However, the signal is not clean and includes a number of spurs around the frequency of interest. Also, during the experiments on the spectrum analyzer, it has

been observed from the output signal in case the DDS is configured, that the frequency of the maximum peak is not exactly 57.6 GHz and varies over ± 0.2 MHz. The most probable reason for this is that PLL is not properly locked, and the frequency of the output transmit signal is not stable over time. Also note that the same behavior has been observed at 60 GHz and 64 GHz.

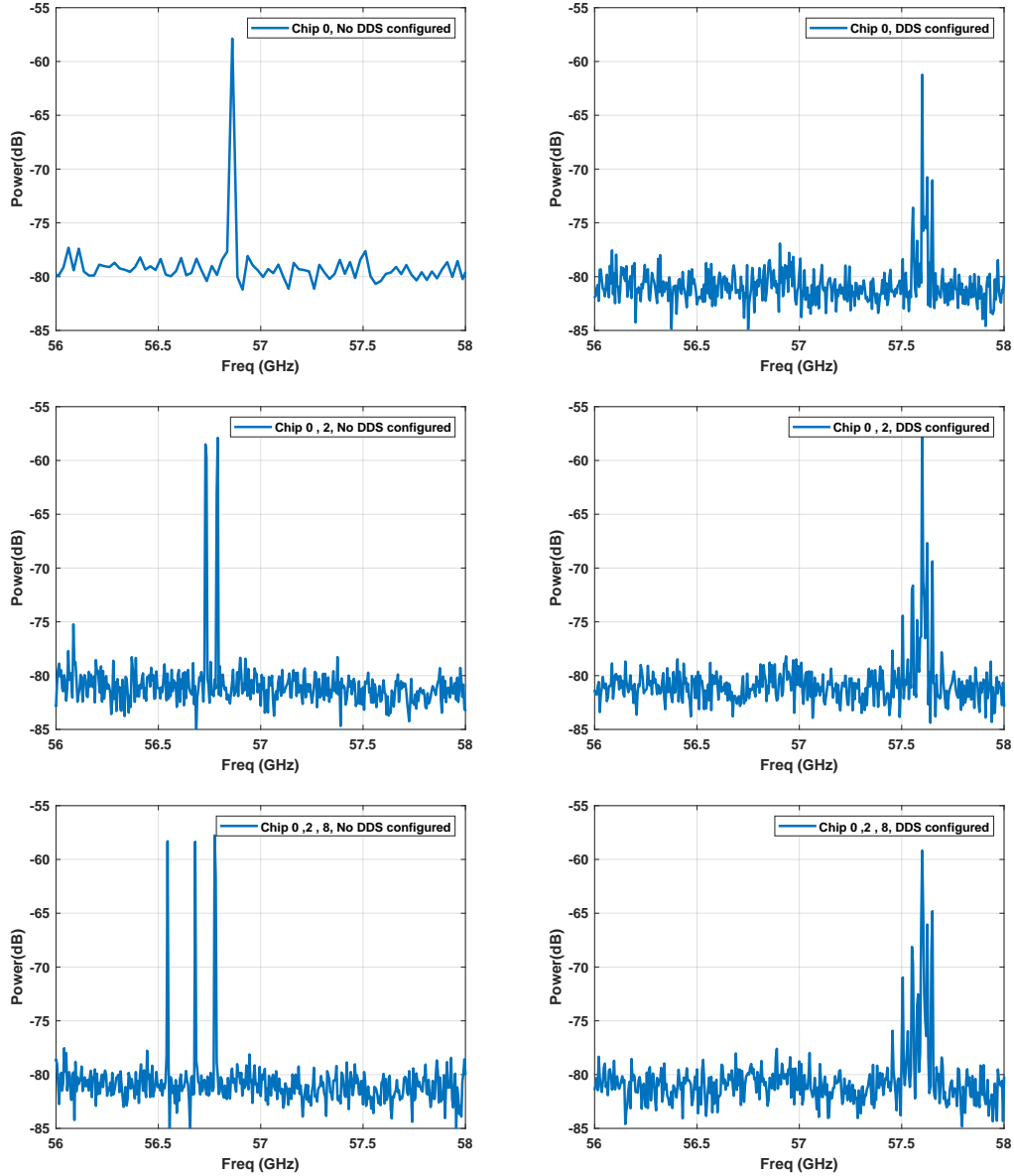


Figure A.2: Measured transmit power levels versus frequency, without DDS configure (left) and with DDS configured (right), for chip 0 (top), chip 0 and 2 (middle), and for chip 0, 2, and 8 (bottom). Note that the different detail in the noise floor of the first plot (top-left) is due to a different sweep time in that measurement.

Further, in Fig. A.2, on the middle left, the graph shows the power level of chips 0 and 2 when simultaneously transmitting, when the DDS is not configured, while on the middle right, the graph shows the power level of the chips with DDS configured (at 24 MHz). Again note that the level and number of the spurs has increased, but now the signal power increases at 57.6 GHz, which suggests constructive interference at broadside, as expected. Furthermore, in Fig. A.2, on the bottom left, the graph shows the power level of chips 0, 2 and 8 when simultaneously transmitting, when DDS is not configured, while on the bottom right, the graph shows the power level of the chips with DDS configured (at 24 MHz). The spurs have increased, but the signal power decreases at 57.6 GHz, which suggests that there is no constructive interference at broadside anymore, and instead of power being add-up because of more elements, the power is reduced at the frequency of interest. This is unexpected since three chips are transmitting at the same time and the transmitted power should add up. It can be concluded that since the collective maximum transmit output power at 57.6 GHz is not accumulative, the three transmitted signals are not phase synchronized.

It is important to mention here that the same trend has been observed in these measurements at higher frequencies (60 GHz and 64 GHz), and with more chip combinations. For example, in Fig. A.3, this is shown in a close-up comparison of the transmit signal power when three chips are configured simultaneously (in red) and when five chips are configured simultaneously (blue). It can be seen that in the case of five chips, the frequency is shifted and the maximum transmit power is 6 dB lower than in the three-chips case. The reason for this measured behaviour of the transmitting chips is that the output signal power has been distributed among the large number of spurs at frequencies around 56.6 GHz. These spurs are approximately at the interval of 24 MHz which suggest that these spurs can be explained with the phenomenon of reference breakthrough. The shift in the frequency suggests that at least one of the PLLs of the transmitting chips is not locked to the reference frequency. It can be argued that the DDS (providing the reference signal to the PLLs) can also be out of sync, but during separate experiments the DDS outputs on the board were measured with an oscilloscope and it turned out that up to the radar chip LO input, all the signals were synchronized and had the same phase. Therefore, it can be concluded that the transmitted signal from all the transmitters do not have the same phase and do not add up coherently so as to give a higher power at the transmitted frequency.

In previous measurements, the transmitted signal was measured by a standard horn antenna in the broadside direction of the radar platform. It can be argued that the maximum of the coherent summation of the transmitted signals from either the three-chip or the five-chip combination can be at an angle other than broadside (i.e. $\theta = 0^\circ$). For that purpose, we measured the transmit power of Fig. A.3, over an angular range. We measured the radiation patterns in the $\phi = 0^\circ$ plane and for θ between $\pm 90^\circ$, to

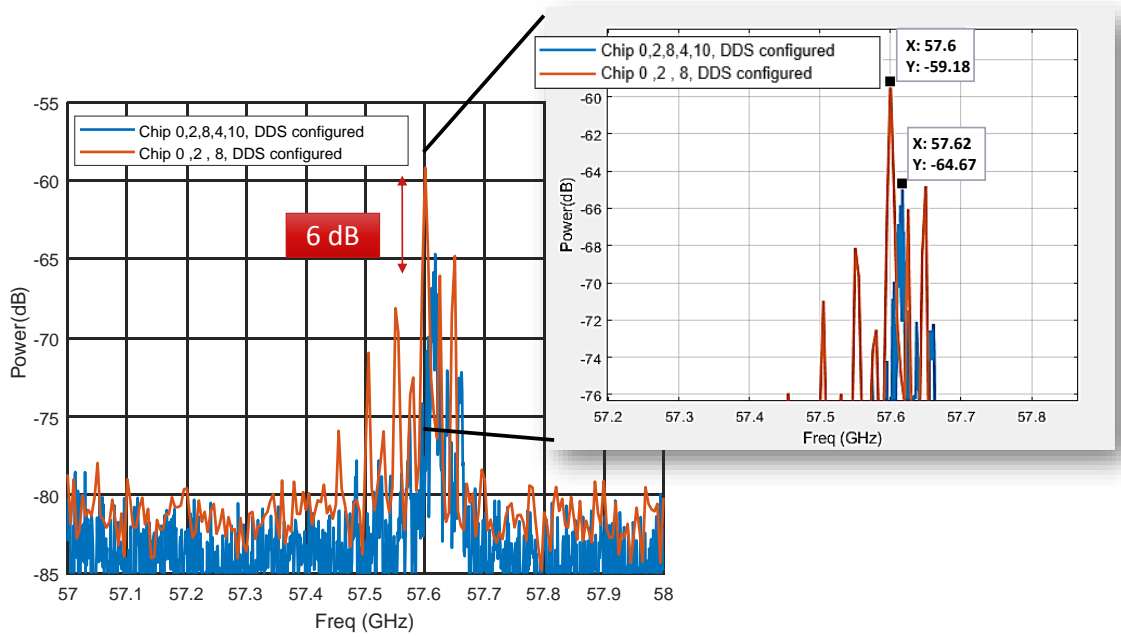


Figure A.3: Comparison of the measured transmit signal power when three chips are configured simultaneously (in red) and when five chips are configured simultaneously (blue) in the broadside direction. Inset: close-up.

determine if there is directivity in the pattern. In Fig. A.4, the absolute power (in dBm) over the angles for the three-chips and five-chips case from Fig. A.3 is shown. It can be seen that the pattern is not directive for either case and also the overall power has been reduced for the case of five chips. The non-directivity of the radiation pattern suggests that the PLLs of the chips are not synchronized and that the phase is not locked to the same value. Also the lower power value is consistent with Fig. A.3, which is due to the spurs in the transmitted signal. Fig A.5 also shows the normalized power for three different cases. These experiments confirm that transmitters are not synchronized and they transmit the signal with random phases (which are time variant) and therefore the radiation patterns are quasi omni-directional.

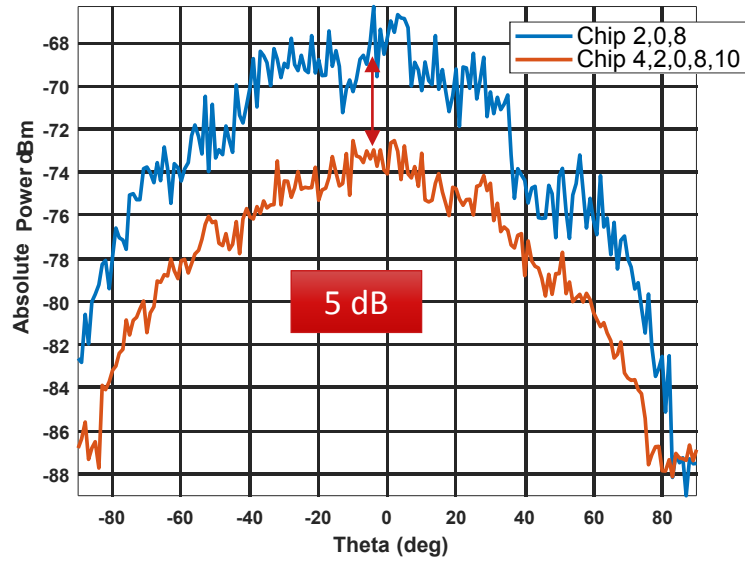


Figure A.4: The absolute transmitted power (in dBm) versus angle for the three-chips (blue) and five-chips (red) cases from Fig. A.3.

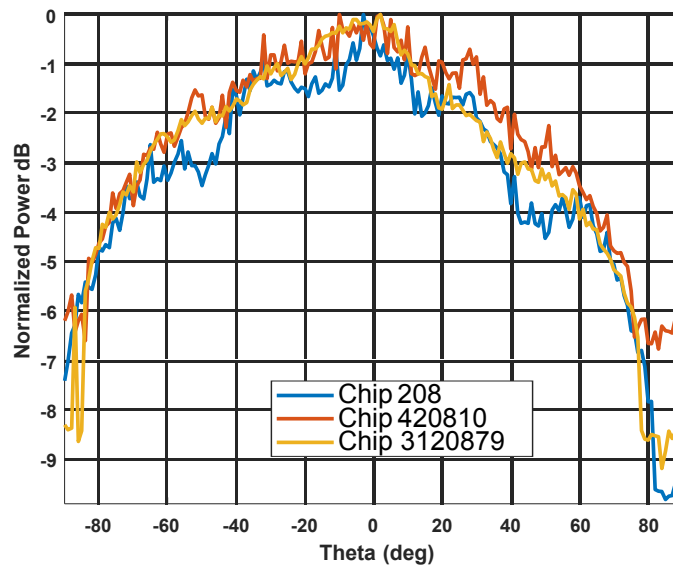


Figure A.5: Normalized radiation pattern for three different combinations of transmitter configurations.

Bibliography

- [1] (2020) This was supposed to be the year driverless cars went mainstream. The New York Times: Technology. [Online]. Available: <https://www.nytimes.com/2020/05/12/technology/self-driving-cars-coronavirus.html>
- [2] (2021) 'peak hype': why the driverless car revolution has stalled. The Guardian. [Online]. Available: <https://www.theguardian.com/technology/2021/jan/03/>
- [3] (2020) Despite setbacks, coronavirus could hasten the adoption of autonomous vehicles and delivery robots. VentureBeat. [Online]. Available: <https://venturebeat.com/2020/03/20/>
- [4] A. Severino, S. Curto, S. Barberi, F. Arena, and G. Pau, "Autonomous vehicles: An analysis both on their distinctiveness and the potential impact on urban transport systems," *Applied Sciences*, vol. 11, no. 8, 2021. [Online]. Available: <https://www.mdpi.com/2076-3417/11/8/3604>
- [5] "From driver assistance systems to automated driving," VDA Automation Magazine, Verband der Automobilindustrie, 2015.
- [6] (2021) Cars with autopilot in 2021. Auto pilot review. [Online]. Available: <https://www.autopilotreview.com/cars-with-autopilot-self-driving/>
- [7] D. J. Yeong, G. Velasco-Hernandez, J. Barry, and J. Walsh, "Sensor and sensor fusion technology in autonomous vehicles: A review," *Sensors*, vol. 21, no. 6, 2021. [Online]. Available: <https://www.mdpi.com/1424-8220/21/6/2140>
- [8] T. Zhou, M. Yang, K. Jiang, H. Wong, and D. Yang, "Mmw radar-based technologies in autonomous driving: A review," *Sensors*, vol. 20, no. 24, 2020. [Online]. Available: <https://www.mdpi.com/1424-8220/20/24/7283>
- [9] X. Zhuge and A. G. Yarovoy, "A sparse aperture MIMO-SAR-based UWB imaging system for concealed weapon detection," *Geoscience and Remote Sensing, IEEE Transactions on*, vol. 49, pp. 509 – 518, 02 2011.

- [10] M. Harter, T. Schipper, L. Zwirello, A. Ziroff, and T. Zwick, "24ghz digital beam-forming radar with t-shaped antenna array for three-dimensional object detection," *International Journal of Microwave and Wireless Technologies*, vol. 4, no. 3, p. 327–334, 2012.
- [11] B. B. Adela, P. T. M. van Zeijl, U. Johannsen, and A. B. Smolders, "On-chip antenna integration for millimeter-wave single-chip FMCW radar, providing high efficiency and isolation," *IEEE Transactions on Antennas and Propagation*, vol. 64, no. 8, pp. 3281–3291, Aug 2016.
- [12] R. Feger, C. Wagner, S. Schuster, S. Scheiblhofer, H. Jager, and A. Stelzer, "A 77-GHz FMCW MIMO radar based on an SiGe single-chip transceiver," *IEEE Transactions on Microwave Theory and Techniques*, vol. 57, no. 5, pp. 1020–1035, May 2009.
- [13] Unleash the full 5g capacity with mmwave. Qualcomm. [Online]. Available: <https://www.qualcomm.com/research/5g/5g-nr/mmwave>
- [14] Ieee distinguished microwave lecture: Automotive radar - a signal processing perspective on current technology and future systems. InnoSent. [Online]. Available: <https://markus.gardill.net/talk/dml/>
- [15] D. Bliss and K. Forsythe, "Multiple-input multiple-output (MIMO) radar and imaging: degrees of freedom and resolution," in *The Thrity-Seventh Asilomar Conference on Signals, Systems Computers, 2003*, vol. 1, 2003, pp. 54–59 Vol.1.
- [16] E. Brookner, "MIMO radar demystified and where it makes sense to use," in *2014 International Radar Conference*, 2014, pp. 1–6.
- [17] J. Wood, "A radar history of world war II: technical and military imperatives [book reviews]," *IEE Review*, vol. 47, no. 4, pp. 29–29, 2001.
- [18] M. I. Skolnik, *Introduction to Radar Systems /2nd Edition/*, 2nd ed. New York: McGraw Hill Book Co., 1980.
- [19] R. Hansen, *Phased Array Antennas*, ser. Wiley Series in Microwave and Optical Engineering. Wiley, 1998. [Online]. Available: <https://books.google.nl/books?id=HaK6QgAACAAJ>
- [20] C. A. Balanis, *Antenna Theory: Analysis and Design*, ser. Wiley-Interscience, USA. Wiley, 2005.
- [21] W.-D. Wirth, *Radar Techniques Using Array Antennas*, ser. Radar, Sonar and Navigation. Institution of Engineering and Technology, 2013. [Online]. Available: <https://digital-library.theiet.org/content/books/ra/pbra026e>

- [22] H. J. Visser, *Array and Phased Array Antenna Basics*. John Wiley and Sons, Ltd, 2005. [Online]. Available: <https://onlinelibrary.wiley.com/doi/abs/10.1002/0470871199.ch7>
- [23] R. Feger, S. Schuster, S. Scheiblhofer, and A. Stelzer, "Sparse antenna array design and combined range and angle estimation for fmcw radar sensors," in *2008 IEEE Radar Conference*, 2008, pp. 1–6.
- [24] M. Q. Nguyen, R. Feger, J. Bechter, M. Pichler-Scheder, and A. Stelzer, "A fast-chirp MIMO radar system using beat frequency FDMA with single-sideband modulation," in *2020 IEEE/MTT-S International Microwave Symposium (IMS)*, 2020, pp. 1015–1018.
- [25] H. Haderer, R. Feger, C. Pfeffer, and A. Stelzer, "Millimeter-wave phase-coded CW MIMO radar using zero- and low-correlation-zone sequence sets," *IEEE Transactions on Microwave Theory and Techniques*, vol. 64, no. 12, pp. 4312–4323, 2016.
- [26] M. Q. Nguyen, R. Feger, J. Bechter, M. Pichler-Scheder, M. H. Hahn, and A. Stelzer, "Fast-chirp FDMA MIMO radar system using range-division multiple-access and doppler-division multiple-access," *IEEE Transactions on Microwave Theory and Techniques*, vol. 69, no. 1, pp. 1136–1148, 2021.
- [27] B. R. Mahafza, *Radar Systems Analysis and Design Using MATLAB*. USA: CRC Press, Inc., 2000.
- [28] R. B. Mahafza, *Radar Systems Analysis and Design Using MATLAB*, 1st ed. Boca Raton, FL, USA: CRC Press, Inc., 2000.
- [29] G. Hislop and C. Craeye, "On the mathematical link between the music algorithm and interferometric imaging," *IEEE Transactions on Antennas and Propagation*, vol. 59, no. 4, pp. 1412–1414, 2011.
- [30] R. Z. Syeda, *MIRACLE-MIMO Integrated Radar with wide-scan on-chip Antennas and Co-Location Efficiency*, pdeng-thesis ed. Eindhoven University of Technology, 2017.
- [31] D. G. Manolakis, V. K. Ingle, and S. M. Kogon, *Statistical and adaptive signal processing: Spectral estimation, signal modeling, adaptive filtering, and array processing.*, ser. Artech House signal processing library. Boston ; London : Artech House, 2005.
- [32] H. Lebrete and S. Boyd, "Antenna array pattern synthesis via convex optimization," *IEEE Transactions on Signal Processing*, vol. 45, no. 3, pp. 526–532, 1997.

- [33] O. M. Bucci, M. D'Urso, T. Isernia, P. Angeletti, and G. Toso, "Deterministic synthesis of uniform amplitude sparse arrays via new density taper techniques," *IEEE Transactions on Antennas and Propagation*, vol. 58, no. 6, pp. 1949–1958, 2010.
- [34] D. Caratelli and M. C. Viganó, "Analytical synthesis technique for linear uniform-amplitude sparse arrays," *Radio Science*, vol. 46, no. 04, pp. 1–6, 2011.
- [35] T. Clavier, N. Razavi-Ghods, F. Glineur, D. González-Ovejero, E. de Lera Acedo, C. Craeye, and P. Alexander, "A global-local synthesis approach for large non-regular arrays," *IEEE Transactions on Antennas and Propagation*, vol. 62, no. 4, pp. 1596–1606, 2014.
- [36] A. B. Smolders, S. J. Geluk, and A. C. F. Reniers, "Circularly polarized sparse arrays realized by randomly rotated linearly polarized antennas," *IEEE Antennas and Wireless Propagation Letters*, vol. 16, pp. 736–739, 2017.
- [37] B. Fuchs, "Antenna selection for array synthesis problems," *IEEE Antennas and Wireless Propagation Letters*, vol. 16, pp. 868–871, 2017.
- [38] B. Fuchs and J. J. Fuchs, "Optimal narrow beam low sidelobe synthesis for arbitrary arrays," *IEEE Transactions on Antennas and Propagation*, vol. 58, no. 6, pp. 2130–2135, 2010.
- [39] B. Fuchs, A. Skrivervik, and J. R. Mosig, "Synthesis of uniform amplitude focused beam arrays," *IEEE Antennas and Wireless Propagation Letters*, vol. 11, pp. 1178–1181, 2012.
- [40] G. Prisco and M. D'Urso, "Maximally sparse arrays via sequential convex optimizations," *IEEE Antennas and Wireless Propag. Lett*, vol. 11, no. 1, pp. 192–195, 2012.
- [41] S. E. Nai, W. Ser, Z. L. Yu, and H. Chen, "Beampattern synthesis for linear and planar arrays with antenna selection by convex optimization," *IEEE Transactions on Antennas and Propagation*, vol. 58, no. 12, pp. 3923–3930, 2010.
- [42] J. Helander, D. Tayli, and D. Sjöberg, "Synthesis of large endfire antenna arrays using convex optimization," *IEEE Transactions on Antennas and Propagation*, vol. 66, no. 2, pp. 712–720, 2018.
- [43] H. V. Bui, S. N. Jha, and C. Craeye, "Fast full-wave synthesis of printed antenna arrays including mutual coupling," *IEEE Transactions on Antennas and Propagation*, vol. 64, no. 12, pp. 5163–5171, 2016.

- [44] E. Fishler, A. Haimovich, R. Blum, D. Chizhik, L. Cimini, and R. Valenzuela, “MIMO radar: an idea whose time has come,” in *Proceedings of the 2004 IEEE Radar Conference (IEEE Cat. No.04CH37509)*, 2004, pp. 71–78.
- [45] X. Zhuge and A. G. Yarovoy, “Three-dimensional near-field MIMO array imaging using range migration techniques,” *IEEE Transactions on Image Processing*, vol. 21, no. 6, pp. 3026–3033, 2012.
- [46] M. Harter, T. Mahler, T. Schipper, A. Ziroff, and T. Zwick, “2-d antenna array geometries for MIMO radar imaging by digital beamforming,” in *2013 European Radar Conference*, 2013, pp. 383–386.
- [47] M. Harter, A. Ziroff, and T. Zwick, “Three-dimensional radar imaging by digital beamforming,” in *2011 8th European Radar Conference*, 2011, pp. 17–20.
- [48] M. Harter, J. Hildebrandt, A. Ziroff, and T. Zwick, “Self-calibration of a 3-d-digital beamforming radar system for automotive applications with installation behind automotive covers,” *IEEE Transactions on Microwave Theory and Techniques*, vol. 64, no. 9, pp. 2994–3000, 2016.
- [49] C. Pfeffer, R. Feger, C. Wagner, and A. Stelzer, “FMCW MIMO radar system for frequency-division multiple tx-beamforming,” *IEEE Transactions on Microwave Theory and Techniques*, vol. 61, no. 12, pp. 4262–4274, 2013.
- [50] —, “A multimode-beamforming 77-ghz fmcw radar system,” in *2013 IEEE MTT-S International Microwave Symposium Digest (MTT)*, 2013, pp. 1–4.
- [51] R. Feger, C. Pfeffer, and A. Stelzer, “A frequency-division MIMO fmcw radar system using delta-sigma-based transmitters,” in *2014 IEEE MTT-S International Microwave Symposium (IMS2014)*, 2014, pp. 1–4.
- [52] C. Pfeffer, R. Feger, and A. Stelzer, “A stepped-carrier 77-GHz OFDM MIMO radar system with 4 GHz bandwidth,” 09 2015, pp. 97–100.
- [53] A. Dürr, D. Schwarz, S. Häfner, M. Geiger, F. Roos, M. Hitzler, P. Hügler, R. Thomä, and C. Waldschmidt, “High-resolution 160-ghz imaging MIMO radar using MMICs with on-chip frequency synthesizers,” *IEEE Transactions on Microwave Theory and Techniques*, vol. 67, no. 9, pp. 3897–3907, 2019.
- [54] *TEF810X Fully-Integrated 77 GHz Radar Transceiver*, NXP, 2017. [Online]. Available: <https://www.nxp.com/docs/en/fact-sheet/TEF810XFS.pdf>
- [55] *AWR2243 Evaluation Module (AWR2243BOOST) mmWave Sensing Solution*, Texas Instruments, 2020. [Online]. Available: <https://www.ti.com/lit/pdf/spruit8>

- [56] *AWRx Cascaded Radar RF Evaluation Module (MMWCAS-RF-EVM)*, Texas Instruments, 2019. [Online]. Available: <https://www.ti.com/lit/pdf/swru553>
- [57] *SiRad MIMO - 24 GHz*, Silicon Radar, 2020. [Online]. Available: https://siliconradar.com/wiki/MIMO_Kit
- [58] T. Savelyev, X. Zhuge, B. Yang, P. Aubry, A. Yarovoy, L. Ligthart, and B. Levitas, "Comparison of 10–18 GHz SAR and MIMO-based short-range imaging radars," *International Journal of Microwave and Wireless Technologies*, vol. 2, no. 3-4, p. 369–377, 2010.
- [59] D. Bleh, M. Rösch, M. Kuri, A. Dyck, A. Tessmann, A. Leuther, S. Wagner, and O. Ambacher, "A 100 GHz FMCW MIMO radar system for 3d image reconstruction," in *2016 European Radar Conference (EuRAD)*, 2016, pp. 37–40.
- [60] D. Bleh, M. Rösch, M. Kuri, A. Dyck, A. Tessmann, A. Leuther, S. Wagner, B. Weismann-Thaden, H.-P. Stulz, M. Zink, M. Rießle, R. Sommer, J. Wilcke, M. Schlechtweg, B. Yang, and O. Ambacher, "W -band time-domain multiplexing FMCW MIMO radar for far-field 3-d imaging," *IEEE Transactions on Microwave Theory and Techniques*, vol. 65, no. 9, pp. 3474–3484, 2017.
- [61] *60GHz mmWave Sensor EVMs*, Texas Instruments, 2018. [Online]. Available: <https://www.ti.com/tool/IWR6843ISK#tech-docs>
- [62] *FMCW radar working in the 24GHz ISM-band*, InnoSent. [Online]. Available: <https://www.innosent.de/en/radarsysteme/isys-50er-serie/isys-5021-radarsystem-with-tracker-license/>
- [63] Vayyar walabot-60GHz. [Online]. Available: https://walabot.com/docs/Walabot60ghz_spec?type=pdf
- [64] *High-Resolution 4D Imaging*, Arbe Robotics. [Online]. Available: <https://arberobotics.com/product/>
- [65] *AUTOMOTIVE SENSOR UMRR-11 TYPE 132*, Smartmicro. [Online]. Available: https://www.smartmicro.com/fileadmin/media/Downloads/Automotive_Radar/Sensor_Data_Sheets_76-81GHz/UMRR-11_Type_132_Automotive_Data_Sheet.pdf
- [66] J. Li and P. Stoica, *MIMO Radar Signal Processing*, ser. Wiley - IEEE. Wiley, 2008.
- [67] E. Murphy and C. Slattery, "Ask the application engineer — 33 all about direct digital synthesis," *Analog Dialogue*, vol. 38, no. 3, 08 2004.

- [68] D. Dhar, P. T. M. van Zeijl, D. Milosevic, H. Gao, and A. H. M. van Roermund, "Modeling and analysis of the effects of pll phase noise on fmcw radar performance," in *2017 IEEE-ISCAS*, May 2017, pp. 1–4.
- [69] U. Johannsen, A. Smolders, R. Mahmoudi, and J. Akkermans, "Substrate loss reduction in antenna-on-chip design," in *2009 IEEE Antennas and Propagation Society International Symposium*, 2009, pp. 1–4.
- [70] *Radar Development Kit RIC60: Documentation*, Omniradar, 2014.
- [71] B. B. Adela, "Antennas for silicon-based mm-wave FMCW radars: antenna integration and MIMO system design," Ph.D. dissertation, Eindhoven NL, 2019.
- [72] P. van Zeijl, "Amplitude and phase accuracy of a sinusoidal-signal versus noise," Omniradar, 2016.
- [73] D. Dhar, P. T. M. van Zeijl, D. Milosevic, H. Gao, and P. G. M. Baltus, "Analysis of the effect of pfd sampling on charge-pump pll stability," in *2018 IEEE International Symposium on Circuits and Systems (ISCAS)*, 2018, pp. 1–5.
- [74] J. Ruze, "The effect of aperture errors on the antenna radiation pattern," *Il Nuovo Cimento*, vol. 9, pp. 364–380, Mar. 1952.
- [75] J. K. Hsiao and Naval Research Laboratory (U.S.), *Array sidelobes, error tolerance, gain, and beamwidth [microform] / James K. Hsiao*. Naval Research Laboratory Washington, D.C, 1984.
- [76] J. K. Hsiao, "Effects of errors on the side-lobe level of a low-side lobe array antenna," p. 24, 06 1981.
- [77] C. Bencivenni, M. Ivashina, R. Maaskant, and J. Wettergren, "Design of maximally sparse antenna arrays in the presence of mutual coupling," *IEEE Antennas and Wireless Propagation Letters*, vol. 14, pp. 159–162, 2015.
- [78] SKA Radio Telescope. [Online]. Available: <http://www.skatelescope.org>
- [79] W. A. van Cappellen, M. Santos, J. P. Macquart, F. Abdalla, E. Petroff, A. Siemion, R. Taylor, O. Smirnov, D. Davidson, and J. Broderick, "MANTIS: The Mid-Frequency Aperture Array Transient and Intensity-Mapping System," *arXiv e-prints*, p. arXiv:1612.07917, Dec 2016.
- [80] W. A. Van Cappellen, J. D. Bregman, and M. J. Arts, "Effective sensitivity of a non-uniform phased array of short dipoles," *Experimental Astronomy*, vol. 17, no. 1, pp. 101–109, Jun 2004. [Online]. Available: <https://doi.org/10.1007/s10686-005-0789-x>

- [81] J. bij de Vaate, D. Davidson, and N. Razavi-Ghods, "Sparse-regular aperture array SKA telescope concept," in *2017 Prog. Electromagn. Res. S*, 05 2017, pp. 1540–1543.
- [82] J. bij de Vaate, D. Davidson, and S. Wijnholds, "Regular sparse arrays: The impact of grating lobes on radio astronomical observations," in *2018 2nd URSI Atlantic Radio Science Meeting (AT-RASC)*, 05 2018, pp. 1–3.
- [83] R. J. Bolt, D. Cavallo, G. Gerini, D. Deurluo, R. Grooters, A. Neto, and G. Toso, "Characterization of a dual-polarized connected-dipole array for ku-band mobile terminals," *IEEE Trans. Antennas Propag.*, vol. 64, no. 2, pp. 591–598, Feb 2016.
- [84] J. Gilmore and D. B. Davidson, "Suppressing undesired common-mode resonances in connected antenna arrays," *IEEE Trans. Antennas Propag.*, vol. 63, no. 11, pp. 5245–5250, Nov 2015.
- [85] Y. Zhang and A. K. Brown, "Octagonal ring antenna for a compact dual-polarized aperture array," *IEEE Trans. Antennas Propag.*, vol. 59, no. 10, pp. 3927–3932, Oct 2011.
- [86] W. H. Syed, D. Cavallo, H. Thippur Shivamurthy, and A. Neto, "Wideband, wide-scan planar array of connected slots loaded with artificial dielectric superstrates," *IEEE Trans. Antennas Propag.*, vol. 64, no. 2, pp. 543–553, Feb 2016.
- [87] E. de Lera Acedo, E. Garcia, V. González-Posadas, J. L. Vazquez-Roy, R. Maaskant, and D. Segovia, "Study and design of a differentially-fed tapered slot antenna array," *IEEE Trans. Antennas Propag.*, vol. 58, no. 1, pp. 68–78, Jan 2010.
- [88] M. Ruiter, W. van Cappellen, E. van der Wal, M. Arts, R. van den Brink, and K. Visser, "Development of a vivaldi tile for the ska mid frequency aperture array," in *2016 10th Eur. Conf. Antennas and Propag.*, 04 2016, pp. 1–4.
- [89] R. Maaskant, "Analysis of large antenna systems," Ph.D. dissertation, Electrical Engineering, Eindhoven University of Technology, 2010.
- [90] R. Maaskant, E. E. M. Woestenburger, and M. J. Arts, "A generalized method of modeling the sensitivity of array antennas at system level," in *34th Eur. Microw. Conf., 2004.*, 10 2004, pp. 1541–1544.
- [91] M. Arts, M. Brethouwer, and M. Ruiter, "Noise modeling of a 4x4 prototype array for the mid frequency aperture array," in *Int. Conf. on Electromagn. Adv. Appl, ICEAA 2017*, 2017, pp. 1415–1417.

- [92] Agilent Advance Design System (ADS). [Online]. Available: <https://www.keysight.com/en/pc-1297113/advanced-design-system-ads>
- [93] J. Hasch, E. Topak, R. Schnabel, T. Zwick, R. Weigel, and C. Waldschmidt, "Millimeter-Wave Technology for Automotive Radar Sensors in the 77 GHz Frequency Band," *IEEE Transactions on Microwave Theory Techniques*, vol. 60, no. 3, pp. 845–860, Mar. 2012.
- [94] Electro Rent e-book, *Development and Test of New Automotive Radar Technologies*. Microwave Journal, Nov. 2019. [Online]. Available: <https://books.google.nl/books?id=HaK6QgAACAAJ>
- [95] R. Rotman, "Recent advances using microwaves for imaging, hyperthermia and interstitial ablation of breast cancer tumors," in *2011 IEEE International Conference on Microwaves, Communications, Antennas and Electronic Systems (COM-CAS 2011)*, 2011, pp. 1–4.
- [96] G. L. Charvat, L. C. Kempel, E. J. Rothwell, C. M. Coleman, and E. L. Mokole, "An ultrawideband (uwb) switched-antenna-array radar imaging system," in *2010 IEEE International Symposium on Phased Array Systems and Technology*, 2010, pp. 543–550.
- [97] J. L. Allen, "The theory of array antennas (with emphasis on radar applications)," in *Technical Report 323, MIT Lincoln Laboratory*, July 1963.
- [98] F. Robey, S. Coutts, D. Weikle, J. McHarg, and K. Cuomo, "MIMO radar theory and experimental results," in *Conference Record of the Thirty-Eighth Asilomar Conference on Signals, Systems and Computers, 2004.*, vol. 1, 2004, pp. 300–304 Vol.1.
- [99] J. Li and P. Stoica, "MIMO radar with colocated antennas," *IEEE Signal Processing Magazine*, vol. 24, no. 5, pp. 106–114, 2007.
- [100] *AWR1443 Single Chip 77 and 79 GHz FMCW Radar Sensor*, Texas Instruments, 2017. [Online]. Available: <https://www.ti.com/product/AWR1443>
- [101] M. E. Yanik, D. Wang, and M. Torlak, "3-D MIMO-SAR imaging using multi-chip cascaded millimeter-wave sensors," in *2019 IEEE Global Conference on Signal and Information Processing (GlobalSIP)*, 2019, pp. 1–5.
- [102] B. B. Adela, M. C. van Beurden, P. Van Zeijl, and A. B. Smolders, "High-isolation array antenna integration for single-chip millimeter-wave FMCW radar," *IEEE Transactions on Antennas and Propagation*, vol. 66, no. 10, pp. 5214–5223, 2018.

- [103] X. Zhuge and A. G. Yarovoy, "Study on two-dimensional sparse MIMO UWB arrays for high resolution near-field imaging," *IEEE Transactions on Antennas and Propagation*, vol. 60, no. 9, pp. 4173–4182, 2012.
- [104] R. Z. Syeda, B. B. Adela, M. C. van Beurden, P. T. M. van Zeijl, and A. B. Smolders, "Design of a mm-wave MIMO radar demonstrator with an array of FMCW radar chips with on-chip antennas," in *2019 16th European Radar Conference (EuRAD)*, 2019, pp. 33–36.
- [105] C. Vasanelli, R. Batra, and C. Waldschmidt, "Optimization of a MIMO radar antenna system for automotive applications," in *2017 11th European Conference on Antennas and Propagation (EUCAP)*, 2017, pp. 1113–1117.
- [106] A. Di Serio, P. Hügler, F. Roos, and C. Waldschmidt, "2-D MIMO Radar: A method for array performance assessment and design of a planar antenna array," *IEEE Transactions on Antennas and Propagation*, vol. 68, no. 6, pp. 4604–4616, 2020.
- [107] S. J. Miller, "Synthesis of uniform amplitude focused beam arrays," Mathematics Department Brown University Providence, RI 02912, 2006.
- [108] R. Z. Syeda, T. G. Savelyev, M. C. van Beurden, and A. B. Smolders, "Sparse MIMO array for improved 3D mm-wave imaging radar," in *2020 17th European Radar Conference (EuRAD), Utrecht, Netherlands, 2021*. IEEE, 2020, pp. 342–345.
- [109] M. Grant and S. Boyd, "CVX: Matlab software for disciplined convex programming, version 2.1," <http://cvxr.com/cvx>, Mar. 2014.
- [110] M. Grant and B. Stephen, *Graph implementations for nonsmooth convex programs, Recent Advances in Learning and Control*, ser. Lecture Notes in Control and Information Sciences. Springer-Verlag Limited, 2008. [Online]. Available: http://stanford.edu/~boyd/graph_dcp.html
- [111] D. Ruiz-Antolin and A. Townsend, "A nonuniform fast fourier transform based on low rank approximation," 2017.
- [112] J. Wang, H. Cetinkaya, and A. Yarovoy, "Nufft based frequency-wavenumber domain focusing under MIMO array configurations," in *2014 IEEE Radar Conference*, 2014, pp. 1–5.
- [113] *Radar Measurements*, Keysight Technologies, 2017. [Online]. Available: <https://www.keysight.com/nl/en/assets/7018-01694/application-notes/5989-7575.pdf>

- [114] C. Vasanelli, F. Roos, A. Durr, J. Schlichenmaier, P. Hugler, B. Meinecke, M. Steiner, and C. Waldschmidt, "Calibration and direction-of-arrival estimation of millimeter-wave radars: A practical introduction," *IEEE Antennas and Propagation Magazine*, vol. 62, no. 6, pp. 34–45, 2020.
- [115] A. Bhattacharya, R. Sarkis, G. Hislop, S. Lambot, and C. Craeye, "Modeling of an ultra-wideband antenna array devoted to near-field imaging," in *2010 Loughborough Antennas Propagation Conference*, 2010, pp. 545–548.
- [116] M. I. Grace, "Measurement of Radar Cross Section Using the "VNA Master" Handheld VNA."
- [117] A. van den Biggelaar, D. Daverveld, A. Reniers, U. Johannsen, and A. Smolders, "Assessment of a contactless characterization method for integrated antennas," in *2019 16th European Radar Conference (EuRAD)*, 2019, pp. 381–384.
- [118] A. J. Van Den Biggelaar, E. Galesloot, A. C. Franciscus, A. B. Smolders, and U. Johannsen, "Verification of a contactless characterization method for millimeter-wave integrated antennas," *IEEE Transactions on Antennas and Propagation*, vol. 68, no. 5, pp. 3358–3365, 2020.
- [119] J.-S. Hong and M. Lancaster, *Microstrip Filters for RF/Microwave Applications*, 1st ed. Wiley, 2001.
- [120] M. Sadiku and C. Akujuobi, "S-parameters for three and four cascaded two-ports," in *IEEE SoutheastCon, 2004. Proceedings.*, 2004, pp. 410–412.
- [121] U. Johannsen, M. Spiritoy, and A. Smolders, "Contactless measurement method for integrated mm-wave antennas," in *Proceedings of the 5th European Conference on Antennas and Propagation (EUCAP)*, 2011, pp. 797–801.
- [122] (2017) Texas Instruments. [Online]. Available: <https://www.ti.com/sensors/mmwave-radar/automotive/overview.html>
- [123] C. Waldschmidt, J. Hasch, and W. Menzel, "Automotive radar — from first efforts to future systems," *IEEE Journal of Microwaves*, vol. 1, no. 1, pp. 135–148, 2021.
- [124] F. E. Gardiol, "Open-ended waveguides: Principles and applications," ser. *Advances in Electronics and Electron Physics*, P. W. Hawkes, Ed. Academic Press, 1985, vol. 63, pp. 139–187. [Online]. Available: <https://www.sciencedirect.com/science/article/pii/S0065253908603522>
- [125] Quinstar (QWA MN:15R18X). [Online]. Available: <https://quinstar.com/shop/waveguides-related-products/transitions-adapters/waveguide-to-coax-adapters-qwa/>

-
- [126] GORE® PHASEFLEX® Microwave/RF Test Assemblies. [Online]. Available: <https://www.gore.com/products/gore-phaseflex-microwave-rf-test-assemblies>
 - [127] Maury Microwave. [Online]. Available: https://www.maurymw.com/Precision/1.85mm_Cal_Kits.php
 - [128] A. Al-Hourani, R. J. Evans, P. M. Farrell, B. Moran, M. Martorella, S. Kandeepan, S. Skafidas, and U. Parampalli, "Chapter 7 - millimeter-wave integrated radar systems and techniques," in *Academic Press Library in Signal Processing, Volume 7*, R. Chellappa and S. Theodoridis, Eds. Academic Press, 2018, pp. 317–363. [Online]. Available: <https://www.sciencedirect.com/science/article/pii/B9780128118870000079>
 - [129] A. Ganis, E. M. Navarro, B. Schoenlinner, U. Prechtel, A. Meusling, C. Heller, T. Spreng, J. Mietzner, C. Krimmer, B. Haeberle, S. Lutz, M. Loghi, A. Belenguer, H. Esteban, and V. Ziegler, "A portable 3-d imaging fmcw mimo radar demonstrator with a 24×24 antenna array for medium-range applications," *IEEE Transactions on Geoscience and Remote Sensing*, vol. 56, no. 1, pp. 298–312, 2018.

List of publications

Journal publications

- [J1] R. Z. Syeda, M. C. van Beurden and A. B. Smolders, "Sparse Virtual Array Synthesis for MIMO Radar Imaging Systems," *IET Microw. Antennas Propag.* 2021;1–15. <https://doi.org/10.1049/mia2.12129>.
- [J2] R. Z. Syeda, J. G. Bij de Vaate and D. Prinsloo, "Regular and Irregular-on-Grid Sparse Array Comparison of Connected Aperture Arrays," in *IEEE Antennas and Wireless Propagation Letters*, vol. 19, no. 4, pp. 586-590, April 2020, doi: 10.1109/LAWP.2020.2972700.
- [J3] R. Z. Syeda, M. C. van Beurden and A. B. Smolders, "Virtual Array Pattern Measurements using two-port VNA," (in preparation)

Conference publications

- [C1] R. Z. Syeda, T. G. Savelyev, M. C. van Beurden and A. B. Smolders, "Sparse MIMO Array for Improved 3D mm-Wave Imaging Radar," *2020 17th European Radar Conference (EuRAD)*, Utrecht, Netherlands, 2021, pp. 342-345, doi: 10.1109/EuRAD48048.2021.00094.
- [C2] R. Z. Syeda, B. B. Adela, M. C. van Beurden, P. T. M. van Zeijl and A. B. Smolders, "Design of a mm-wave MIMO radar demonstrator with an array of FMCW radar chips with on-chip antennas," *2019 16th European Radar Conference (EuRAD)*, Paris, France, 2019, pp. 33-36.
- [C3] R. Z. Syeda, M. C. van Beurden and A. B. Smolders, "On the Phase-Error Tolerance of Virtual Antenna Arrays in MIMO Radars," *2019 IEEE International Symposium on Antennas and Propagation and USNC-URSI Radio Science Meeting*, Atlanta, GA, USA, 2019, pp. 1573-1574, doi: 10.1109/APUSNCURSINRSM.2019.8888580.
- [C4] R. Z. Syeda, B. B. Adela, M. C. van Beurden, P. T. M. van Zeijl and A. B. Smolders, "Beamwidth enhancement of on-chip antenna integrated in single-chip FMCW radar using periodic dielectric lenses," *2017 11th European Conference on Antennas and Propagation (EuCAP)*, Paris, France, 2017, pp. 1170-1173, doi: 10.23919/EuCAP.2017.7928108.

Acknowledgements

Finally, a long journey has come to an end and a few people have supported me in so many different ways during this time. Gratitude is in order and so I would take this opportunity to pay my regards.

First, and foremost, I would like to thank my first promoter, prof.dr.ir. Bart Smolders. It is said that sometimes all you need is someone who is willing to give you a chance and for me that someone has been Bart Smolders. I am really grateful to Bart for giving me an opportunity to work on the MUSIC project, almost six years ago as PDEng candidate. By the end of my two-year program, I was very much invested into the project, which Bart saw and then offered me this PhD position. Thank you, Bart, it has been an enriching experience for me and has set up my future career path in EM and antenna engineering. I would also like to thank you for all of your guidance through the years, it has been really helpful in the times I got stuck in my PhD. Next, I want to thank my second promoter, prof.dr.ir. Martijn van Beurden who has also been my daily supervisor. Martijn, you have been a constant source of support throughout the years. I highly appreciated our lengthy technical discussions while trying to steer the path of my PhD in the right direction. You always encouraged me and motivated me to push myself to go in detail and better understand my research topic. Your critical review of my work has always allowed me to bring my work to a higher level. Thank you for being a great mentor.

I would like to thank my MUSIC-project team, in particular, Bedilu Adela, Debashis Dhar, and Dusan Milosevic for their advice and guidance during our bi-monthly meetings. My PhD project was in collaboration with Omniradar and my heartfelt gratitude goes to Paul van Zeijl and the former employees of Omniradar for their support during the design of the MIMO radar demonstrator presented in this thesis. I am highly grateful to Paul for his extensive supervision during the realization phase of the demonstrator, without which I would not have been able to take up such a challenging task. I would like to mention some names, Jacques Rompen, Marilyn Arts, Jan Willem Wakker, and Thom van Zeijl, who helped me in debugging the hardware and software over and over again before it was fully functional.

During my PhD journey, I spent four months as a guest researcher at ASTRON. I am indebted to Mark Bantum for arranging the position and warmly welcoming me to ASTRON. I would like to thank Jan Geralt bij de Vaate and David Prinsloo for their supervision during my stay. I thoroughly enjoyed our discussions and it made me realize how many interesting/intriguing similarities and differences there are between the fields of astronomy and radar. I would extend my gratitude towards Heleen and Piet for allowing me to live in their beautiful farmhouse and being gracious hosts. In the last stage of my PhD, I also collaborated with Radar Xense and I would like to thank Timofey Savelyev and Olaf Biezevan for lending us the Vayyar platform and collaborating on the sparse array analysis for the platform.

I would like to thank the EM group members (current and former) for making a great environment to work at TU/e and for always being supportive and eager to help. Certainly, I wish to mention some names who directly influenced my work during my PhD journey. Sander Bronckers, thank you for being an amazing office mate and colleague, you had been my go-to guy for any type of advice, technical or non-technical. I absolutely enjoyed our discussions during our coffee breaks and I somehow always found motivation to complete my PhD after our casual chats. Rocío Molina, thank you for all your support, we had collaborated only in the last year of my PhD, but certainly you greatly contributed towards the end phase. Thanks to Ronis Maximidis, Fahimeh Sepehripour and Ellen van Wesel for being great office mates. A great deal of gratitude is owed to Ad Reniers for being the primary source of support whenever I needed help with measurements. Thank you, Ad, for always being willing to discuss and provide insight into the measurement results. Special thanks to Suzanne Kuijlaars for being the backbone of the group and for always being there to solve my administrative problems, an uncountable number of times. I would also like to thank Rian van Gaalen for always being so helpful during my PDEng time and even during my PhD, and for introducing me to Monique Hunck, who graciously took care of my cat during my stay at ASTRON, which allowed me to fully focus on my research. Thank you, Monique also for supporting me during the corona times and keeping a check on me. I highly appreciate that!

I wish to pay my regards to my committee members, dr.ir. Christophe Craeye, prof.dr.ir. Peter Baltus and prof.dr.ir. Massimo Mischi for their valuable feedback on this thesis, which allowed me to further improve my thesis.

The completion of my PhD thesis would not have been possible without the support of my friends and family. A special thanks to Aymen Ayaz for hosting lovely dinners at her place, which compensated for all the Pakistani food I missed, for nice discussions and great company. A heartfelt gratitude is owed to Kousar Aslam, whom I got to know in the last year of my PhD. Kousar, thank you for immense emotional support you provided during the corona times. I am amazed with the connection we developed in such a short time and I would say that my PhD thesis writing would not have seen the finish line if it wasn't for so many pep talks from you!

Even though being thousands of miles away, my family has always been a great source of inspiration for me. I would like to thank my siblings, Mahrukh, Rubab, Anum and Ali Akbar for always being there for me, special thanks to my nephew Ali Abbas and my niece Aroush, who have grown up so much in the past few years that they have amazingly provided some valuable advice in certain aspect of this thesis.

Last, but not least, my deepest gratitude goes to the two most important people in my life; my mother, Anila Zainab and my sister, Affifa Zainab. First to my mother, Mama, whoever I am and wherever I am today it's because of you. Thank you for all your prayers, and love.

To my sweet, caring, and supportive sister, Affifa Zainab; I don't have words to express my gratitude for you always being there for me, through thick and thin. Your encouragement and your assistance have always allowed me to pass through the challenging times during this PhD period. Thank you for being so patient during all the times when I talked about my technical stuff, and you always managed to give me useful advice. You are my person, thank you for everything!

Curriculum Vitae

Rabia Zainab Syeda was born on the 19th November 1988, in Rawalpindi, Pakistan. Rabia received her bachelor's degree in telecommunications engineering from the University of Engineering and Technology (UET) Taxila, Pakistan, in 2011. In 2012, she was awarded an Erasmus Mundus scholarship for a European master's and completed her dual MSc degree in Electrical Engineering from Karlsruhe Institute of Technology (KIT), Germany, and Polytechnic University of Catalonia (UPC), Barcelona, Spain, in 2014. She received her PDEng. (Post-Master Design Engineer) degree on mm-Wave MIMO Integrated radars in 2017 from Eindhoven University of Technology (TU/e), The Netherlands, within the Electromagnetics group. From 2017, she started her PhD degree in the same group, of which the main results are presented in this thesis.



In 2018, she received the TU/e Academic award for the Best PDEng thesis for the year 2017. During her PhD, she co-supervised many BSc, MSc, and PDEng students, taught main lectures and guest lectures for various courses. She was a guest researcher at the Netherlands Institute for Radio Astronomy (ASTRON) for four months in 2019. She is currently employed as Electromagnetic Design Engineer (Automotive Radar, mmWave) at NXP Semiconductors, Eindhoven. Her research interests include mm-Wave antennas, sparse antenna array synthesis for radar systems and MIMO radar system architectures.